10-30-2020

Numerical Prediction of Automotive Underhood Airflows using an Uncalibrated Fan Body Force Model

Palak Saini
University of Windsor

Numerical Prediction of Automotive Underhood Airflows using an Uncalibrated Fan Body Force Model

by

Palak Saini

A Thesis
Submitted to the Faculty of Graduate Studies
through the Department of Mechanical, Automotive & Materials Engineering
in Partial Fulfillment of the Requirements for
the Degree of Master of Applied Science at the
University of Windsor

Windsor, Ontario, Canada
2020

Numerical Prediction of Automotive Underhood Airflows using an Uncalibrated Fan Body Force Model

by

Palak Saini

APPROVED BY:

_____

P. Henshaw

Department of Civil & Environmental Engineering

_____

E. Farbar

Department of Mechanical, Automotive & Materials Engineering

_____

J. Defoe, Advisor

Department of Mechanical, Automotive & Materials Engineering

September 14, 2020

Declaration of Co-Authorship/Previous Publication

I hereby declare that this thesis incorporates material that is the result of joint research, as follows: The thesis was authored by Palak Saini under the supervision of professor Dr. J. Defoe and adjunct professor, Dr. E. Farbar. In all cases, the key ideas, primary contributions, experimental designs, data analysis, interpretation, and writing were performed by the author; Dr. J. Defoe and Dr. E. Farbar provided feedback on refinement of ideas and editing of the manuscript. I am aware of the University of Windsor Senate Policy on Authorship and I certify that I have properly acknowledged the contribution of other researchers to my thesis, and have obtained written permission from each of the co-author(s) to include the above material(s) in my thesis. I certify that, with the above qualification, this thesis, and the research to which it refers, is the product of my own work. This thesis includes 3 original papers that have been or will be submitted for publication in peer reviewed conferences and/or journals, as follows:

Thesis Chapter	Publication title/Full Citation	Publication Status
Chapter 2	Palak Saini, Jeff Defoe and Erin Farbar. A framework for implementing volumetric source term models in OpenFOAM and Star-CCM+.	Intended for CFD Society of Canada Conference 2021
Chapter 3	Palak Saini and Jeff Defoe. GT2020-16176: The effect of blade count on body force model performance for axial fans. In Turbo Expo: Power for Land, Sea, and Air, 2020.	Accepted for Turbo Expo 2020 Conference and recommended for publication in the Journal of Turbomachinery
Chapter 4	Palak Saini, Erin Farbar and Jeff Defoe. Suitability Assessment of an Uncalibrated Body Force Based Fan Modeling Approach to Predict Automotive Under-hood Airflows. SAE Technical Paper, 2020.	To be submitted pending review by industrial partners (WCX SAE World Congress 2021)

I certify that I am in the process of obtaining written permission from the copyright owner to include the above published material (Chapter 3) in my thesis. I certify that the above material describes work completed during my registration as a graduate student at the University of Windsor. I declare that, to the best of my knowledge, my thesis does not infringe upon anyone's copyright nor violate any proprietary rights and that any ideas, techniques, quotations, or any other material from the work of other people included in my thesis, published or otherwise, are fully acknowledged in accordance with the standard referencing practices. Furthermore, to the extent that I have included copyrighted material that surpasses the bounds of fair dealing within the meaning of the Canada Copyright Act, I certify that I have sought, and expect to obtain, written permission from the copyright owner to include such material(s) in my thesis. I declare that this is a true copy of my thesis, including any final revisions, as approved by my thesis committee and the Graduate Studies office, and that this thesis has not been submitted for a higher degree to any other University or Institution.

Abstract

Underhood vehicle airflow simulations are an important part of the overall vehicle thermal management process, especially in the preliminary stages of the vehicle development program when performing experimental work on cooling system prototypes can prove to be expensive, time-consuming, or simply impossible due to the absence of any physical vehicle prototypes. Accurate prediction of the automotive fan performance, which forms a critical component of the cooling module, is a prerequisite for the optimum sizing and design of heat exchangers, and the rest of the under-hood installations. The coupled and complex nature of the under-hood flow environment necessitates consideration of the entire front-end cooling module, and preferably the entire vehicle, in a single simulation to judge the fan performance. Direct modelling of the rotating fan blades in a full vehicle simulation can yield unacceptably long run times, hence the norm is to use simplified numerical models which can capture the general fan behaviour at a reduced cost. Industrial practice is to calibrate these fan models with experimental or high-fidelity simulated fan performance data, which slows down the design process and is expensive. This work solves this problem by using an uncalibrated body force fan modelling approach, which only requires fan geometry information and no a-priori fan performance data. The approach has previously shown promising results for aircraft engine fan applications, however it's suitability for automotive fan applications is tested for the first time. The model performs with a comparable accuracy as the current state-of-the-art calibrated fan modelling techniques. It predicts the radiator airflow rate to within 8% of the experimentally-measured value at idle. At high vehicle speed, the accuracy improves to 1%. Success in this project facilitates a low-cost, reliable and rapid aerothermal analysis tool for designing vehicle cooling systems.

To my parents Anita and Raj,

my two pillars of strength and righteousness.

This work is a culmination of all the sacrifices you made

to get me the best education that you could.

Thank you for your constant love and encouragement,

even from oceans away.

Acknowledgements

I am blessed to have worked with two incredibly supportive and patient advisors through the two years of my graduate degree. Foremost, I would like to express my sincere gratitude to Dr. Jeffrey Defoe, who has the substance of a genius: his terrific mentorship, expertise in the field of turbomachinery and extended discussions have left me enriched, both academically and professionally. Dr. Defoe, your generous time and numerous weekends spent on reviewing my thesis, papers and presentations are gratefully acknowledged. I am profoundly indebted to my industrial advisor, Dr. Erin Farbar whose dedicated involvement and genuine enthusiasm for the project has been instrumental in getting this project done on time and improving the quality of this research. Moreover, her guidance has refined my personal and professional perspective towards my work.

This thesis has also benefited from comments and suggestions made by Dr. Paul Henshaw, whose time spent on reviewing the thesis is duly recognized. Also, this research would not have been possible without the generous resources and funding provided by Fiat Chrysler Automobiles (FCA) Canada and MITACS.

I would also like to recognize the invaluable technical assistance and unwavering personal encouragement offered by past and current members of the Turbomachinery and Unsteady Flows Research Group: Majed Etemadi, David Jarrod Hill, Hani Khalili Param, Syamak Pazireh, Mehran Eshaghi, and Gurpinder Singh Basra.

None of this would have been possible without countless friends and family members who've kept me in their prayers. To Nupur - thank you for being my solid support system, you've helped me through difficult times this year. Last but not the least, thank you Nico, Youstina, Luigi and Madi for keeping me level-headed through the tough months of lockdown with your humorous company and all-you-can-eat food symposiums in my kitchen. If it weren't for you, this thesis would have been completed weeks, if not months, earlier.

Table of Contents

List of Tables

List of Figures

xviii

xix

Nomenclature

Symbols

AF	amplification factor
AR	aspect ratio of blade
B	number of blades
c	chord [m]
C_f	local skin friction coefficient
d	height of distorted region with total pressure deficit [m]
f	body force [m s^{-2}]
h	enthalpy [m^{2}s^{-2}]
n	blade surface camber normal
N	design rotational speed [rpm]
p	pressure [Pa]
r	radial coordinate [m]
R	duct radius [m]
u	absolute velocity [m s^{-1}]
U_{M}	mid span blade speed [m s^{-1}]
W	relative velocity [m s^{-1}]
x, y, z	Cartesian coordinates [m]
y^+	dimensionless wall distance
α	absolute swirl angle [degrees]
β	relative flow angle (in the blade frame of reference) [degrees]
γ	radial flow angle [degrees]
δ	flow deviation from blade camber surface [radians]

η polytropic efficiency

μ dynamic viscosity

ρ density [kg m^{-3}]

σ solidity (ratio of chord length to blade pitch)

ϕ flow coefficient

ψ fan work coefficient

ω angular velocity of the fan rotor [rad s^{-1}]

Subscripts

ax   axial

in   inlet

max   maximum

mid   midspan

n   normal component

o   outer

p   parallel component

t   total

r   radial component

x   x component

θ circumferential component

1   measurement at plane 1

2   measurement at plane 2

Superscripts

M   mass-averaged quantity

Abbreviations

BFM   Body Force Model

CFD   Computational Fluid Dynamics

MRF   Multiple-reference Frame

RANS   Reynolds-Averaged Navier–Stokes

URANS   Unsteady Reynolds-Averaged Navier–Stokes

Chapter 1

Introduction

The automotive radiator fan is a critical component of the vehicle cooling module as it is responsible for ensuring adequate cooling airflow throughout the front-end region of the vehicle. It is imperative to accurately predict the performance of the fan as it directly affects the size, design, and optimization of heat exchangers as well as the rest of the underhood installations. The large number of components which intervene in the complex and coupled aerothermal phenomena in the underhood compartment make it necessary for the entire vehicle front-end region, at minimum, to be considered for the accurate prediction of fan performance [1]. While experiments measuring performance of cooling fan prototypes in a full-scale vehicle are an essential step in the vehicle thermal management process, the cost considerations and complications associated with using experimental equipment in an already congested underhood region have lead to an increased focus on using numerical simulation as a tool to tackle the aerothermal management challenges in the vehicle underhood [1]. Moreover, the correct fan design has to be chosen in the early stages of the vehicle development program, well before actual vehicle prototypes are available for physical testing. In such a scenario, numerical simulation is the only available tool for assessing the aerothermal design of the vehicle.

Nevertheless, the inherent unsteadiness associated with turbomachinery flows demands enormous amounts of computational resources and long simulation times to directly resolve the flow around the fan blades; this makes it impractical to run full 3D unsteady Reynolds-averaged Navier-Stokes (RANS) simulations for a full vehicle.

This has fueled the development of simplified fan models which can respond realistically when placed in an underhood setting and predict the overall steady state influence of the fan on the cooling airflow. Existing practice in the industry is to calibrate such fan models based on experiments or higher-fidelity simulations. However, this slows down the design process and is expensive. This thesis serves to resolve this problem using a "body-force" type simplified fan modeling approach which does not require a-priori knowledge of the fan performance.

A body force model (BFM) replaces the physical blade row with volumetric momentum and energy source terms which are responsible for generating the flow turning, as well as the pressure and temperature changes that occur through the blade passage. Owing to the considerable reduction in mesh refinement enabled by the absence of actual blades, the body force model facilitates inexpensive numerical simulations. The model of interest in this work is the inviscid, incompressible BFM developed by Hall, Greitzer and Tan [2] which only requires knowledge of the blade geometry and local flow conditions to simulate the fan response. Hence, it does not require a-priori fan performance information for calibration. Numerous studies have successfully implemented this model in commercial computational fluid dynamics (CFD) solvers to accurately represent a fan, but all of these studies have been limited to aerospace applications only [2–4]. Automotive fans are built to have less than 10 blades, which is fewer than half the number of blades present in typical aerospace fans. Since Hall's model approximates a circumferentially "smeared-out" version of the blades effect on the flow, the accuracy of the model's predictions is expected to vary with the fan blade count or equivalently, for a given chord, the solidity of the fan.

To the author's knowledge, the model's applicability as an uncalibrated automotive fan modeling approach has never been tested before and there have been no

comprehensive studies regarding the effect of blade count on body force model accuracy in general. Moreover, the implementation details for incorporating the model into the open-source software package OpenFOAM, which offers a low-cost alternative to commercial CFD packages, have not previously been published. The objective of this thesis is to implement Hall's BFM in OpenFOAM to study the effect of blade count on body force model predictions, and to subsequently extend its use to full vehicle cooling airflow simulations in the commercial CFD code STAR-CCM+ [5] to study the effect of coupling between the fan and the surrounding non-uniform flow on cooling system performance in an actual vehicle setting.

1.1 Objective and High-Level Approach

The objective of this thesis is to apply an analytical body force fan modeling approach to automotive underhood cooling fans, so that the use of *calibrated* numerical fan models in this application can be eliminated. This will speed up the design process by enabling accurate analysis of cooling fans earlier in the design cycle, and will reduce overall effort and costly experimental measurements. The overall objectives of this work can be broken down into three parts:

- develop a framework to implement Hall's BFM in the OpenFOAM CFD package;

- investigate the impact of low blade count on the body force model predictions, and assess the results against high-fidelity simulations and experimental data; and

- implement the modeling approach for an automotive fan in full vehicle simulations during drive test cycles, and study the effect of coupling between the fan and the surrounding flow on the performance of the cooling system.

1.2 Thesis Outline and Overview of Contributions

This thesis is divided into three major chapters:

- **Chapter 2: A framework for implementing volumetric source term models in OpenFOAM and Star-CCM+**

  This chapter describes the body force formulation in detail along with the implementation of the model into an open-source as well as a commercial CFD framework. Two example applications of the model are presented and validated. The results demonstrate OpenFOAM's capabilities to support the addition of body forces and its comparable robustness to widely-used commercial CFD codes.

- **Chapter 3: The Effect of Blade Count on Body Force Model Performance for Axial Fans**

  This chapter investigates and quantifies the effect of low blade count on the accuracy of the body force model predictions for both uniform and non-uniform inflow. The key findings indicate that (i) for uniform flow, the accuracy of the model improves in the limit of low blade count due to the reduction of the blade metal blockage effects combined with spanwise flow redistribution mechanisms, and (ii) reducing the number of blades is found to have negligible impacts on upstream influence and distortion transfer in non-uniform inflow until extremely low blade counts (such as 2) are applied.

- **Chapter 4: Suitability Assessment of an Uncalibrated Body Force Based Fan Modeling Approach to Predict Automotive Under-hood Airflows**

  In this chapter, the uncalibrated BFM model is applied to simulations of airflow around and through an entire vehicle at a variety of speeds. The model

predicts the flow rate through the radiator to within 8% of the experimentally-measured value at idle. At high vehicle speed, the accuracy improves to 1%. The uncalibrated model has equal or better accuracy in predicting the flow rate compared to the current best-practice calibrated fan modellng techniques used in industry. The impact of the findings is a significant reduction in the overall effort, time, and cost involved in simulating under-hood and underbody flows.

Finally, Chapter 5 presents the conclusions drawn from the work, proposes recommendations for improving the technical implementation of the model and suggests a number of ideas for future research.

References

[1] Mahmoud Khaled, Mohamad Ramadan, Hicham El-Hage, Ahmed Elmarakbi, Fabien Harambat, and Hassan Peerhossaini. Review of underhood aerothermal management: Towards vehicle simplified models. *Applied Thermal Engineering*, 73(1):842–858, 2014.

[2] DK Hall, EM Greitzer, and CS Tan. Analysis of fan stage conceptual design attributes for boundary layer ingestion. *J. Turbomach.*, 139(7):071012, 2017.

[3] JJ Defoe, M Etemadi, and DK Hall. Fan performance scaling with inlet distortions. *J. Turbomach.*, 140(7):071009, 2018.

[4] David J Hill and Jeffrey J Defoe. Innovations in body force modeling of transonic compressor blade rows. *International Journal of Rotating Machinery*, 2018, 2018.

[5] Simcenter STAR-CCM+ user guide v13. 04. *Siemens PLM*, 2018.

Chapter 2

A Framework for Implementing Volumetric Source Term Models in OpenFOAM and Star-CCM+

The evolution of computational sciences in general, and computational fluid dynamics (CFD) in particular, is one of the major developments which have revolutionized the design process of turbomachinery at a fundamental level. With the advent of high-performance computing and ever shrinking design cycles, experiments are increasingly being supplanted by higher-fidelity CFD simulations, such as Large-Eddy simulations (LES) and unsteady Reynolds-averaged Navier-Stokes (URANS) simulations, to inform design tools and even improve lower order modeling approaches for turbomachinery [1]. However, despite the tremendous improvements in parallel computing and numerical algorithms, the enormous amounts of computational resources needed for higher fidelity simulations remains a major concern. In light of this, developing simpler models for estimating turbomachinery performance has emerged as a critical area of interest. The fact that these models can be straightforwardly implemented in low-cost general-purpose open source CFD solvers and unsophisticated in-house codes (which do not have advanced turbomachinery-specific functionality) presents another motivation for the development of these models.

In practical problems of interest, there are frequent instances when the interest is only capturing the general response of a turbomachinery component as part of a larger fluid flow or mechanical system. In such a case, the time-resolved flow details are not of significant interest. This has led to the development of multiple reduced order modeling approaches which can predict the steady-state response of a turbomachinery

component at a reduced cost. These steady-state lower order modeling approaches can be broadly divided into three categories and are listed below in order of decreasing complexity:

- the multiple-reference frame approach, which requires the user to define a volume containing the rotor blades within which the governing equations are solved in the rotating frame of reference of the rotating component;

- body force models, which introduce momentum and energy source terms inside a blade-free volume to mimic the work input and/or losses which occur in a blade passage; and

- actuator disks, which make use of experimental fan curves or simple models to impose discontinuous pressure changes across a thin fan-representing interface.

The first of these approaches, the multiple-reference frame (MRF) approach, uses a "frozen-rotor" technique to solve the equations of motion in a steady sense. The rotation is accounted for by the addition of centrifugal and Coriolis force source terms in the momentum equation in the region of interest. It is sufficient to couple the rotating and stationary regions at an interface to pass information through the domain [2]. Alternatively, a "mixing-plane" can be used to perform circumferential averaging of the solution at the interface. Most turbomachinery-capable commercial CFD codes, such as ANSYS CFX and STAR-CCM+, have inherent capabilities to define MRF regions and mixing planes [3, 4]. Such codes do not require modification of the background numerics of the CFD solver for setting up MRF models.

The MRF approach, though inexpensive, is inaccurate because its predictions have been found to be dependent on user-specific methodology such as the size and extent of the MRF domain [5, 6]. Therefore, it is typically used as an initial flow field approximation for higher-order turbomachinery simulations. Additionally, the MRF

approach still requires the construction of detailed blade geometry which can increase the grid count and the technique is suitable for steady flows only [7] (hence it cannot be applied to transient problems of interest). There are other techniques such as body force modeling and the actuator disk approach which can predict turbomachinery performance without requiring the construction of a detailed blade geometry, thus offering savings in simulation time and computational costs. These models are capable of working in a steady as well as an unsteady setting. The pressure rise obtained using these models is usually a physics-based approximation or an experimentally-calibrated value.

Simulating vehicle under-hood airflows is one example problem where the non-uniform nature of the surrounding airflow necessitates the construction and meshing of the complex geometry of the fan for full-wheel 3D unsteady RANS computations; this renders the calculation very intensive. Hence, the pressure rise through the radiator fan section is usually realized by adding a local forcing term to the momentum equations in a blade-free volume which represents the fan section [8, 9]. This approach, called the body force model (BFM), replaces the physical blades by virtual body forces in the form of momentum and energy source terms (for compressible flow) distributed across a blade-free volume as shown in Figure 2.1. The absence of physical blades allows for the creation of a much simpler grid, thereby reducing the mesh size and the computational costs. Additionally, this approach allows the use of steady CFD calculations to capture turbomachinery flows. Another example where body force models have been frequently used is the design and development of boundary-layer ingesting (BLI) propulsion systems [1] [11–16].

---

[1]Boundary layer ingesting (BLI) propulsion is a concept that has the potential to reduce the aircraft fuel burn by upto 8.5% compared to current aircraft [10]. The "double bubble" D8 series is one example of a BLI aircraft configuration with fuselage-embedded engines, as opposed to podded engines, which ingest the airframe boundary layers and use it to generate propulsive power. This reduces the aircraft drag as well as the required propulsive power. Due to the ingestion of boundary layers, these engines are subject to increased non-axisymmetric flow distortions at the inlet.
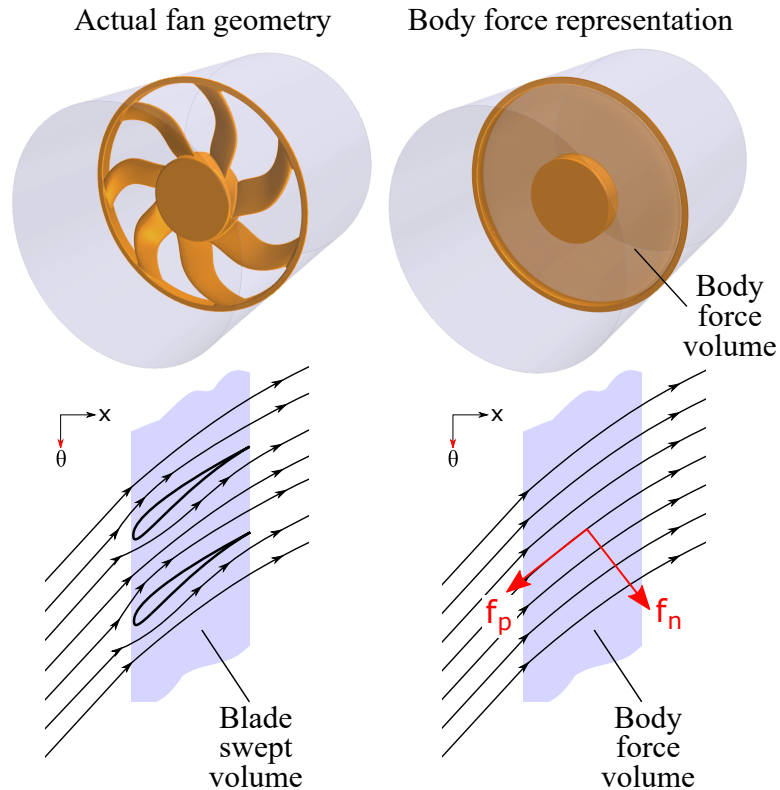
Figure 2.1: Flow through a real blade passage (left) and through a body force region (right). Source terms are distributed across the "body-force region" defined by the swept area of the blades. The force can be split into two components, i) the normal force f_n, responsible for pressure rise and flow turning, and ii) the parallel force f_p, responsible for generating blade profiles losses. The flow exits the "body-force" region without any circumferential variations in velocity due to absence of real blades.

Multiple variations of body force models are currently employed by the automotive and aerospace communities, and the majority of these models extract source term distribution information either from single passage, bladed calculations of the flow field or else require a-priori experimental fan performance data for calibration. Elimination of this calibration step can significantly reduce the overall associated costs and facilitate an accelerated design process for applications such as vehicle cooling systems and BLI aircraft configurations. A recent body force model developed by Hall et al. [12] is capable of predicting the fan performance without requiring a-priori knowledge of fan performance and hence, is the model of interest in this work.

Most widely-used CFD solvers provide varied forms of in-built body force models or actuator disk models which only require the user to provide certain basic input parameters which are used in the calculation of the source terms. For example, Simcenter STAR-CCM+ provides an actuator disk approach as well as a body force based approach to model axial fans under the names "the fan interface" and "the fan momentum source" respectively [4]. It also has several inbuilt physics-based body force models categorized under "Virtual Disk Models". The virtual disk model has three options which provide the capability to model the effects of turbomachines - the Body Force Propeller Method, The Blade Element Method and the 1D Momentum Method. Additionally, STAR-CCM+ has tools and utilities to simply define any variation of user-defined sources in an easy manner. This will be discussed in greater detail in the later sections.

Some other examples of CFD solvers which have been previously used with body force models are ANSYS CFX [14], Numeca FINE/Turbo [17], elsA [16] and SU2 [18]. In most commercial CFD codes, it is fairly simple to create user-defined code to implement any kind of body force model even without requiring a pre-existing template. On the other hand, for open-source software packages, the user might have to explore avenues to entirely modify the existing solvers to go beyond the basic capabilities of the code. This process can prove to be very time-consuming. Out of the four software packages listed above, Latour's BFM implementation in SU2 is the only published open-source code version of Hall's model [18], and hence a cheaper option for simulating simplified turbomachines. However, the code is limited to 2D applications only and has not been generalized for different turbomachinery configurations. This limits its usefulness to a certain degree.

Further development and understanding of the body force model requires an open-source solver with code that is modular, easily adaptable, and practical for running large simulations. The open-source CFD software package OPENFOAM v6 is an

interesting candidate for implementing a body force model because of its high adaptability to user-modified solvers and excellent parallel scaling capabilities for running large simulation cases [19, 20]. Hence, the objective of the present work is to detail a general systemic approach to implement body force (or source term) models in OPENFOAM V6, testing it for real fan geometries, and assessing the implementation of Hall's BFM in OPENFOAM V6 against commercial CFD solvers. Additionally, a general framework is also presented to implement the same model in the commercial general-purpose CFD code STAR-CCM+ [4]. To the best of the authors' knowledge, this is the first published account of the implementation of Hall's model in both codes.

The rest of the chapter is structured as follows. The work begins with a general overview of the "turbo tools" present in OPENFOAM V6. This is followed by an overview of Hall's body force model. Then, the detailed processes of model implementation in OPENFOAM V6 [19] and STAR-CCM+ [4] are discussed. Lastly, two test cases are presented and the OPENFOAM V6 results obtained are compared against those obtained from commercial CFD codes.

2.1 Overview of Source Term Modeling Capabilities in OpenFOAM

The open-source CFD solver OPENFOAM V6 [19] has some basic turbomachinery-specific functionality which can handle dynamic meshes, multiple-reference frame models as well as certain momentum source term models. Also, it offers a general capability for the addition of source terms to the governing equations via run-time selectable finite volume options, referred by the short form `fvOptions`. OPENFOAM V6 does not have a generic CFD solver, instead it makes the user choose from a range of standard solvers, each of which are designed for a specific class of problems and are able to handle any applicable sources through `fvOptions`. This work made use of a modified version of the solver `simpleFoam` which uses the SIMPLE algorithm and is meant for incompressible and steady turbulent flow problems.

The counterpart to the STAR-CCM+ [4] fan interface model in OPENFOAM v6 is the `fanPressure` boundary condition which is equivalent to an actuator disk [19]. It employs user-specified fan pressure curves to set the pressure rise/drop across an interface as a function of the volumetric flow rate. Under the `fvOptions` framework, the user can add "general" scalar or vector type volumetric source terms to governing equations without rewriting the original code, using the options `scalarCodedSource` and `vectorCodedSource` respectively. Under the same `fvOptions` framework, the user can also choose from a list of "derived" sources which are essentially pre-existing templates for commonly used momentum/energy sources such as porosity models, acoustic damping models, etc.

The "derived" sources also include three pre-defined models for turbomachinery under the class names `actuationDiskSource`, `radialActuationDiskSource` and `rotorDiskSource` [19]. The first of these models, `actuationDiskSource`, is based on Froude's 1D momentum theory to mimic axial loading of rotary disks such as propellors, helicopter rotors and horizontal-axis wind turbines [19, 21]. It is a kind of volumetric source term model which only requires the user to specify the area and location of the disk, and the power and thrust coefficients of the propellor to impart a uniform axial thrust to the flow. This class provides two options for force computations: the basic `Froude` implementation and an improved `variableScaling` option, which calculates a calibrated thrust coefficient based on single wind turbine blade wake simulations [22]. The `radialActuationDiskSource` is a variant of the actuator disk source which produces the thrust as a function of the radius of the actuator disk [19]. Although the two above-mentioned classes use the term "actuation", the source models are applied to cell volumes and therefore should not be confused with traditional "actuator disks" which possess zero-thickness. Lastly, the `rotorDiskSource` calculates momentum sources using a purely analytical approach based on the blade

element theory to simulate propellors. This class was originally developed by Wahono [23] and was further improved by Patrao [24]. It requires numerous details of the blade geometry and propeller performance to calculate the sources, the discussion of which is outside the scope of this chapter and can be found in Patrao's work [24]. More detailed information about these classes can be found in the OpenFOAM v6 documentation [19].

Owing to the fact that the physics underlying Hall's model is based on thin airfoil theory, which is entirely different from Froude's 1D momentum theory or the blade element method, none of these pre-defined source models or even their templates can be used as a basis for implementing Hall's model.

2.2   Description of Hall's Body Force Model

This section presents a general overview of Hall's model. For detailed information about the governing equations, the reader is advised to refer to works which have previously employed the model [12, 15]. Hall's approach is a purely analytical body force based approach to predict fan performance without requiring calibration with experimental data or high-fidelity simulations, a process which can prove to be expensive and time-consuming. It is a normal force model only which means that there are no blade profile losses involved, hence the volumetric source terms only need to account for the turning of the relative flow in the circumferential direction.

The source distributions are solely dependent on the local flow conditions and the blade geometry [12]. The blade geometry is characterized by the "blade camber" information which is fed to the model in the form of a blade camber surface normal distribution, $\hat{n}(x, r)$. In a 2D sense, the camber is a line joining the leading and trailing edges of an aerofoil, equidistant from the upper and lower surfaces as shown in Figure 2.2. These lines stacked up together through the span of a 3D blade form the camber surface.
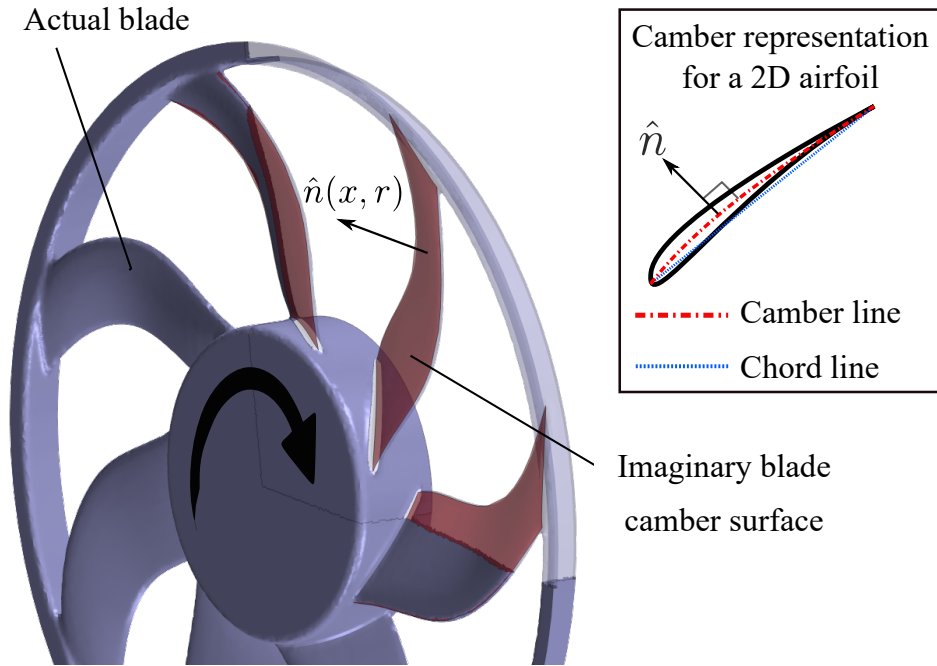
Figure 2.2: Illustration of camber surface of a fan blade

The momentum source, f_n, scales with the square of the relative velocity, $\vec{W}$, and the deviation angle, δ, of the local flow from the blade camber surface. The normal force, responsible for flow turning, is defined per unit mass as,

$$|\vec{f_n}| = \frac{(2\pi\delta)(\frac{1}{2}|\vec{W}|^2/|\hat{n}_\theta|)}{2\pi r/B} \tag{2.1}$$

where $\vec{W}$ is the relative velocity vector, δ is the local flow deviation (with respect to the imaginary blade camber surface), $\hat{n}_\theta$ is the circumferential component of the local blade camber surface normal and B is the number of blades. Figure 2.3a depicts the imaginary blade camber surface and the local camber surface tangent plane at a general point in the body force region. The force acts in a direction which is perpendicular to the local relative velocity streamline and acts to reduce the deviation, δ. The force acts in a plane shared by the blade camber surface normal and the relative velocity vector as depicted in Figure 2.3b. For uniform inflow, the model produces a circumferentially-averaged version of the actual flow field.
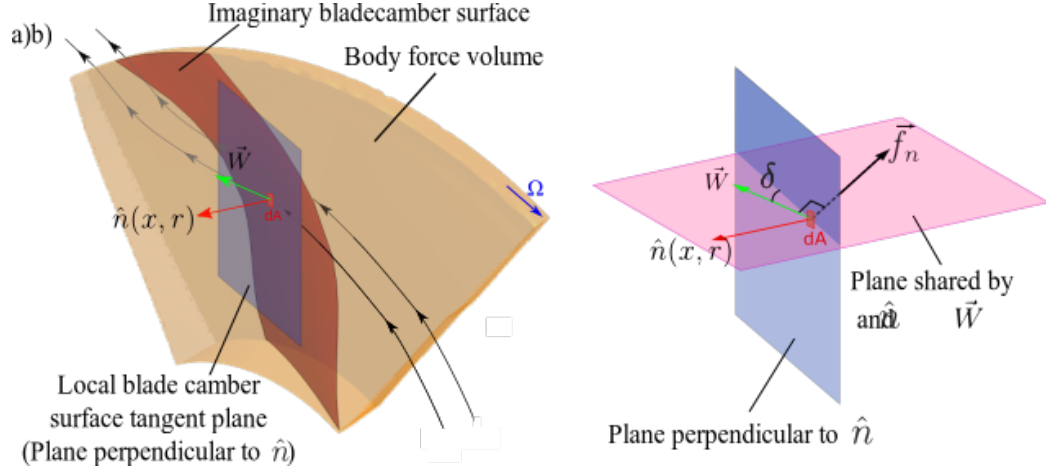
Figure 2.3: a) Illustration of local camber surface tangent plane and camber surface normal $\hat{n}$; b) geometric layout of the relative velocity vector $\vec{W}$, blade camber normal $\hat{n}$, deviation δ and momentum source $\vec{f}_n$

2.3 Implementation of Body Force Model in OPENFOAM v6

This section details the implementation of Hall's body force model using the `fvOptions` functionality in OPENFOAM v6. `fvOptions` allows the user to manipulate the equation systems by adding sources/sinks, imposing constraints and applying corrections without making any changes to the solver application [19]. This work makes use of the `vectorCodedSource` type in `fvOptions` to implement the body force momentum source as computed by Hall's model. For calculating the source terms based on the definition of Hall's model, the `fvOptions` code requires the following inputs:

- cell coordinate information (r, θ, x),

- local velocity field $\vec{U}$,

- turbomachinery features such as number of blades B, rotation rate of the component Ω, and the blade camber surface normal distribution $\hat{n}(x, r)$.

The cell coordinate information (r, θ, x) can be obtained from the mesh information. The local velocity field $(\vec{U})$ can be accessed from the time directories for each iteration and the scalar quantities (B and Ω) can be directly specified in the body

of the `fvOptions` code. Once the blade camber information is fed to the model, the rest of the quantities specified in Equation 2.1 can be easily derived (see Appendix A for details). However, the specification of the blade camber information within the `fvOptions` code poses several constraints/challenges.

Mathematically, the blade camber information contains values of the camber surface normal unit vectors specified in cylindrical coordinates. Due to the axisymmetric nature of the body force geometry, these values are a function of the axial and radial coordinates only, and are defined on a coarse set of scattered data points in 2D space in the form of lookup tables as depicted in Figure 2.4.

```
//(    x        RADIUS       nr )    //(    x        RADIUS       nth )    //(    x        RADIUS       nx )
 (                                    (                                    (
 (   0.00541909  0.08799994   0.42436949 )  (   0.00541909  0.08799994  -0.33954924 )  (   0.00541909  0.08799994  -0.83941459 )
 (   0.00493391  0.08799994   0.17063719 )  (   0.00493391  0.08799994  -0.08563229 )  (   0.00493391  0.08799994  -0.98160586 )
 (   0.00511942  0.08799994  -0.05710058 )  (   0.00511942  0.08799994   0.15377169 )  (   0.00511942  0.08799994  -0.98645516 )
 (   0.00541708  0.08799994  -0.10976241 )  (   0.00541708  0.08799994   0.21793031 )  (   0.00541708  0.08799994  -0.96977244 )
 .                                    .                                    .
 .                                    .                                    .
 .                                    .                                    .
 .                                    .                                    .
 .                                    .                                    .
 (   0.02379370  0.22699982  -0.08909939 )  (   0.02379370  0.22699982   0.05495641 )  (   0.02379370  0.22699982  -0.99450545 )
 (   0.02385229  0.22699982  -0.07664737 )  (   0.02385229  0.22699982   0.02140302 )  (   0.02385229  0.22699982  -0.99682852 )
 )                                    )                                    )
```

Figure 2.4: Example of lookup tables for the values of $\hat{n}_r$, $\hat{n}_\theta$ and $\hat{n}_x$ (left to right) tabulated against axial position, x and radial position, r

The constraints/challenges faced while inputting the blade camber information to `fvOptions` are:

- mapping these values to the simulation grid using lookup tables requires a robust interpolation routine, but there is no inbuilt capability to interpolate volume fields in OpenFOAM v6;

- this interpolation routine ideally should not be a part of `fvOptions` code which is executed for every iteration as it would lead to an unacceptable increase in simulation run time; and therefore

- the implementation has to be structured such that the mapping procedure occurs outside of `fvOptions`, executes only once per simulation to avoid duplicating effort and is available for access by `fvOptions`.

The first of these problems called for the linking of external C++ libraries to OPENFOAM v6 which could perform the specified interpolation in a simple manner. For this purpose, the 2D and Surface Function Interpolation package of the Computational Geometry Algorithms Library (CGAL) was used [25]. Please see details in Appendix A to see how the library was linked to OPENFOAM v6.

The other two requirements were met by introducing camber normals as a separate volume field (called `volVectorField` in OPENFOAM v6 terminology) via the addition of a new field named `camber` to the solver `simpleFoam`. This modified solver will be referred by the name `fsimpleFoam` throughout this chapter. Just like any other field, such as pressure `p` or velocity `U`, the `camber` field has to be initialized for the first iteration. This was achieved by performing the interpolation process inside the `0/camber` file using the OPENFOAM v6 directive `#codeStream` (see Appendix A for details). The `#codeStream` directive makes use of the CGAL interpolation functions to map the camber normal values from the lookup tables (specified in .dat files in the case setup folder) to the cell volumes. The `camber` field carries values of the interpolated blade camber normals for the cells belonging to the body force volume and assigns a value of zero to the cells lying outside the body force volume. The field stays constant throughout a given simulation and the solver automatically copies the calculated field file through each iteration so that `fvOptions` can access it easily from the time directories. The only drawback to this procedure is that it might lead to storage/memory issues for large simulations, especially where turbomachinery is only a small part of the domain since the `camber` field contains numeric values for each cell in the domain. However, the acceleration in simulation time achieved by this process is considered to be a fair trade-off for the increased memory usage.

Once all these inputs are provided to `fvOptions`, it performs the required calculations for the momentum source terms, which are then passed on to the governing equations contained in the `fsimpleFoam` solver (see Appendix A for complete details).

The flowchart presented in Figure 2.5 depicts the flow of data into and out of `fvOptions` as detailed above.
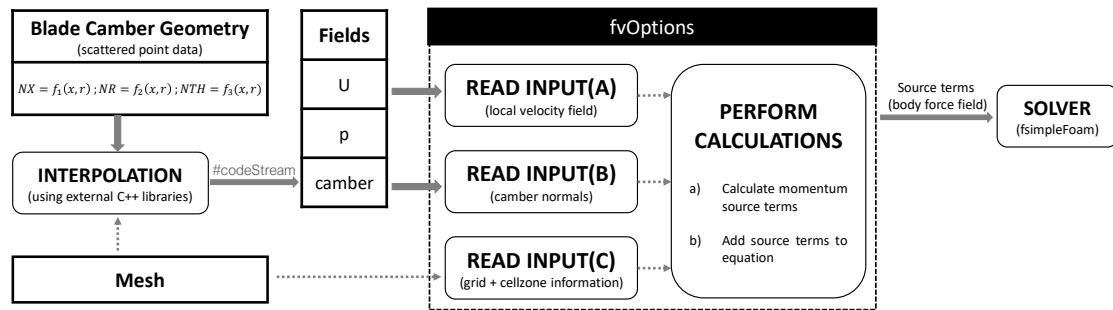
Figure 2.5: Calculation of source terms using `fvOptions`

2.4   Implementation of Body Force Model in Star-CCM+

STAR-CCM+ has several pre-defined turbomachinery-specific options capable of simulating the actuator disks as well as body force models. Since Hall's model is an analytical approach, the pre-defined *fan momentum source* template in STAR-CCM+ can not be employed as it requires fan pressure curves. None of the options under the virtual disk method can be used to implement Hall's model either.

Hence, the source term calculations were performed by using user-defined field functions. The cell coordinate information and the local velocity field, $\vec{U}$ can be easily accessed using field function expressions. The turbomachinery specific variables (number of blades, B and the rotation rate of the turbomachinery, Ω) were defined as *Parameters* to separate them from the intermediate field functions, and to make the setup modular and easy to use for someone who is not completely familiar with the calculation procedure.

To input the blade camber surface normal distribution, $\hat{n}(x, r)$, field functions were created which could map the values of the camber normal components from a lookup table (created in a similar fashion as the ones used for OpenFOAM v6) to the simulation grid using the `interpolateTable` function. Star-CCM+ does not have the capability to interpolate a field as a function of two independent variables. It can perform 3D spatial interpolation using a closest neighbour method only. The absence of a general interpolation routine is a major drawback to using Star-CCM+ for implementing general body force models.

Although Star-CCM+ has an easy-to-use graphical-user interface (GUI), attaching external user libraries or reading external files can be a tedious process. Attempts to introduce the CGAL library [25] as well as a hard-coded linear interpolation code through Star-CCM+ user libraries to map a coarsely-defined camber field to the simulation grid met with challenges due to the absence of any robust inbuilt debugger in Star-CCM+. The constraint of performing a closest-neighbour interpolation for the camber field requires the lookup table to have scattered data in all 3 dimensions (even though camber normal values are a function of x and r only), and to have a resolution at least as fine as the grid spacing to ensure accuracy. This can be a problem for large simulation cases with hundreds of thousands of cells which require a high amount of RAM for closest-neighbour interpolation. Moreover, a new table has to be created for any simulation which uses a different grid (even if it is for the same turbomachine) to ensure adequate resolution. In this aspect, OpenFOAM v6 offers a more flexible approach by allowing attachment of external libraries to interpolate fields from a coarsely-defined data set to any resolution of grid in a modular way.

For large simulation cases where the introduction of a fine lookup table is impossible, a workaround has been found by the author which has been described in Chapter 4, Section 4.6.2. The full list of user-defined field functions, parameters and examples of tables used in Star-CCM+ can be found in Appendix B.

2.5   Numerical Details for the Test Cases

This section describes the geometry and computational domains of the two fans used to test the performance of Hall's body force model in OPENFOAM v6 and STAR-CCM+. The first fan is the low-speed Whittle aircraft engine rig fan model which has been frequently used to study boundary layer ingesting (BLI) propulsion system behavior [11–16]. The second fan is an automotive radiator fan used for vehicle cooling applications [7]. The two axial fans chosen as test cases have very different design characteristics as evident from Table 2.1.

Table 2.1: Design characteristics for the test fan models

Parameter	Whittle BLI Fan	Automotive Cooling Fan
Machine type	Rotor and stator, with rotor tip gap	Shrouded rotor only, with no tip gap
Number of blades, B	20 rotor blades, 30 stator vanes	7
Rotor inlet hub-to-tip ratio, r_{hub}/r_{tip}	0.3	0.388
Design rotational speed, N	1800 rpm	2683 rpm
Rotor tip relative Mach, M_{tip}	0.13	0.19
Design flow coefficient, $\phi_{des} = \bar{u}_x^M/U_{\mathrm{mid}}$	0.5	0.215
Design total enthalpy rise, $\psi = \Delta\bar{h}_{\mathrm{t}}^{\mathrm{M}}/U_{\mathrm{mid}}^2$	0.47	0.13

The design flow coefficient is defined as the ratio of the mass-averaged inlet velocity, $\bar{u}_x^M$, to the midspan blade speed, U_{mid}, at design operating point. The design total enthalpy rise is the mass-averaged total enthalpy change, $\Delta\bar{h}_{\mathrm{t}}^{\mathrm{M}}$, non-dimensionalized by the square of the midspan blade speed, U_{mid} at design point.

2.5.1 Whittle Laboratory Low-speed Rig Fan

The geometry used for this work is the same low-speed fan employed by Hall et al. for the study of inlet distortions in boundary layer ingesting (BLI) fans. Figure 2.6 shows a meridional (axial-radial) view of the fan stage geometry and the computational domain. The body force computational domain extends two diameters upstream of the spinner tip and downstream of the stator. A 22.5° wedge-shaped geometry was created by using POINTWISE [26], with cyclic (periodic) boundary conditions.
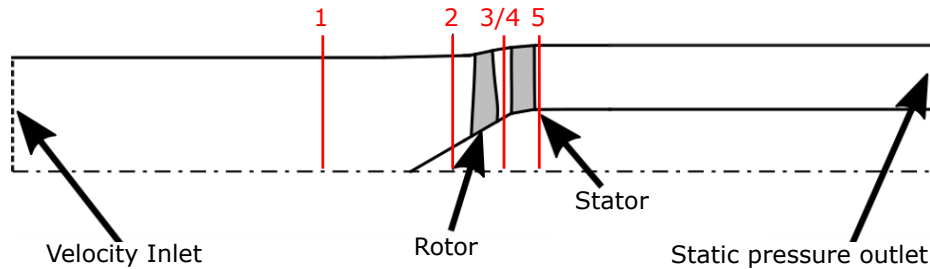
Figure 2.6: Meridional view of Whittle fan geometry and computational domain with measurement plane locations (Adapted from Defoe et. al [13])

2.5.2 Shrouded Automotive Fan

The fan geometry examined in this case is a 7-bladed, shrouded automotive cooling fan filleted at the hub and the tip. A schematic meridional view of the computational geometry and the axial measurement planes is given in Figure 2.7. The body force computational domain is a simple 2° wedge which is representative of a simple annular duct with the hub and casing radii equal to those of the fan throughout [2]. The domain extends about two spans upstream and three spans downstream of the blade row.

---

[2] For the Whittle fan, a 22.5° wedge geometry was used, as opposed to a 2° wedge used for the automotive fan, because ANSYS CFX was found to yield inaccurate results for a single-cell thick wedge. Moreover, the automotive radiator fan computational domain has a constant radius hub for the inlet portion as opposed to the converging inlet used for the Whittle fan. The presence of a computational domain which touches the rotational axis (converging inlet portion for the Whittle fan) may require a complex butterfly structure to create a mesh in the vicinity of the rotation axis. To avoid this complexity, a simple straight annular duct type computational domain is used for the automotive fan.
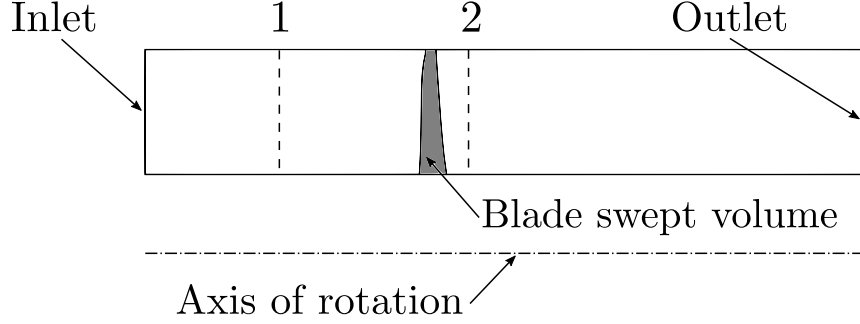
Figure 2.7: Meridional view of the automotive radiator fan geometry and computational domain (Adapted from Saini and Defoe [7])

2.5.3 Performance Metrics of Interest

The metrics of interest for comparison of body force model performance between different solvers in this chapter are the work coefficient of the fan and the total pressure rise coefficient. The work coefficient is defined as:

$$\psi = \frac{\Delta \bar{h}_\mathrm{t}^\mathrm{M}}{U_M{}^2} \tag{2.2}$$

where $\Delta \bar{h}_\mathrm{t}^\mathrm{M}$ is the mass-averaged total enthalpy change across the fan, and $U_\mathrm{M} = \omega r_\mathrm{mid}$ is the midspan blade speed. ω is the angular velocity of the rotor. The total enthalpy is simply defined from the Euler turbine equation as $h_\mathrm{t} = \omega r u_\theta$ where the tangential velocity u_θ is calculated directly from the velocity field. The far-upstream flow is axial so the upstream total enthalpy, $\bar{h}_\mathrm{t,1}^\mathrm{M}$, is defined to be zero. The total pressure coefficient is defined as:

$$\psi_{tt} = \frac{\Delta \bar{p}_\mathrm{t}^\mathrm{M}}{\rho U_M{}^2} \tag{2.3}$$

where $\Delta \bar{p}_\mathrm{t}^\mathrm{M}$ is the mass-averaged total pressure change between the upstream and the downstream measurement plane locations. For Hall's original body force model, $\psi = \psi_{tt}$ because there are no total pressure losses and thus the fan is operating at 100% efficiency.

2.5.4   Details of Computational Setup

For both test cases, the hub and casing surfaces are defined as free-slip zero shear stress walls and the fluid viscosity is set to zero for modelling inviscid flow. The velocity-inlet boundary condition has flow incoming normal to the boundary and the outlet static pressure is fixed. Calculations were performed in OPENFOAM v6 using the `fsimpleFoam` solver. The volumetric source terms are calculated within the rotor and stator zones for each iteration and then added to the governing equations.

A grid independence study was performed on both domains with grid converged results obtained using 4.4 million cells for the Whittle fan case, and $3.5X10^5$ cells for the automotive fan. For the Whittle fan, the grid independence was checked based on the convergence of the total enthalpy rise coefficient at the design operating point and also for the convergence of the radial profiles of flow deviation to ensure that the local flow features were also grid-independent (see Figures 2.8a and 2.9). For the automotive fan, the grid was successively refined until the total enthalpy rise coefficient at the design operating point was grid-independent to three decimal places (see Figure 2.8). Moreover, the grid convergence for the automotive fan was judged to be accurate based on the Richardson extrapolation method, the details of which can be found in Chapter 3, Section 3.3.5.

The camber surface normal distributions were specified in the form of lookup tables (as shown in Figure 2.4) which contain information about the camber surface normal values defined on a coarse set of scattered data points as a function of the axial (x) and radial (r) positions only. The values are automatically interpolated to the grid at the start of the simulation using a high-order interpolation routine.
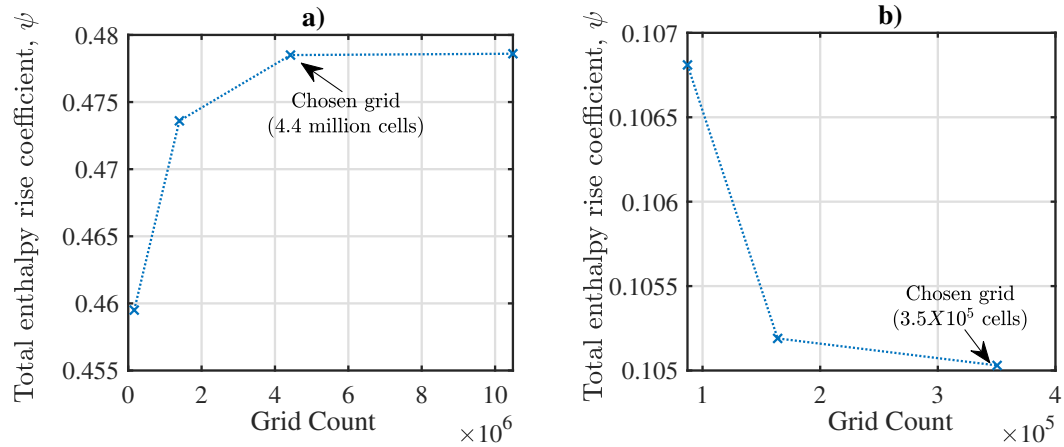
Figure 2.8: Grid convergence study for the total enthalpy rise coefficients at the respective design points for a) Whittle fan, and b) automotive radiator fan
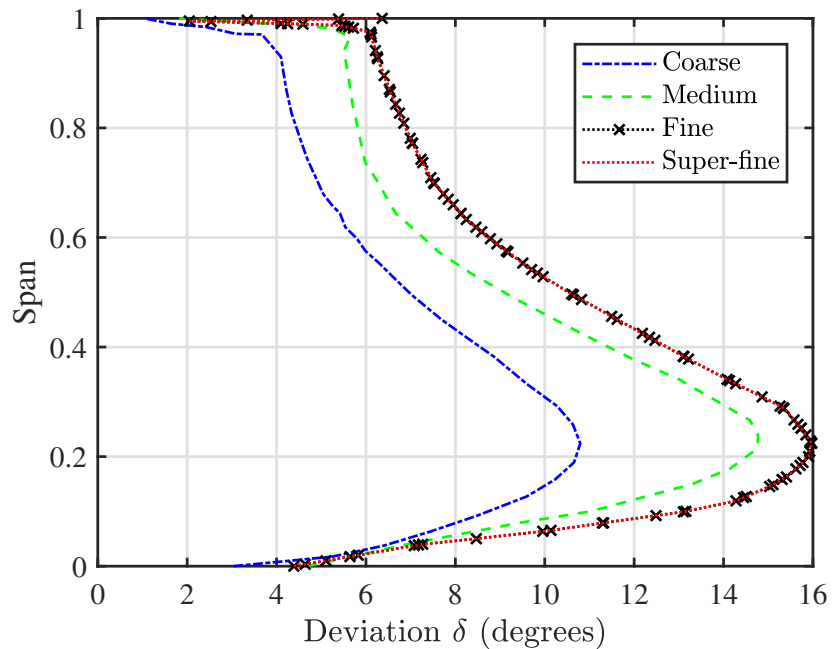
Figure 2.9: Spanwise profiles of the rotor trailing edge deviation, δ for the four grid counts shown in Figure 2.8(a) obtained at plane 3/4 for the Whittle fan operating at design point

2.6 Results and Validation

This section provides details of the results obtained from the OPENFOAM v6 simulations. The Whittle fan case is compared to a similar simulation case which was performed in ANSYS CFX [3]. The experimental data available in the literature for the Whittle fan has been used as a reference solution to validate the body force model implemented in OPENFOAM v6 [27, 28]. For the automotive fan, the results are compared against an identical simulation performed in STAR-CCM+ [4]. One of the major differences between the commercial codes ANSYS CFX and STAR-CCM+ [4], and the open-source software OPENFOAM v6 is that the latter is a cell-centered code whereas both the commercial solvers are node-centered.

2.6.1 Whittle Laboratory Low-speed Rig Fan

Table 2.2 shows a comparison of the experimentally measured stage total enthalpy rise characteristics for the design point, as well as the ones obtained from ANSYS CFX and OPENFOAM v6.

Table 2.2: Total enthalpy rise coefficients for the Whittle Fan

Results from	Total Enthalpy Rise Coefficient
Experiments	0.469
ANSYS CFX	0.483
OPENFOAM v6	0.470

For the numerical results, the total pressure rise and total enthalpy rise coefficients are equivalent since there are no losses in the blade rows. OPENFOAM v6 yields a total enthalpy rise coefficient closer to the experiments as compared to the one obtained from ANSYS CFX. Since both numerical results are grid-independent for their respective solvers, it indicates that the disparity in the values comes from the inherent differences in the nature of the two solvers. Besides the fact that OPEN-FOAM v6 is a cell-centered code whereas ANSYS CFX is a node-centered code,

ANSYS CFX also differs in the sense that it solved the equations with a compressible flow solver (even though Mach < 0.3 everywhere for our case). This difference could be the reason for the deviation in the results.

Figures 2.10 shows a comparison of the spanwise distributions of pitchwise averaged rotor inlet and exit axial velocity at the stage design point obtained from OpenFOAM v6 [19] and ANSYS CFX [3]. None of the solvers are able to capture the sharp gradient in the axial velocity values in the outer 20% of the span because they do not model the rotor tip gap. However, there are negligible differences in the overall values of axial velocity predicted by the two solvers in the inner 80% span.
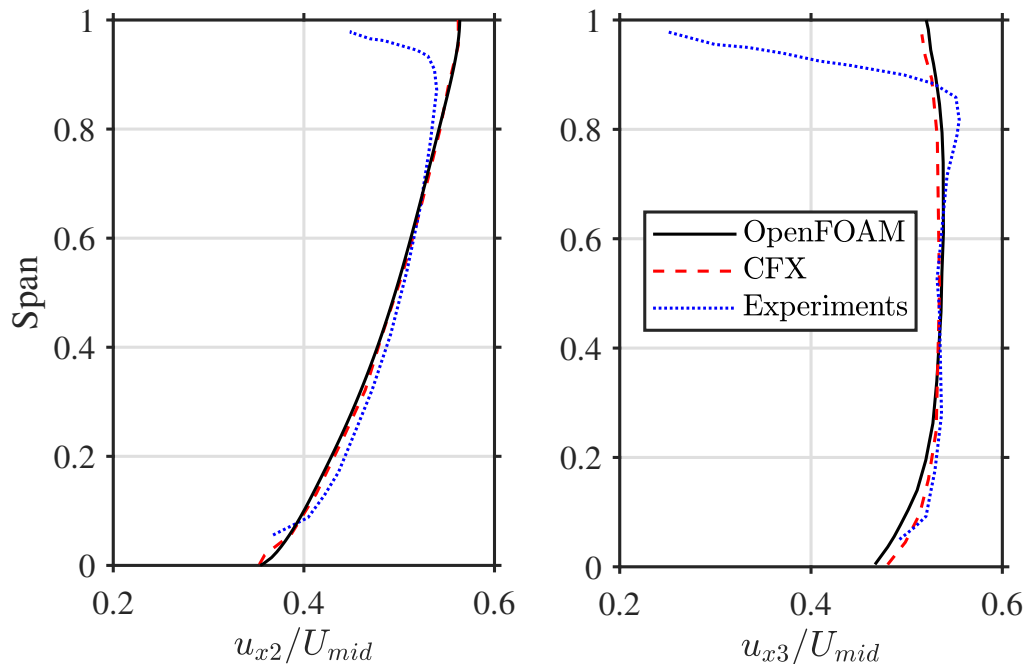
Figure 2.10: The axial velocity profiles obtained from OpenFOAM v6, ANSYS CFX and experimental data just upstream and downstream of the rotor for the Whittle fan at the design operating point

The circumferential velocities obtained just upstream and downstream of the stator for the two solvers are also shown in Figure 2.11. The profiles predicted by OpenFOAM v6 are at an almost constant offset of ~0.015 for plane 4 and ~0.004

for plane 5. from the ones obtained from ANSYS CFX. OPENFOAM v6 predicts higher flow turning at the end of the rotor (upstream of stator), thereby doing more work, and takes out a higher amount of swirl from the flow as it passes through the stator. This explains the higher total enthalpy rise observed for the OPENFOAM v6 case.
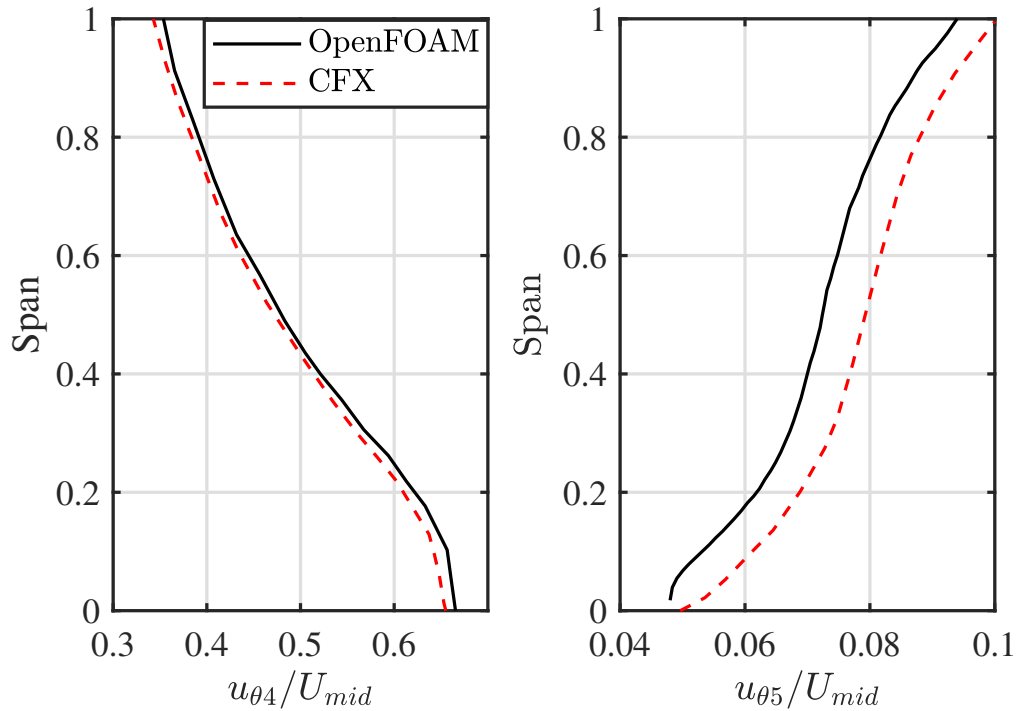
Figure 2.11: The tangential velocity profiles obtained from OPENFOAM v6 and ANSYS CFX just upstream (plane 3/4) and downstream (plane 5) of the stator for the Whittle fan at design operating point

2.6.2 Automotive Radiator Fan

Figure 2.12 shows the fan characteristics for the automotive radiator fan as obtained from the body force model implementations in OPENFOAM v6 and STAR-CCM+ [4] respectively. STAR-CCM+ [4] achieved grid convergence at the same mesh resolution as the one obtained for OPENFOAM v6. Results obtained from the solvers were compared to single-passage bladed multiple-reference frame (MRF) computations, the details of which can be found in Chapter 3. Although the body force

models in both solvers under predict the fan work coefficient significantly, there are negligible differences in the values obtained from the two solvers.
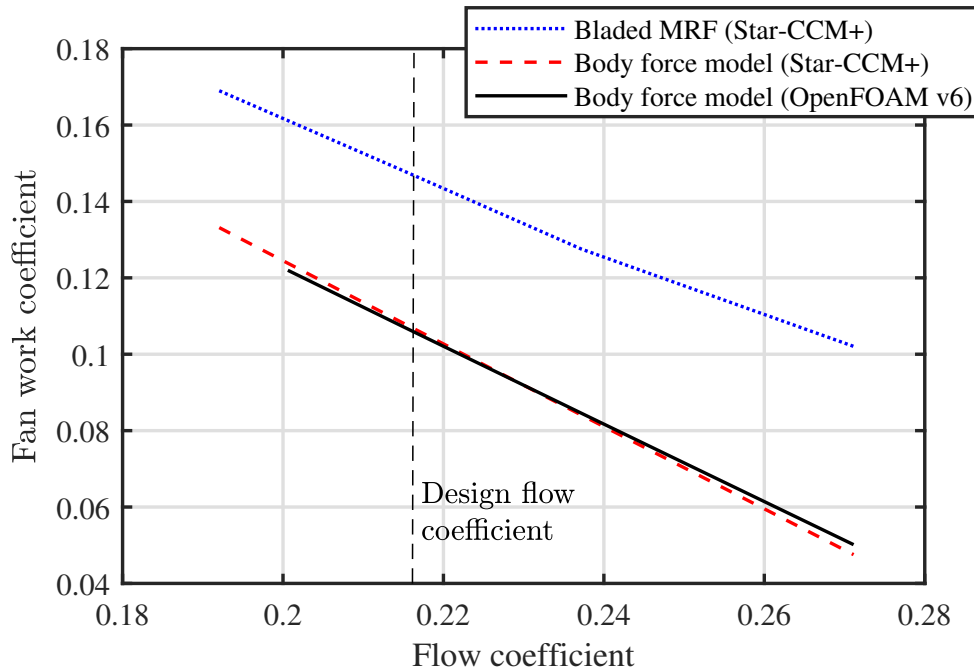
Figure 2.12: Fan characteristic curves obtained from OPENFOAM v6 and STAR-CCM+ [4] for the automotive radiator fan

Figures 2.13 and 2.14 show the spanwise profiles of the cylindrical velocity components, and the total pressure rise coefficient, and work coefficient profiles obtained from the two solvers. Despite the excellent agreement of the overall fan work coefficient yielded by the body force model for the two solvers, there are significant differences in the shapes of the velocity profiles. This could indicate that the two body force model formulations perceive different blade camber geometries owing to the differences in the way interpolation (for the camber normals) was performed in the two solvers. Despite the velocity disagreement, the total pressure rise coefficient, and the fan work coefficient have negligible differences especially in the outer 50-60% of the span as shown in Figure 2.14.
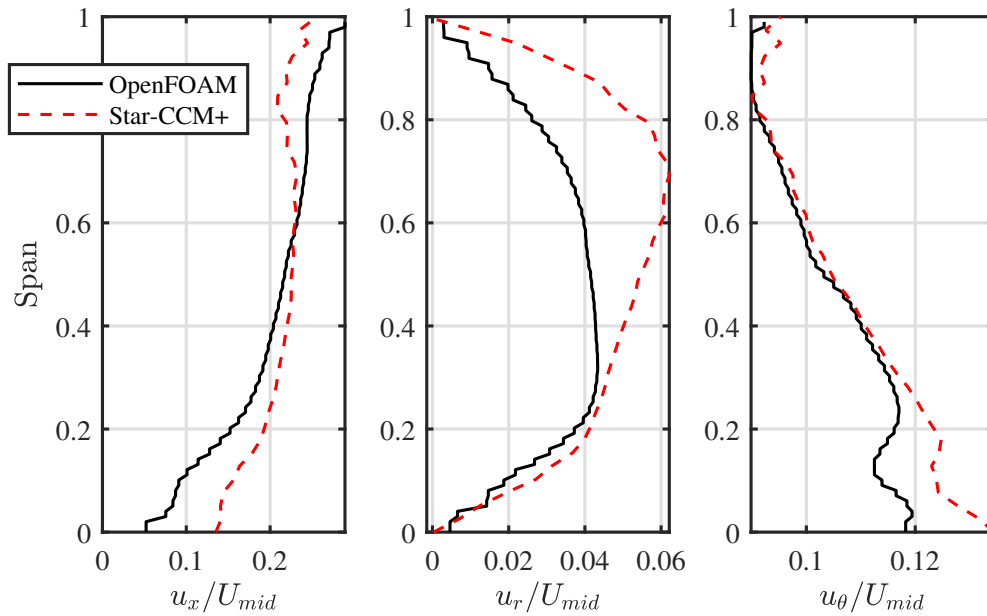
Figure 2.13: The velocity components obtained from OPENFOAM v6 and STAR-CCM+ [4] at the downstream plane for the automotive radiator fan at design operating point
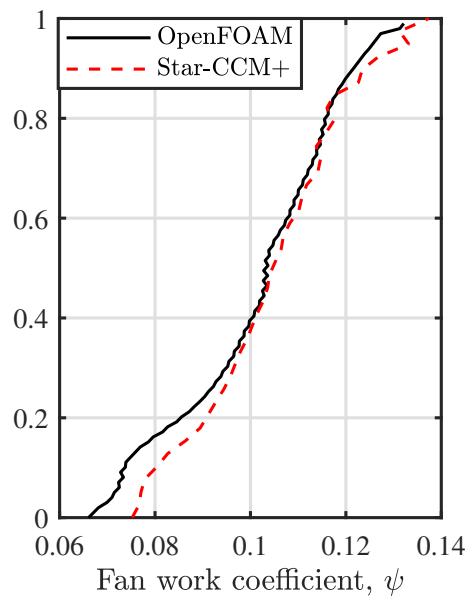
Figure 2.14: The total pressure rise coefficient and work coefficient profiles obtained from OPENFOAM v6 and STAR-CCM+ [4] at the downstream plane for the automotive radiator fan at the design operating point

2.7 Summary and Conclusion

This work illustrated the implementation of an uncalibrated body force model approach for axial fans in the open-source software OPENFOAM v6 [19] and the commercial code STAR-CCM+ [4]. The model was tested for two different configurations of axial fans, i) an aircraft engine fan with a high blade count and high work coefficient, and ii) an automotive radiator fan with low blade count and low work coefficient.

The most challenging part of the model implementation was the mapping of blade camber surface normal values from a lookup table to the simulation grid. A modified, incompressible flow solver `fsimpleFoam` was used to trigger the mapping process in OPENFOAM v6 [19] using the external library CGAL [25], and the source term calculations were performed using the `fvOptions` utility. In STAR-CCM+ [4], the mapping process was performed using closest-neighbour interpolation from lookup tables while the rest of the calculations were performed using field functions. The results obtained from OPENFOAM v6 were compared to available data from experiments, higher-fidelity simulations, and body force model data from commercial CFD solvers STAR-CCM+ and ANSYS CFX [3].

OPENFOAM v6 [19] was found to yield results as good as, or even better, than the commercial CFD solvers while offering the most flexibility by allowing attachment of a robust interpolation library for the mapping process. The ANSYS CFX [3] results were solved in a compressible sense. This behavior may have led to the slight deviations between the results obtained from OPENFOAM v6 and ANSYS CFX. STAR-CCM+ [4] was found to have a major drawback because of its inability to perform a general spatial interpolation of camber normal values as a function of two position variables (x and r) only. However, the overall turbomachinery performance characteristics were well-matched between OPENFOAM v6 and STAR-CCM+.

This work proves the suitability of OPENFOAM v6 [19] as a solver for implementing body force models and also provides a template for executing volumetric source term models in general, an important turbomachinery-specific capability which is largely missing from the existing collection of OPENFOAM v6 "turbo-tools" [19]. Nevertheless, there are several improvements/modifications that can be introduced in the current model implementation, the full details of which can be found in Chapter 5, Sec. 5.3.

2.8   Acknowledgments

References

[1] James Tyacke, NR Vadlamani, W Trojak, R Watson, Y Ma, and PG Tucker. Turbomachinery simulation challenges and the future. *Progress in Aerospace Sciences*, 110:100554, 2019.

[2] Hrvoje Jasak and Martin Beaudoin. Openfoam turbo tools: From general purpose CFD to turbomachinery simulations. In *Fluids Engineering Division Summer Meeting*, volume 44403, pages 1801–1812, 2011.

[3] ANSYS Inc. *ANSYS v18.2 User's Guide*. ANSYS Inc., Canonsburg, PA, 2019.

[4] Simcenter Star-CCM+ user guide v13. 04. *Siemens PLM*, 2018.

[5] Jing Liu, Htet Lin, and Srinivasa Rao Purimitla. Wake field studies of tidal current turbines with different numerical methods. *Ocean Engineering*, 117:383–397, 2016.

[6] Itsuhei Kohri, Yuji Kobayashi, and Yukio Matsushima. Prediction of the performance of the engine cooling fan with CFD simulation. *SAE International Journal of Passenger Cars-Mechanical Systems*, 3(2010-01-0548):508–522, 2010.

[7] Palak Saini and Jeff Defoe. The effect of blade count on body force model performance for axial fans. In *Turbo Expo: Power for Land, Sea, and Air*, 2020.

[8] Dirk Baeder, Thomas Indinger, Nikolaus Adams, and Friedhelm Decker. Comparison of numerical simulations with experiments of bluff bodies including under-hood flow. Technical report, SAE Technical Paper, 2011.

[9] Nicolas Francois. Using CFD for heat exchanger development and thermal management. *Valeo Engine Cooling, EACC, Frankfurt, Germany*, 2005.

[10] Boundary layer ingestion propulsion, Nov 2019.

[11] David K Hall. *Analysis of civil aircraft propulsors with boundary layer ingestion*. PhD thesis, PhD Thesis, MIT, 2015.

[12] DK Hall, EM Greitzer, and CS Tan. Analysis of fan stage conceptual design attributes for boundary layer ingestion. *J. Turbomach.*, 139(7):071012, 2017.

[13] JJ Defoe, M Etemadi, and DK Hall. Fan performance scaling with inlet distortions. *J. Turbomach.*, 140(7):071009, 2018.

[14] David Jarrod Hill. Compressor performance scaling in the presence of non-uniform flow. 2017.

[15] Sho Sato, Nathan Spotts, and Xinfeng Gao. Validation of fan source term model constructed without blade geometry. In *Proceedings of the AIAA Scitech 2019 Forum*, page 1448. AIAA, 2019. AIAA paper 2019-1448.

[16] Emmanuel Benichou, Guillaume Dufour, Yannick Bousquet, Nicolas Binder, Aurélie Ortolan, and Xavier Carbonneau. Body force modeling of the aerodynamics of a low-speed fan under distorted inflow. *Int. J. Turbomach. Propuls. Power*, 4(3), 2019.

[17] Andreas Peters, Zoltán S Spakovszky, Wesley K Lord, and Becky Rose. *Ultrashort nacelles for low fan pressure ratio propulsors*, volume 45578. American Society of Mechanical Engineers, 2014.

[18] Marc Latour. Body force modeling of axial turbomachinery for analysis and design optimization. 2020.

[19] The OpenFOAM Foundation. OpenFOAM v6, 2019.

[20] TCFD 17.06 parallel scaling francis hydro-turbine 2017, Jun 2017.

[21] Tony Burton, David Sharpe, Nick Jenkins, and Ervin Bossanyi. *Wind energy handbook*, volume 2. Wiley Online Library, 2001.

[22] M Paul van der Laan, Niels N Sørensen, Pierre-Elouan Réthoré, Jakob Mann, Mark C Kelly, and Niels Troldborg. The k-ε-fp model applied to double wind turbine wakes using different actuator disk force methods. *Wind Energy*, 18(12):2223–2240, 2015.

[23] Stefano Wahono. Development of virtual blade model for modelling helicopter rotor downwash in openfoam. Technical report, Defence Science and Technology Organisaion Fisherman's Bend (Australia), 2013.

[24] Alexandre Capitao Patrao. Description and validation of the rotordisksource class for propeller performance estimation. Technical report, Chalmers University of Technology, 2017.

[25] The CGAL Project. *CGAL User and Reference Manual*. CGAL Editorial Board, 5.0.2 edition, 2020.

[26] Pointwise. *Pointwise v18.3R1 User's Manual*. Pointwise, Forth Worth, TX, 2019.

[27] Ewan J Gunn, Sarah E Tooze, Cesare A Hall, and Yann Colin. An experimental study of loss sources in a fan operating with continuous inlet stagnation pressure distortion. 135(5), 2013.

[28] EJ Gunn and CA Hall. Aerodynamics of boundary layer ingesting fans. In *Turbo Expo: Power for Land, Sea, and Air*, volume 45578, page V01AT01A024. American Society of Mechanical Engineers, 2014.

Chapter 3

The Effect of Blade Count on Body Force Model Performance for Axial Fans

3.1 Introduction

The accurate prediction of automotive fan performance is a critical step in developing the vehicle thermal management system since it underpins the design of the entire vehicle cooling module, and is critical for sizing, designing, and optimizing the heat exchangers and the rest of the components lying in the path of the cooling airflow. Due to the complexity of the under-hood architecture in modern vehicles, even slight flow non-uniformities and deviations from assumed geometry can have a significant impact on the under-hood and under-body cooling flows [1]. This makes it imperative to consider both the external and the internal flow in the entire front-end cooling module to be able to correctly predict the performance of the automotive fan [2]. However, the complications associated with using experimental measurement techniques to correctly predict the fan performance in a tightly-packed under-hood compartment has led to an increased focus on the development of computational fluid dynamics (CFD) fan models which respond realistically when installed in an under-hood environment [1].

Transient drive cycles are typically simulated in CFD in the automotive industry to assess component thermal responses under challenging and variable conditions [3]. The time scale for the flow to move through the fan is orders of magnitude smaller than the time scale for the overall external flow around the vehicle. This means

that time step sizes in the CFD required for resolving the flow through the fan are much smaller than those needed to resolve the flow around the vehicle. As a result, modeling the blades directly would yield unacceptably long run-times for the full vehicle computations. This has led to the development of multiple types of simplified CFD models which can inexpensively predict the fan performance, with varying levels of fidelity and calibration, in transient vehicle test-drive cycles.

The actuator disk approximation is one such technique, popular in both the automotive as well as the aerospace CFD community. It is used to predict the fan pressure rise by assuming the fan to be an infinitely thin momentum source, across which the fluid properties change discontinuously. The fan curve models utilized by Natarajan et al. [4] and Kim and Kim [5] exemplify the simplest form of actuator disks which make use of experimentally derived pressure rise vs. volumetric flow rate curves to calibrate the fan model. There are several variants of the actuator disk models available in the literature, however most of these techniques require calibration with some form of experimental or higher fidelity data, or suppress either (or both) of the radial or tangential components of the velocity field [6–9]. Multiple studies have pointed out that neglecting the radial flow through a fan subjected to inlet distortions can lead to erroneous results [10, 11]. This makes the actuator disk approximation unsuitable for use in a tightly packed under-hood environment where flow blockage upstream or downstream of the fan can create significant radial and circumferential flow non-uniformities.

Another common approach in the automotive CFD community is the multiple-reference frame (MRF) model which, unlike actuator disks, requires significant computational effort since the detailed fan geometry is included. This approach essentially uses a "frozen rotor" technique to predict the fan performance. The MRF method requires the user to define a volume containing the rotor blades within which the

governing equations are solved in the rotating reference frame of the fan. This enables steady state computations to be performed without a need for mixing planes [12]. There are, however, several limitations to this model. For instance, the MRF technique is suitable for problems where no large-scale transients are present since it is a steady state technique [13]. This means it cannot be directly applied for the transient drive cycles of interest. It has also been shown that uniform "mixed-out" inflow conditions are necessary to get an accurate prediction of fan performance with the frozen rotor method [14]. This means that the MRF technique is unsuitable for an automotive fan operating in a convoluted and complex under-hood geometry, even if the overall flow conditions are steady. Additionally, the MRF technique cannot represent the true time-averaged effect of the fan on the flow field since the rotor is modeled as being "frozen" in a particular clocking position. The variation of fan performance with the choice of clocking position becomes more significant for rotors with lower blade counts; automotive fans tend to have less than 10 blades so this is problematic.

An alternative fan modeling approach is to use a body force field to represent the effect of the fan on the flow. This approach has been widely used in the aerospace community in the modeling of axial fans and compressors [15–20]. Body force modeling involves replacing the blades with body forces in the form of momentum and (for compressible flow) energy source terms. The model therefore does not resolve the detailed flow over the blades but instead captures a "smeared out" version of the blades' effect on the flow. The elimination of physical blades has been shown to reduce the required grid count by about two orders of magnitude [19] and, more importantly, it is able to predict the "quasi-steady" effect of the fan on the flow field even in cases of non-uniform flow. This eliminates the problem of disparity in time scales associated with the non-uniform flow through a fan and the transient drive cycles of the full vehicle. The body force modeling approach was initially conceptualized by Marble [21],

however a multitude of variations of the approach have been developed, such as the works of Gong et al. [22], Peters et al. [17], Hall et al. [15], and Benichou et al. [23]. In most of the body force models currently employed by the aerospace community, the source term distribution information is extracted either from single passage, bladed calculations of the flow field or is calibrated using available experimental data. Eliminating calibration of the simplified fan model would significantly reduce the overall effort, time, and cost involved in simulating under-hood and underbody flows.

The approach developed by Hall et. al [15] uses a body force formulation which only requires the blade camber surface geometry information and the local flow conditions to define momentum and energy source terms. It therefore requires neither calibration with experimental data nor high-fidelity simulations to predict the performance of axial fans and is therefore the model of interest in this paper. This model has been applied to study inlet distortions in aircraft engine applications [16, 24, 25] and has also been shown to predict the total enthalpy rise across a low speed fan stage to within an accuracy of 3% [15].

All the above applications and parametric studies utilizing body force models have been restricted to aircraft engine fans and compressors with at least 20 blades per row, while automotive cooling fans often have fewer than half that many. Since the body force model essentially approximates the circumferentially "smeared-out" version of the blades' effect on the flow, the accuracy of the body force model is expected to vary with the number of blades or, equivalently for a given chord, the solidity. Ever-shortening design cycles in the automotive industry provide motivation for implementing a calibration-free fan model. Hall's model is a good candidate, but its accuracy is unproven for fans with low blade counts. Further, there has not been a comprehensive study of the impact of blade count on the accuracy of body force models in general. Therefore, the objectives of this paper are to (1) quantify how changing the number of blades in a fan rotor affects the accuracy of the body force

model's predictions of total enthalpy rise in uniform flow and (2) study the impact of the ratio of length scales between the blade pitch and flow periodicity in non-uniform flow.

One key finding is that a significant reduction of the blade metal blockage effects, combined with the effects of spanwise flow redistribution, drives the body force model to predict more accurate values of the fan work coefficient as the blade count decreases. Another is that the reduction in the number of blades (which also causes a change in the ratio of the length scale of the distortion to the blade pitch) is found to have negligible impacts on upstream influence and distortion transfer in non-uniform inflow until extremely low blade counts (such as 2) are applied, at which point the upstream flow becomes more uniform and the distortion is transferred almost unaltered through the fan.

The remainder of this paper is organized as follows. First, we describe the body force modeling approach, the machine of interest, the computational domain and the numerical details. Then, for the case of uniform inflow for a 7-bladed automotive fan, the computations are carried out at a range of flow coefficients for single-passage bladed and body force simulations. Subsequently, to assess the variation of accuracy of the body force predictions with solidity for uniform inflow, the number of blades in the fan rotor is altered from 5 to 22. Lastly, the model is used to capture distortion transfer in fans with low blade counts to assess the effect of the change of the distortion scale to pitch ratio on upstream influence and distortion transfer.

3.2   Body Force Model

Here a brief description of Hall's body force model is provided. For the complete details, the reader is advised to refer to Hall et al.'s original work [15].

In a body force modeling approach, the physical blades are replaced by forces which yield momentum source terms. These source terms are added to the region

covered by the swept volume of the blades, and are responsible for altering the flow field in the form of pressure changes and flow turning. In general, any body force model formulation can be divided into two parts: (1) a force normal to the relative streamlines which causes the flow turning, and (2) a force parallel to the relative streamlines, responsible for viscous losses. Hall's model is for a normal force only. The fan model thus assumes the flow to be isentropic. Blade profile losses are thus neglected. The action of the rotating blades is modeled as a circumferentially averaged body force (f) that is a function of the square of the local relative velocity magnitude (W) and the deviation angle (δ) between the blade camber surface and the local relative velocity vector. The magnitude of the body force is given by Eq. 3.1 where B is the number of blades, r is the radius measured from the axis of rotation, and n_θ is the circumferential component of the blade camber surface normal. The magnitude of the body force, which represents the blade loading, scales linearly with the number of blades, all else being equal. The calculation of the deviation as well as the direction of application of the force considers the three-dimensional camber surface and velocity field, accounting for any blade lean and giving rise to radial force components when lean is present.

$$|f| = \frac{(2\pi\delta)(\frac{1}{2}W^2/|n_\theta|)}{2\pi r/B} \tag{3.1}$$

There are several instances in the literature of the use of Hall's body force model in conjunction with additional terms which account for the blade profile losses and metal blockage effects [23] as well as compressibility corrections [18, 23, 25]. For instance, Benichou et al. [23] use a modified version of Hall's normal body force formulation given as

$$|f_n| = \frac{K_{Mach}}{b} \frac{(2\pi\delta)(\frac{1}{2}W^2/|n_\theta|)}{2\pi r/B} \tag{3.2}$$

where K_{Mach} is a compressibility correction dependent on the Mach number and b is a parameter which accounts for the change in body force due to the effects of the metal blockage by blades with a finite thickness. b is defined as

$$b = \frac{\theta_{PS} - \theta_{SS}}{2\pi/B} \tag{3.3}$$

where $\theta_{PS} - \theta_{SS}$ represents the passage width (normalized by local radius) from the pressure side of one blade to the suction side of the next blade. The effect of metal blockage is discussed later in more detail.

In this paper we are only interested in incompressible flow, which negates the need for any compressibility correction. Our focus is on the prediction of the fan work coefficient. As will be shown later, the inclusion of shear stresses on the blade surfaces and endwalls has a negligible impact on the total enthalpy rise prediction, and the effect of metal blockage is found to be insignificant for the low blade counts typically seen in automotive fans. Therefore, Hall's original body force model has been implemented in this study without taking any additional loss model or metal blockage effects into consideration. This avoids adding unnecessary complexity to the body force implementation.

The approach used here represents a pitchwise-average of the actual flow field and assumes infinitely-thin blades. Hence, it is expected that a "smeared-out" version of the flow field is more likely to be a good approximation for high blade count (or low pitch) fans where the ratio of the pitch to the length scale of circumferential flow non-uniformities is small. The assumption of infinitely-thin blades implies that the relative velocity magnitude W "perceived" by the body force model is less than the magnitude locally "seen" in a real blade passage; this not only affects the relative velocity but also the blade loading. This effect caused by the finite thickness of the blades is what is referred to as the "metal blockage effect" in the remainder of this paper.

It is important to reiterate here that Hall's original body force model makes two inherent assumptions: (1) the pitchwise-averaged flow field is a good representation for the actual flow field (which is only true for fans with a high blade count), and (2) the relative velocity magnitude "perceived" by the body force model does not change with the blade count, to first order. As the blade count decreases, the flow field becomes increasingly non-uniform in the circumferential direction. However, at low blade counts, there is an improved agreement between the relative velocity field "perceived" by the body force model and that present in an actual passage with finite-thickness blades. Due to these contrasting effects, it is difficult to predict how the body force model would behave for low blade counts.

3.3   Fan Studied and Numerical Methodology

In this section, we introduce the machine of interest and computational domain, the details of the metrics used to calculate fan performance, and the numerical details for both bladed and body force computations. Recall that for the purposes of this paper, the flow can always be considered incompressible hence no treatment of the energy equation is included.

3.3.1   Fan of Interest and Computational Domain

The fan used in this work is a 7-bladed, shrouded automotive cooling fan filleted at the hub and the tip. The fan blades are radially twisted such that the length of the axial chord decreases from the hub to the tip as shown in Figure 3.1. The fan has a hub-to-tip radius ratio of 0.388, so significant radial shifts in streamlines through the blades are possible. The key design characteristics for the base fan model are given in Table 3.1.

Figure 3.2 shows a schematic meridional view of the computational geometry along with the measurement planes. It is a simple annular duct with the hub and casing

a) Suction side   b) Pressure side   c) Full fan (front view)
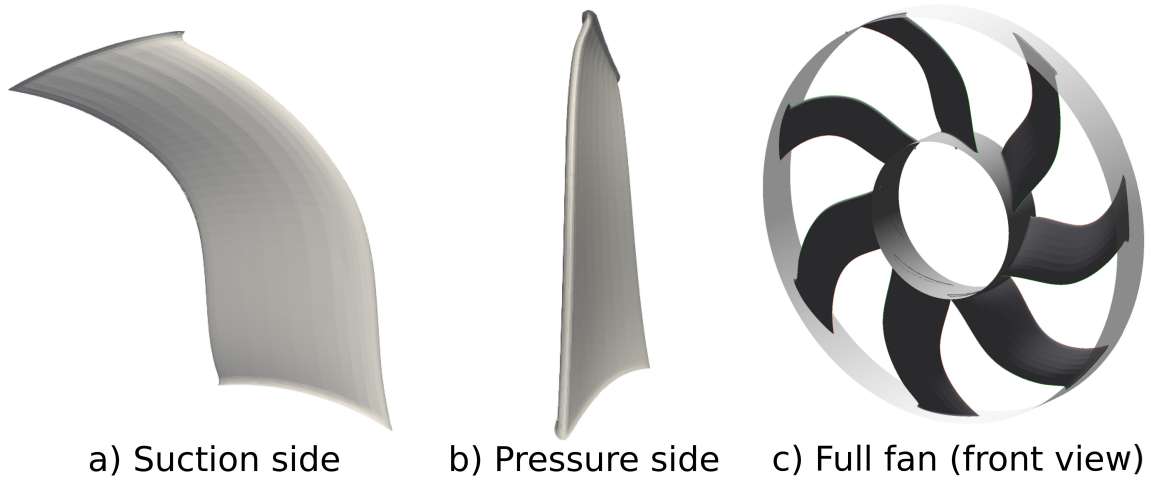
Figure 3.1: Geometry of fan studied
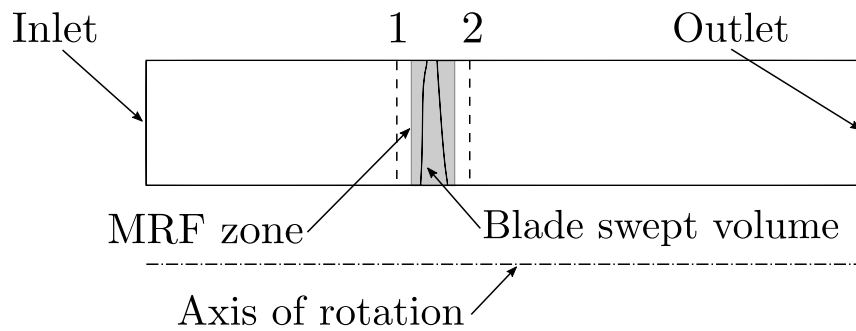
Figure 3.2: Meridional view of the computational geometry

radii equal to those of the fan throughout. The domain extends about two spans upstream and three spans downstream of the blade row. For uniform inflow cases, the body force simulations use a simple 2° wedge. We also employ full-annulus body force computations for circumferentially non-uniform flow cases. On the other hand, a bladed single-passage geometry is employed for the MRF simulations as shown in Figure 3.3. The fan has no tip gap and the hub and casing rings labeled as "rotating walls" in Figure 3.3 rotate with the fan; the rest of the passage walls are stationary. The shaded region in Figure 3.2 represents the "MRF zone" and the blade swept volume defines the "body force region". The details of each computational domain are expanded upon later.

Table 3.1: Design characteristics for the base fan model

Parameter	Value
number of blades B	7
aspect ratio AR	5.56
hub solidity σ_{hub}	0.46
tip solidity σ_{tip}	0.18
r_{hub}/r_{tip}	0.388
design flow coefficient $\phi_{des} = \bar{u}_x^M/U_{\mathrm{mid}}$	0.215
design rotational speed N	2683 rpm

3.3.2 Performance Metrics

The principle metric of interest in this paper is the work coefficient, defined as

$$\Psi = \frac{\bar{h}_{t,2}^{\mathrm{M}} - h_{t,1}}{U_{\mathrm{M}}^2} \tag{3.4}$$

where $\bar{h}_{t,2}^{\mathrm{M}}$ and $h_{t,1}$ are the mass-averaged total enthalpies at the upstream and down-stream measurement locations, respectively, and $U_{\mathrm{M}} = \omega r_{\mathrm{mid}}$ is the midspan blade speed. ω is the angular velocity of the rotor. Since the far-upstream flow is axial, the total enthalpy is simply defined from the Euler turbine equation as $h_t = \omega r u_\theta$ where the tangential velocity u_θ is calculated directly from the velocity field. In assessing grid convergence, the polytropic efficiency is also used and is defined as

$$\eta_{poly} = \frac{\Delta \bar{p}_t^{\mathrm{M}}/\rho}{\Delta \bar{h}_t^{\mathrm{M}}} \tag{3.5}$$

where $\Delta \bar{p}_t^{\mathrm{M}}$ and $\Delta \bar{h}_t^{\mathrm{M}}$ are the mass-averaged values of the total pressure change and the total enthalpy change, respectively, between the upstream and the downstream measurement plane locations.

3.3.3 Boundary Conditions

All the simulations in this work have been performed using the open source CFD software OpenFOAM v6 [26]. Since the flows of interest for automotive under-hood components are incompressible, a velocity inlet is set to force the target volume flow rate and a uniform static pressure outlet is used (there is no radial equilibrium outlet boundary in OpenFOAM v6, which is why the domain exit is relatively further downstream as compared to the inlet). For all rotationally periodic surfaces, `cyclic` (for MRF cases) or `wedge` (for body force cases) type boundary conditions are utilized. Both of these have the effect of ensuring the flow is periodic at these boundaries. For the bladed MRF cases, two types of simulations were run which differ only in the definition of wall boundaries:

1. Case A: All wall boundaries are modeled as free-slip

2. Case B: The blade surface is modeled as a no-slip boundary while the rest of the walls are modeled as free-slip

The application of all free-slip walls in the first case eliminates the effects of secondary flows and viscous endwall losses, thereby isolating the influence of change in blade count on the fan performance. Hence, the results obtained from case A are used to make a direct comparison with those obtained from the inviscid body force model (with all free-slip boundaries). Case B is used mainly for the purpose of assessing grid convergence since viscous loss prediction tends to be more grid-dependent than quantities such as total enthalpy rise. Secondly, the work coefficient values obtained from the two cases are used to assess the significance of the blade profile losses. Lastly, the unsteady blade-resolved RANS simulation presented later in this paper requires the blade surfaces to be defined as no-slip. Hence, the grid convergence study is performed for the case of no-slip as well as slip blade surfaces.

3.3.4   Numerical Approach for MRF Simulations

In the MRF approach, the shaded region around the blade as depicted in Figure 3.2 is treated in a frame of reference that rotates with the fan blades. The resulting flow field obtained is akin to an instantaneous "snapshot" of the true, time-varying flow field. For the cases of uniform inflow, the MRF approach is used to perform simulations for a single-passage bladed model.

Figure 3.3 shows a 3D view of the single-passage computational domain used for the MRF cases. A fully structured hexahedral mesh is generated using Ansys Turbogrid [27] by importing constant-radius blade profile sections, which accurately capture the fillets at both the hub and the casing. The inviscid treatment of wall boundaries does not necessitate the creation of a finer grid near the walls since there are no boundary layers present. However for the purpose of the grid independence study of case B, the near-wall mesh has been refined to resolve any sharp gradients such that a y^+ value of around 30 is attained around the blade wall regions for all grids. There are 53 cells distributed radially across the passage for the medium density grid and a cell growth rate of about 1.1 is employed at all wall boundaries. To assess grid independence, a series of three single-passage grids is created with cell counts of approximately 1, 2, and 4 million while maintaining the y^+ values as well as the cell aspect ratio distribution in the passage. The incompressible, steady-state OpenFOAM solver `simpleFoam` is used to perform the single-passage bladed simulations, and the SST turbulence model is utilized [28].

The impact of grid size on the metrics of interest is assessed by using the approach presented in the book by Roache [29], which is based on the use of Richardson extrapolation to estimate the expected error between different grid levels. This method assumes that the change in results should asymptotically approach zero as the number of grid cells approaches infinity. Figure 3.4 shows the values of the work coefficient for
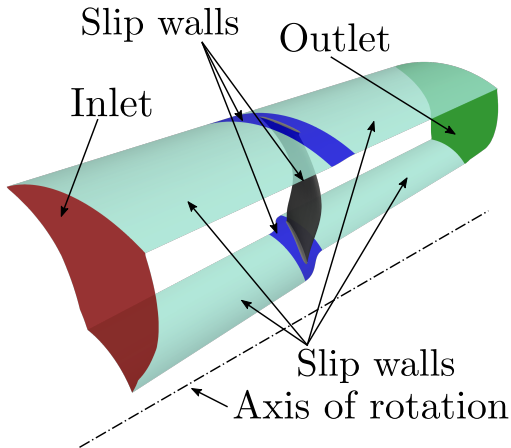
Figure 3.3: 3D view of the single passage domain used for the MRF simulations

cases A and B, as well as the polytropic efficiency for case B. These parameters are shown for the three different grid levels as well as for the limit of infinite grid points as calculated by Richardson extrapolation. For the medium grid level, the Richardson extrapolation predicts a work coefficient of 0.1279 and a polytropic efficiency of 87.6% for case B, and a work coefficient of 0.1303 for case A, with negligible errors for all three quantities. To keep the computational costs as low as possible, the medium grid level with a cell count of approximately 2 million is selected for the rest of the computations.

3.3.5 Numerical Approach for Body Force Simulations

As mentioned earlier, the body force grid for uniform flow cases is a 2° wedge, created using Pointwise v18.3R1 [30]. The cell size distribution is such that there are 40 cells in the axial direction and 100 cells in the radial direction inside the blade swept volume for the medium density grid. There is a single cell in the circumferential direction. The boundary conditions are identical to those used for the MRF simulations. The free-slip treatment of the passage walls eliminates the need for any wall boundary layers. The mesh near the walls is still made fine enough to capture the gradients in the flow quantities. A cell growth rate of 1.1 is employed at all wall boundaries.
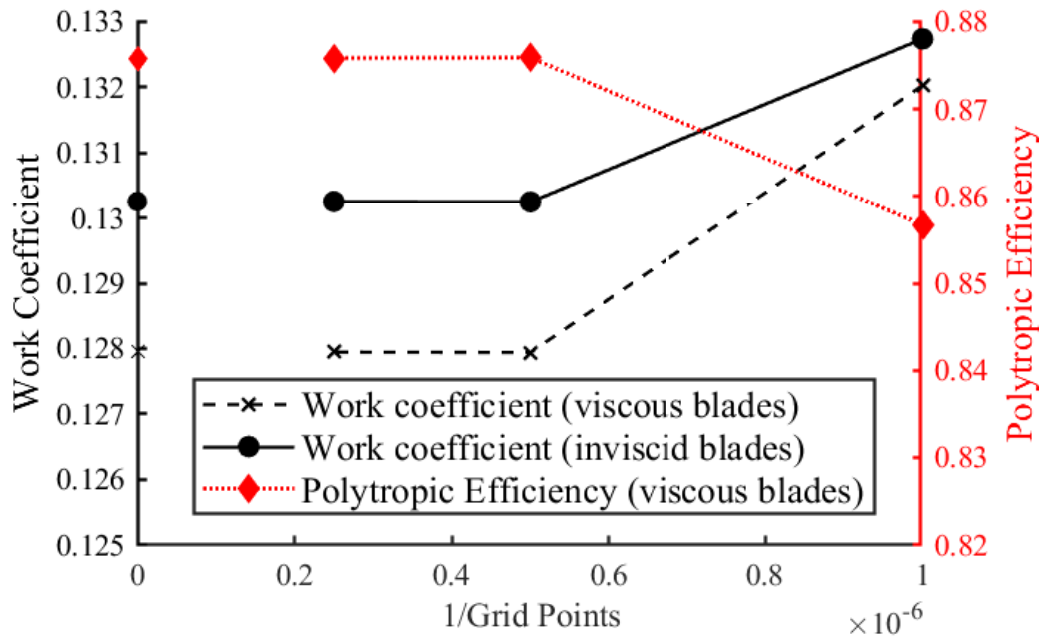
Figure 3.4: Work coefficient and polytropic efficiency as a function of grid points for the MRF simulations

As depicted in Figure 3.2, the swept volume of the blade defines the body force region inside which the momentum equations are solved by taking into account the volumetric source terms. The magnitude and direction of the body force exerted on the flow is frame-independent, hence there is no need for any kind of interfaces before or after the body force region. OpenFOAM offers the capability of adding source terms to the solver equations via custom user-generated code, referred to by the shorthand `fvOptions`. For the purpose of implementing Hall's body force model in the most efficient way, a modified version of the `simpleFoam` solver is employed to easily define the blade camber surface unit normals as a separate vector field. The interpolation functions from the Computational Geometry Algorithms Library (CGAL) are utilized to generate the camber field for every grid [31]. The volumetric source terms are then calculated within the region defined by the swept volume of the blades for each iteration and are added to the momentum equations.

A series of three grids were created to assess the impact of grid size on the work coefficient.The successive grids were refined in the axial and radial direction by a factor of 2. Again Roache's approach is used. Figure 3.5 shows the values of work coefficient obtained for the body force calculations for the three different grid levels as well as for the limit of infinite grid points as calculated by Richardson extrapolation. For the medium grid level, we obtain a work coefficient of 0.1052, and based on Richardson extrapolation the associated possible error is $\pm$ 0.0002. This is a small error, so to lower computational costs, the medium grid level with a cell count of 8.72×10^4 is employed for the rest of the uniform flow body force computations. The same grid, revolved around the fan axis to yield 180 cells in the circumferential direction around the full wheel, is used for non-uniform flow.
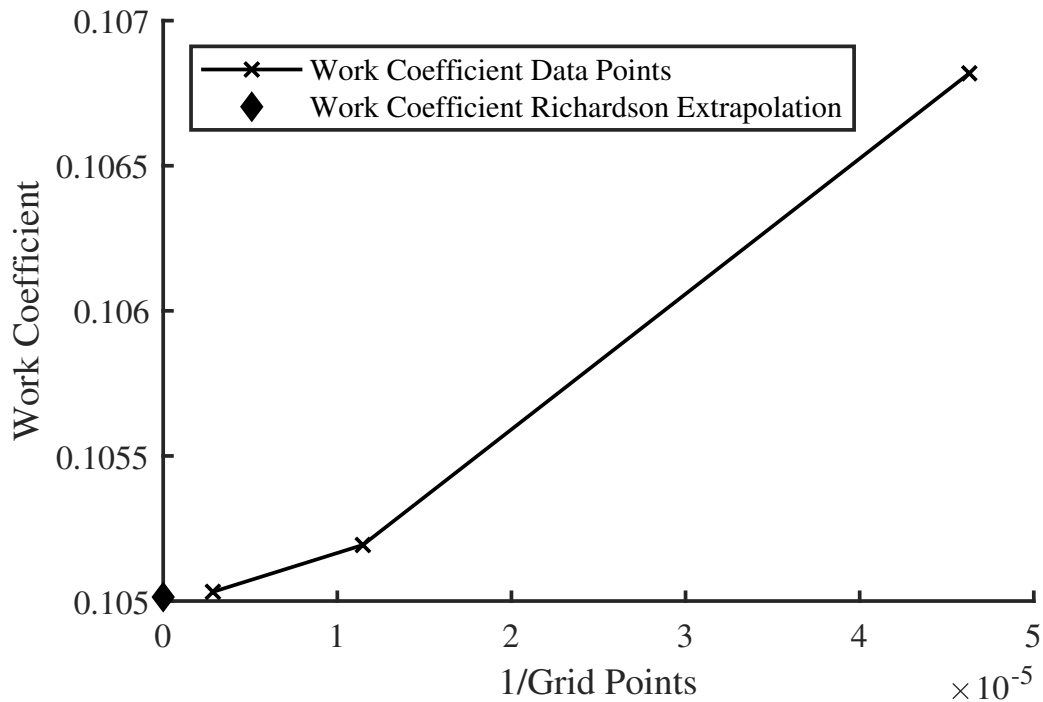
Figure 3.5: Work coefficient as a function of grid points for body force simulations at the design flow coefficient

3.4   Results and Discussion

3.4.1   Assessment of MRF Model Accuracy against Experimental Data

Experimental test data available from the fan manufacturer only includes the static pressure rise for a range of flow rates at the design rotational speed. We were unable to obtain many details of the test rig geometry, so it was not possible to computationally model the fan within the test rig. It is known that the upstream pressure measurement in the rig was from a plenum, so the measurement more accurately corresponds to a total-to-static measurement. Thus the best option is to compare total-to-static pressure rise coefficients from the experimental data and the MRF computations. The total-to-static pressure coefficient is defined as:

$$\Psi_{\text{ts}} = \frac{\bar{p}_2^{\text{M}} - p_{\text{t},1}}{\rho U_{\text{M}}^2} \tag{3.6}$$

where $\bar{p}_2^{M}$ and $p_{t,1}$ are the mass-averaged values of static pressure at plane 2 and total pressure at plane 1, respectively (for the experiments, the static pressure rise is used for the numerator). Some offset is expected because of the differences in geometry and in the quantities measured. However, the slopes of the fan characteristic should be similar if the numerical model is performing as intended, so we assess the degree to which the experimental and numerical characteristic slopes are similar. The characteristics are shown in Figure 3.6. The MRF predictions are for case A since the speedline was obtained for later comparison with the body force model and the pressure rise is not strongly affected by the lack of shear stress on the blade surface (as later shown in Figure 3.7). The MRF model predicts higher pressure rise than what was measured experimentally. This is due to the fact that the case A results do not involve any viscous losses due to the blade or the passage walls, and possibly due to larger flow area at the downstream measurement location in the experiments. It
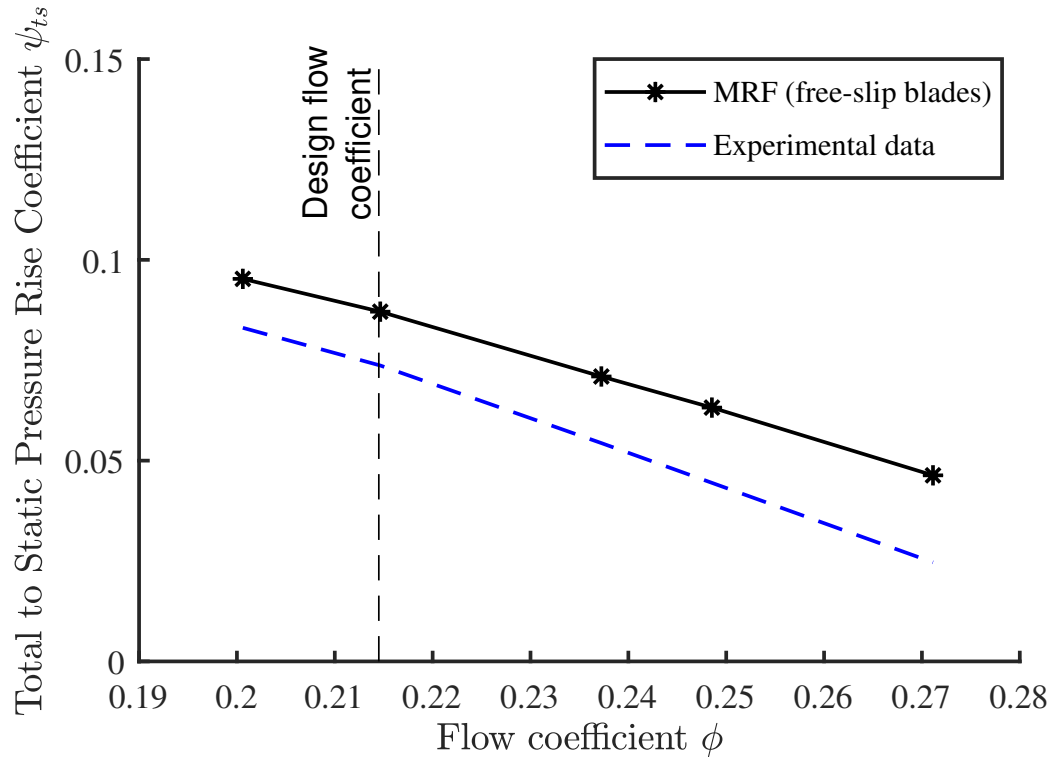
Figure 3.6: Fan total-to-static pressure rise coefficient as a function of flow coefficient

is clear that the MRF approach accurately captures the fan characteristic slope, and thus is a good metric against which to assess the body force model.

3.4.2 Body Force Model Accuracy Compared to MRF Predictions for a Range of Flow Coefficients

In this section we compare uniform-inflow body force predictions of rotor total enthalpy rise to those produced by the MRF approach. It is also important to gain insight into the flow mechanisms which drive the inaccuracies in the model predictions for a fan blade row designed, as is our fan of interest, for the low total enthalpy rise and low flow coefficient regime. This regime is common for automotive cooling fans.

First we examine the fan total enthalpy rise characteristic at the design rotational speed, shown in Figure 3.7. Both bladed (MRF) and body force results are shown.

While the body force model successfully captures the general trend of the variation of the work coefficient with the flow coefficient, the work coefficient is under-predicted compared to the results obtained from the free-slip wall single passage computations. The disparity increases with flow coefficient. At the design flow coefficient of 0.214, the observed behavior is the opposite to that observed in other studies which have used the original or modified versions of Hall's body force model formulation [15, 24]. At the design flow coefficient, the body force predicts the work coefficient to be 0.108 while the MRF approach (with inviscid walls) yields 0.130 (error of -0.022). Also shown in the figure is the work coefficient for the bladed computation with no-slip walls (case B), and it is clear that removing wall shear stresses has only a small impact on work coefficient. It is interesting to note that in Hall's original work [15], the model was shown to predict the work coefficient with an error magnitude of ± 0.02 at the design operating point of a low-speed fan stage, which is the same range of error observed in the present study. Thus it appears that this magnitude of error is consistent in absolute magnitude. Since the automotive fan used in this study is a highly staggered design, made for low flow coefficients and a very low design work coefficient, the error is more significant compared to fans previously studied with this model.

To begin to identify why the work coefficient is under-predicted with the body force approach, we examine chordwisetotal enthalpy rise distributions across the span at the design flow coefficient. These are depicted in Figure 3.8. The body force model always under-predicts the total enthalpy rise and the inaccuracy arises from the low or even negative total enthalpy change by the body forces in the leading 25% of the chord. The lag in total enthalpy rise (flow turning) is a well-known consequence of Hall's approach, especially at design where incidence is near zero. This is because the force is proportional to deviation, so that if the incoming relative flow is well-aligned to the camber surface, initially the body forces are nearly zero. Only further down the chord
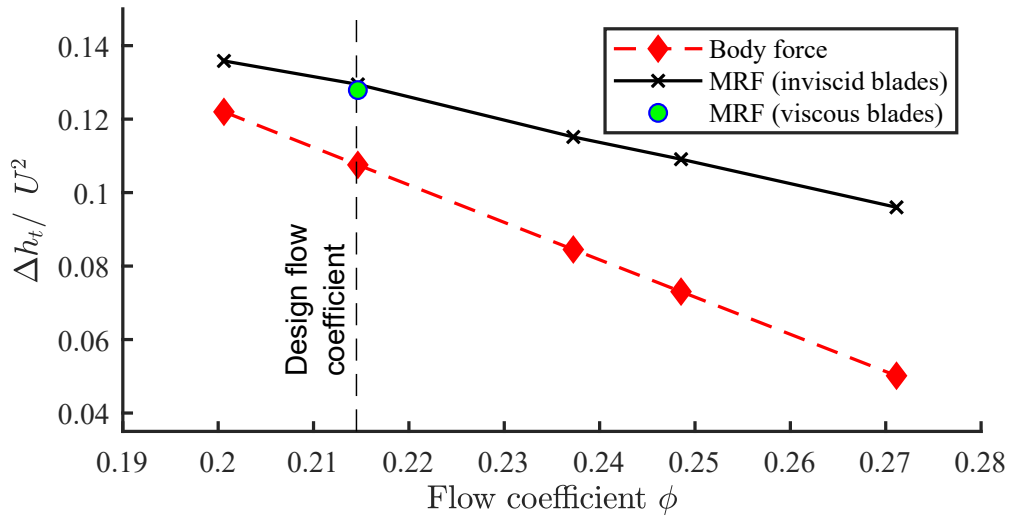
Figure 3.7: Fan work coefficient as a function of the flow coefficient for the 7-bladed fan

when the flow hasn't turned enough does the local deviation rise and the forces act to turn the flow back towards the camber surface. However, the low blade count for the fan here reduces the magnitude of the body force compared to other fans simulated using this approach. This means that flow deviation reduces relatively slowly and the tangential velocity is still not "caught up" by the trailing edge, compared to the bladed case. Additionally, the negative values of the work coefficient near the start of the blade chord in the inner span indicate negative incidence, which exacerbates the catch-up problem. As the axial chord length shortens from the hub to the tip, the distance available for the body force to catch up with the flow turning in the real blade row also decreases. Hence, the difference between the total enthalpy rise at the end of the body force region tends to be higher as one gets closer to the tip.

To try to understand why the agreement between bladed and body force computations worsens at high flow coefficients, we examine the spanwise distribution of local flow coefficient (axial velocity normalized by midspan blade speed) in Figure 3.9. Results are shown for both the design flow coefficient and the highest flow coefficient examined, for both bladed (circumferentially averaged) and body force
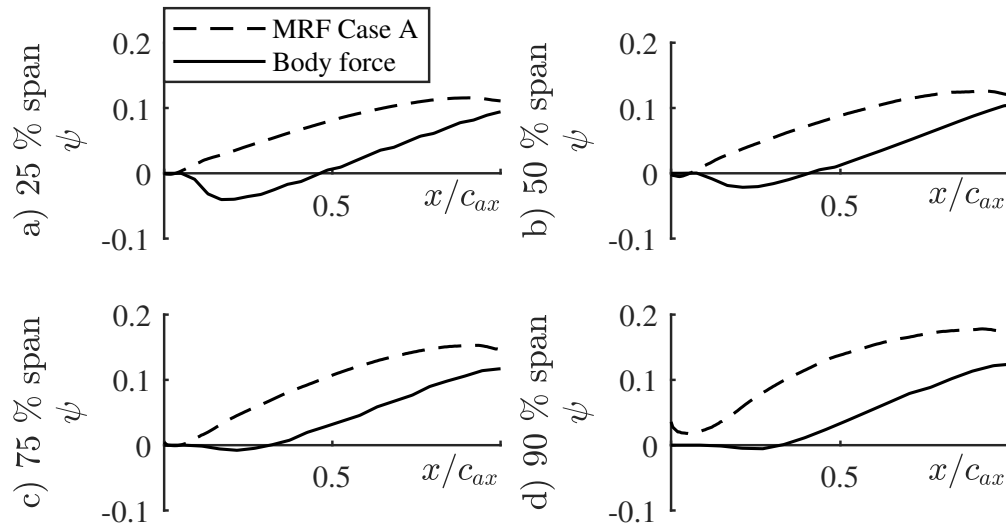
Figure 3.8: Work coefficient versus meridional distance through the fan at different spans, and $\phi = 0.214$

computations. In the bladed computations, there is a radially-outward shift of the streamlines through the rotor which causes a small separation bubble to form right after the trailing edge of the fan blade near the hub. The size of this separation bubble shrinks as the flow coefficient increases and the blades are unloaded. This can be seen in Figure 3.9 as higher local flow coefficient values in the inner 10% span at $\phi = 0.271$ than for $\phi = 0.214$ for the bladed computations. In the smeared-out version of the flow field created by the body force model, there is no separation bubble formed but just a region of slower flow near the hub; however its circumferential uniformity (as opposed to the local separation regions in the bladed case) results in a shift of mass flow towards the tip, with the effect more dramatic at $\phi = 0.214$ than at $\phi = 0.271$. The reduced loading at high flow coefficient reduces the radial flow redistribution for the body force model and increases agreement in the spanwise distribution relative to the bladed case.
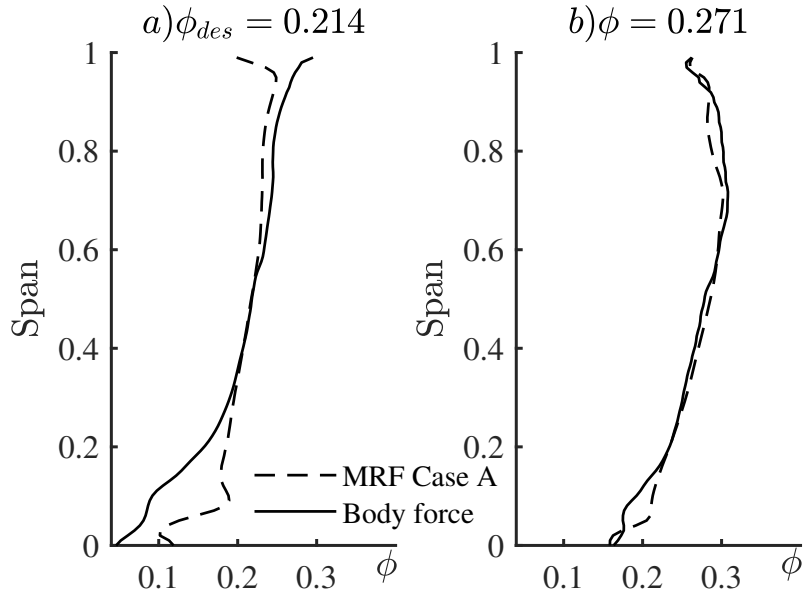
Figure 3.9: Radial traverse of flow coefficient downstream of the fan at (a) $\phi = 0.214$ and (b) $\phi = 0.271$

The differences in radial flow distribution yield changes in the spanwise profiles of total enthalpy rise at the trailing edge; these are shown in Figure 3.10. At the design flow coefficient (0.214), the increased flow in the outer 40% span for the body force model results in significantly lower total enthalpy rise, driving the under-prediction of the mass-averaged work coefficient. At the high flow coefficient (0.271), the flow distributions along the span from Figure 3.9 are in excellent agreement, and there is a consistent spanwise under-prediction of total enthalpy rise due to the lag effect of the body force model discussed earlier. Thus, consideration of Figures 3.9 and 3.10 reveals that the better agreement in overall work coefficient at design flow coefficient compared to high flow is actually the result of **reduced** agreement of flow distribution. At high flow the distribution agreement is good which yields under-prediction of loading across the full span. Therefore the main issue with the body force model in this case is that, when the local flow coefficients are correct, total enthalpy rise is significantly under-predicted.
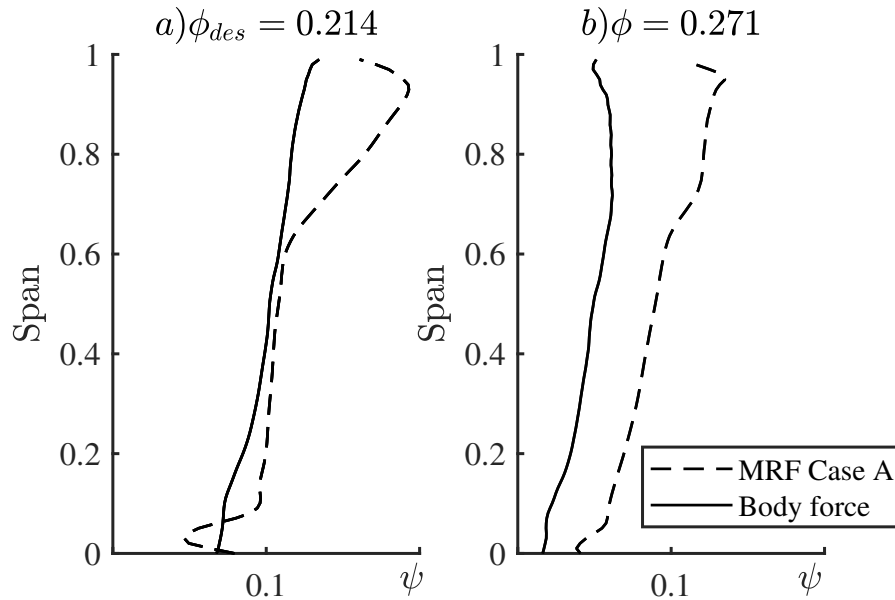
Figure 3.10: Radial traverse of work coefficient downstream of the fan at (a) $\phi = 0.214$ and (b) $\phi = 0.271$

3.4.3 Effect of Blade Count on Body Force Model Accuracy

The single-passage grid created for the 7-bladed fan model represents one-seventh part of the full-annulus, hence different grids have to be created for fans with different blade counts. This was achieved in Turbogrid [27] by simply changing the extent of the pitch of the grid while maintaining all other parameters including the cell size and the boundary layer refinement constant. The blade count is varied from 5 to 22 for both the bladed and the body force simulations, and the cases are run with uniform inflow at the design flow coefficient.

Figure 3.11 depicts the variation of the work coefficient for fans with different blade counts at the design flow coefficient. While the decrease in deviation (and thus increase in flow turning and work coefficient) associated with increasing the blade count is evident for both modeling approaches, the body force model again always under-predicts the total enthalpy rise compared to the bladed computations. The amount of under-prediction increases as the number of blades increases from nearly
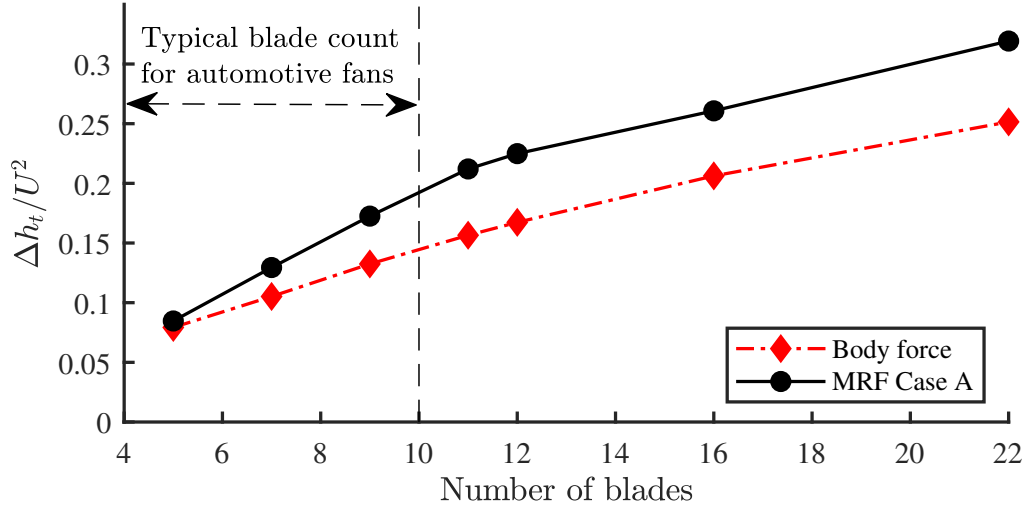
Figure 3.11: Fan work coefficient as a function of the number of blades at the design operating point

zero at 5 blades to approximately 0.06 at 11 blades, and then remains approximately constant. Though on the scale of Figure 3.11 the error at $B = 7$ blades appears small, this is the same data shown in Figure 3.7 at $\phi = 0.214$ and so represents a significant under-prediction by the body force model.

There are two phenomena that can be observed in Figure 3.11 which require explanation: the linear increase in under-prediction for rising blade counts up to ~ 12 blades, and the change in slope for the bladed computations at higher blade counts than this. It is therefore useful to consider the inherent differences between the flow turning behavior caused by the physical blade row as compared to that caused by the body force model. To facilitate this comparison, the difference in relative flow angle between body force and bladed computations is tracked along the axial chord. The difference between the local relative flow angles is defined as:

$$\Delta\beta = \overline{\beta}_{\mathrm{BF}}^{\,\theta} - \overline{\beta}_{\mathrm{SP}}^{\,\theta} \tag{3.7}$$

where $\overline{\beta}_{\mathrm{BF}}^{\,\theta}$ and $\overline{\beta}_{\mathrm{SP}}^{\,\theta}$ are the circumferentially averaged values of the relative flow

angle at a given fraction of the span for the body force and bladed calculations, respectively. Since we are dealing with a fan, higher relative flow angles imply less turning/total enthalpy rise so positive values of $\Delta\beta$ mean the body force model is turning the flow less than in the computations with blades. Since the outer span contains much of the mass flow, we focus on the $\Delta\beta$ distributions at 90% span. In addition, the streamlines at 90% span experience relatively little radius changes from leading to trailing edge, facilitating tracking $\Delta\beta$. In Figure 3.12 we plot $\Delta\beta$ along the axial chord for differing blade counts. Red is used to highlight the cases firmly in the linear region while black is used for higher blade counts. The impact of upstream influence (which occurs for the bladed cases, but not for the body force approach in uniform inflow) is apparent in the leading edge values of $\Delta\beta$: the flow aligns more closely to the blade camber surface at the leading edge for the bladed cases, and this effect is magnified at higher blade counts, though the incidence mismatch begins to saturate as the blade count gets high. In general $\Delta\beta$ decreases along the chord as the body force model again tries to "catch up" to the flow direction imposed by the blades. At 90% span, $\Delta\beta$ is always positive, meaning there is a consistent under-prediction of flow turning.

The total enthalpy rise is affected not only by the relative flow angle but also the axial velocity. To examine how the work build-up leads to the overall results seen in Figure 3.11, we consider the difference in the local work coefficient $\Delta\psi$ between the single-passage (SP) bladed and the body force (BF) simulations, calculated as

$$\Delta\psi = \overline{\psi}_{\mathrm{SP}}^{\theta} - \overline{\psi}_{\mathrm{BF}} \tag{3.8}$$

Positive values indicate that the blades do more work on the flow than does the body force model. This is plotted against axial chord at 90% span for varying blade counts in Figure 3.13. The differences peak near midchord and the overall curves become
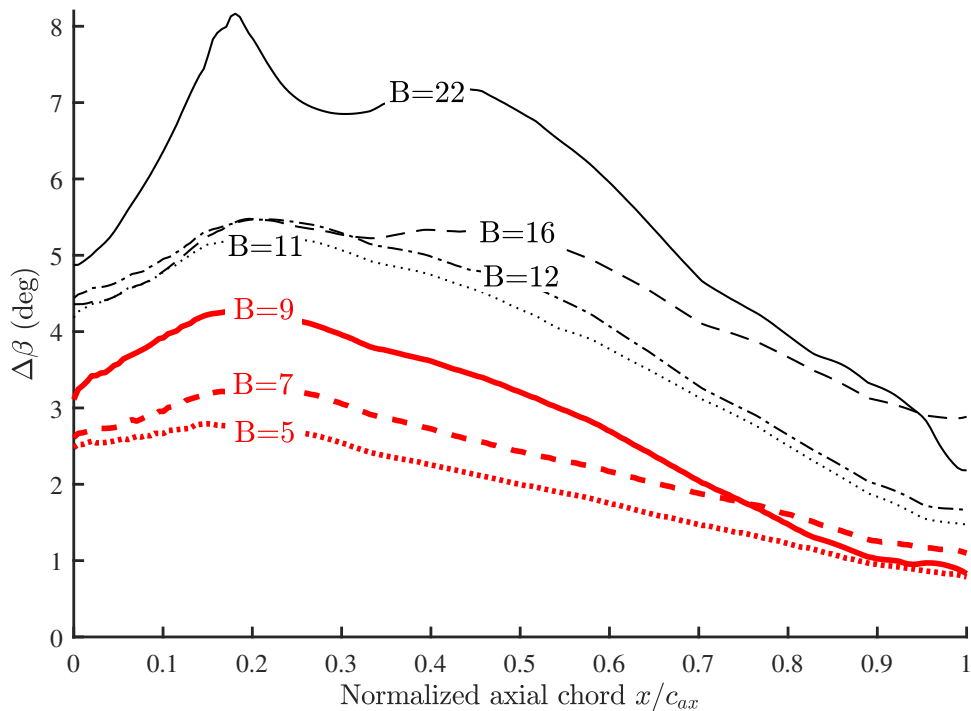
Figure 3.12: Variation of difference in relative flow angle between the MRF and the body force simulations through the passage at 90% span for the design operating point

insensitive to blade count for $B > 10$. This shows that the body force model work coefficient falls behind in the front half of the blade row and then catches up towards the trailing edge. The significant negative slopes of all the $\Delta\psi$ curves at the trailing edge suggest that if the blades were longer (i.e. higher solidity), the under-prediction of work by the body force model would be alleviated. Referring back to Table 3.1, it can be seen that especially at the tip the solidity is 2-3X lower than those normally seen in axial fans for aircraft engines where Hall body force model has previously been applied. The low solidity affords less opportunity for the body force model flow turning to "catch up" to that in the bladed case, which fundamentally drives the under-prediction of total enthalpy rise.

Another factor that drives the increase in accuracy of the model as the number of blades reduces is related to the effect of the metal blockage created by the finite
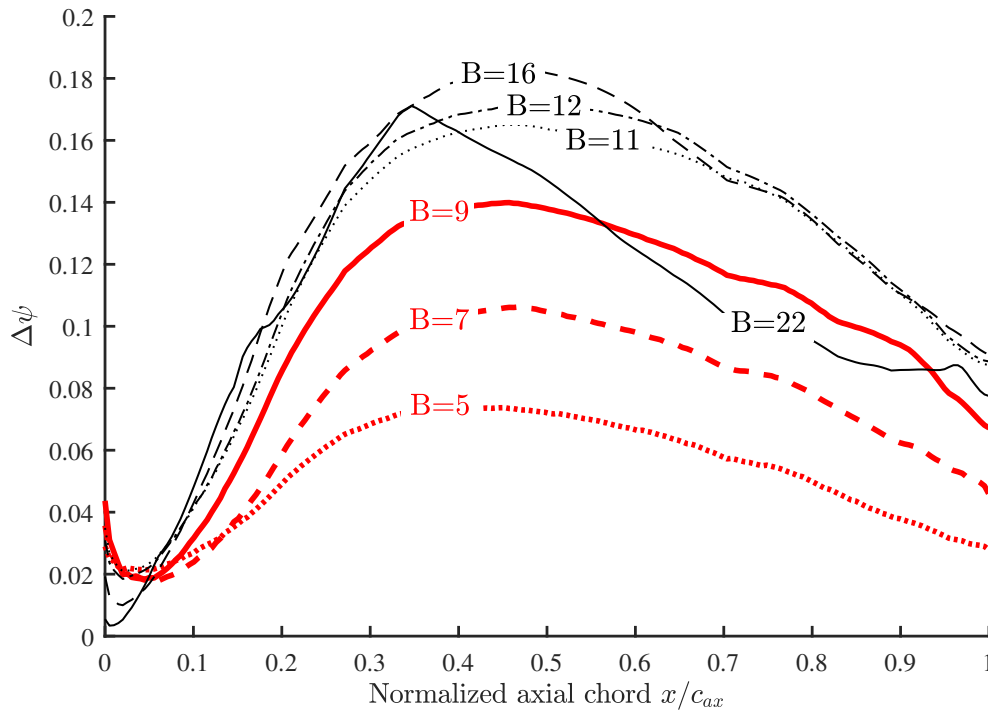
Figure 3.13: Chordwise variation of difference in total enthalpy rise between the MRF and the body force simulations through the passage at 90% span for the design operating point

thickness of the blades. Figure 3.14 schematically illustrates that for a blade design with a given design work coefficient, the choice of flow coefficient dictates the stagger angle. The lower the flow coefficient, the higher the blade stagger and lower the axial width of the passage for a given blade thickness. The blade metal blockage factor b introduced in Eq. 3.3 scales linearly with the width of the passage and the number of the blades. As the number of blades decreases, the circumferentially-averaged relative velocity field in the body force computations becomes a better estimate of that in the bladed case as the metal blockage factor decreases. This leads to improved accuracy in the prediction of total enthalpy rise. For highly staggered blades such as those studied in this paper, the effect of the metal blockage factor assumes greater significance at high blade counts. This contributes to the divergence of the results for the body force and bladed computations as the number of blades increases.
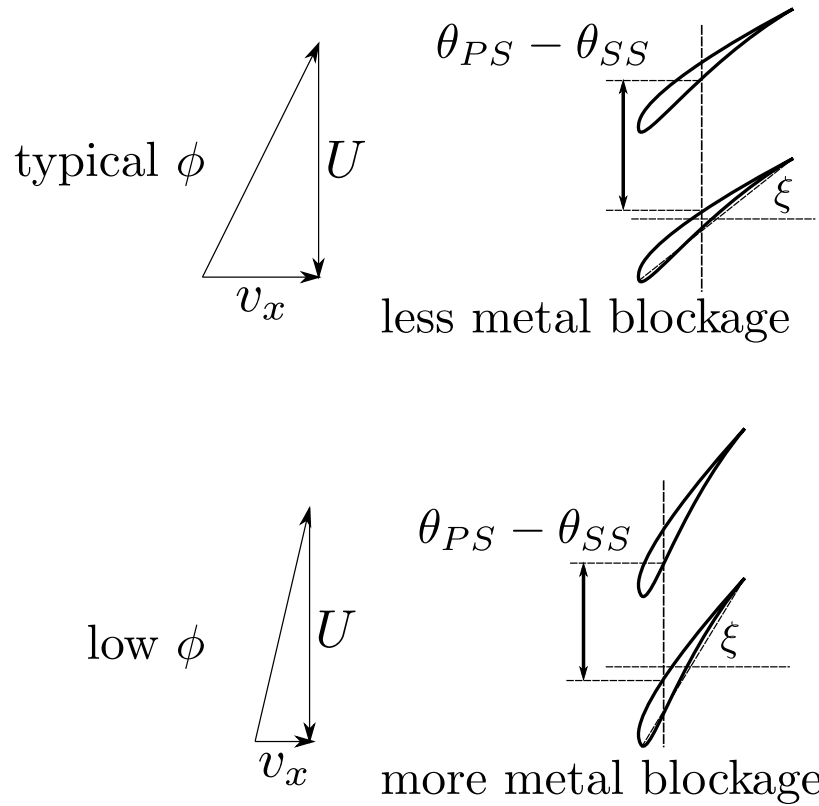
Figure 3.14: Impact of flow coefficient and stagger angle on blade metal blockage for constant blade thickness and pitch

The leveling off of the difference between the work coefficients obtained with the two approaches can be explained by the presence of a hub separation that appears at blade counts above 10. This can be seen in Figure 3.15, in which we plot the spanwise profiles of flow coefficient and work coefficient for the 12-bladed case. The negative flow coefficients near the hub indicate the presence of a region of separated flow. This constrains the radial streamline shifts, yielding better overall agreement in the flow distributions between bladed and body force computations. The result is a more consistent under-prediction of total enthalpy rise across the majority of the span. The lower total enthalpy rise by the body force model is again caused by the low solidity (even with higher blade counts!) and stops being a strong function of blade count itself.
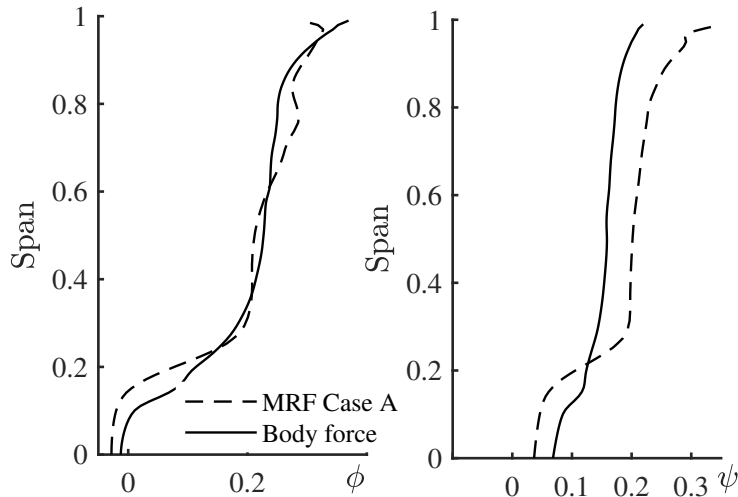
Figure 3.15: Flow coefficient and work coefficient versus span at plane 2 for $B = 12$ blades, $\phi = 0.214$

3.4.4 Effect of Blade Count and Distortion Scale-to-Pitch Ratio on Fan Interaction with Non-Uniform Inflow

The current body force approach has been widely used to study distortion transfer characteristics in turbomachines and has been shown to capture distortion transfer accurately for flow non-uniformities which have a much larger characteristic length scale than the rotor blade pitch and which have a local rotor reduced frequency significantly less than one [15]. The local reduced frequency is

$$g_{\mathrm{red}} = \frac{c_{\mathrm{x}}/u_{\mathrm{x}}}{2\pi/\omega} \tag{3.9}$$

where c_{x} is the local axial chord and u_{x} is the local axial velocity. For our machine of interest, the values of g_{red} ($\sim$ 0.13-0.2) are towards the higher end of the spectrum of the typical values (< 0.1) that have been considered in previous studies[15, 16]. Therefore, it is of interest to see how Hall's body force model applied to the fan studied here predicts distortion transfer for varying blade counts. Since in under-hood

applications the flow is typically highly non-uniform, this sort of prediction is important to determine the suitability of using Hall's approach for modeling automotive cooling fans in-situ.

In this section, two types of non-uniform inflow cases are studied. First, these are described, and then results are presented.

Case 1: Total Pressure Inflow Distortion

The first case is that of a vertically stratified inlet distortion identical to one of the distortions studied by Defoe et al. [16]. The distortion is characterized by two parameters: the distortion intensity $v_{x,max}/v_{x,min}$ and the distortion immersion $d/2R_o$, where d is the height of the duct of outer radius R_o occupied by varying inlet velocity (and thus total pressure). We examine a distortion with $v_{x,max}/v_{x,min} = 0.5$ and $d/2R_o = 0.5$. The resulting total pressure profile at the computational domain inlet for a flow rate equal to the design flow for our fan is illustrated in Figure 3.16.
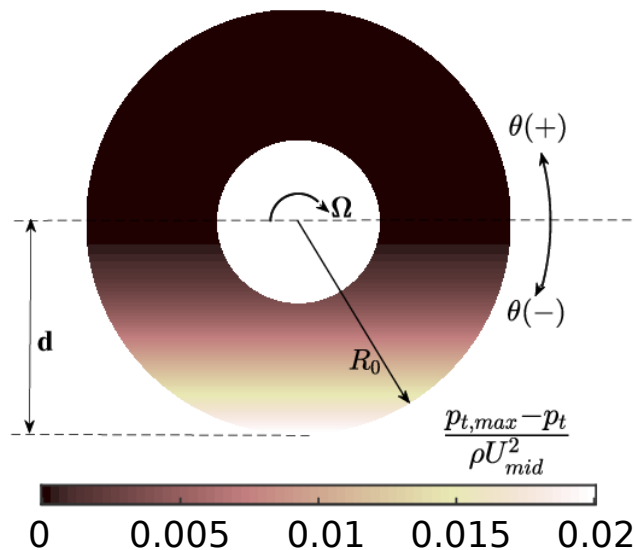
Figure 3.16: Inflow distortion case 1: A vertically stratified total pressure distortion at the inlet

The grids used for these computations include the full annulus. For body force computations, the grid is generated by revolving the wedge geometry used for the uniform-inflow body force computations around the axis of rotation. To assess whether the body force model is accurately responding to the total pressure distortion, one of the cases is compared against higher-fidelity blade-resolved unsteady RANS simulation. For this purpose, a full-wheel grid is generated by appropriate instancing of the single passage bladed domain used for the uniform-inflow calculations (medium grid level). In the unsteady computation, there are 2236 time steps per rotor revolution.

At the inlet, the velocity profile is specified to yield the desired total pressure variation and target flow rate. The static pressure is set to zero at the domain outlet. Using the dynamic mesh capabilities of OpenFOAM[26], the "MRF zone" in Figure 3.2 is replaced by a dynamic mesh region (`cellZone`) which rotates with the rotational speed of the fan for the unsteady computation. In that computation, two sliding mesh interfaces are defined at the boundaries of this `cellZone` to couple the adjacent stationary and rotating mesh regions. Flow field information is passed across the sliding interfaces using the `cyclicAMI` boundary condition. All the wall boundaries are defined as slip (zero shear stress), except the blade surfaces in the unsteady computation. Due to the limitations of the available boundary conditions in OpenFOAM, it was not possible to define inviscid blade walls inside a dynamic mesh region. Since the inclusion of shear stresses is found to have a negligible impact on the performance of the fan as discussed earlier, the comparison with the blade-resolved case with no-slip blade surfaces is sufficient to ascertain the accuracy of the body force computations. In particular, the upstream influence of the blade row is not significantly affected by viscous effects. The incompressible, transient OpenFOAM solver `pimpleFoam` is utilized for performing these unsteady computations. The unsteady simulation was allowed to run for about ten rotor revolutions (about three times the passage through-flow time) until the solution reached a periodic steady state.

Case 2: Downstream Blockage

For the second case, we consider the same geometry upstream but a half-blocked annulus downstream of the fan which causes static pressure distortion at the fan inlet. For this case we consider body force computations only. This kind of geometry is representative of the blockage caused by an engine block placed just downstream of the fan in a real automotive under-hood setting. Figure 3.17 shows the computational geometry used for this case, along with the boundary conditions. The blockage is placed one blade span downstream of the end of the body force region. All the walls, except the ones bordering the blockage, have been defined as free-slip. A uniform velocity is prescribed at the inlet to attain the design flow rate and the static pressure is specified at the outlet. The grid used for this computation is similar to the one employed for full-wheel body force computations, except the blockage region has been removed. The mesh in the vicinity of the no-slip walls has been refined to achieve a y^+ value of around 30.
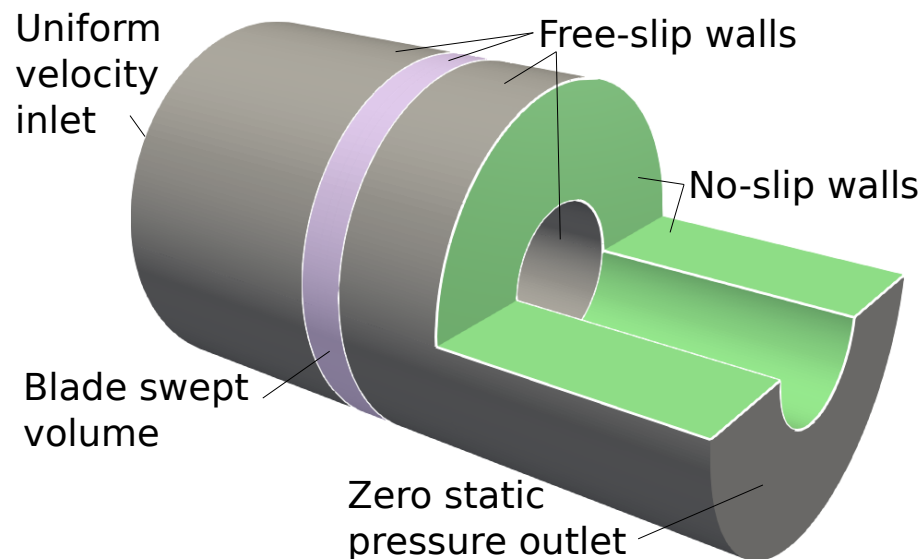
Figure 3.17: Inflow distortion case 2: Downstream blockage

Body Force Assessment in Non-Uniform Flow

For case 1, we use a 5-bladed fan (same blade shape as considered in the rest of the paper) to determine the accuracy with which the body force model can predict upstream influence and distortion transfer in non-uniform flow. In Figures 3.18 and 3.19, the variations in absolute swirl angle from the circumferential means $\Delta\alpha$ are shown for 25%, 50%, and 75% span for the 5-bladed case for both unsteady bladed and body force computations upstream and downstream of the rotor, respectively.

Figure 3.18: Circumferential variation of the absolute swirl angles at different span fractions upstream of the blade row for the case of total pressure distortion

For the unsteady blade-resolved simulation, the flow angles have been calculated from the mean velocity field by time-averaging the instantaneous velocity fields over one rotor revolution. At 25% and 50% span, the agreement between the two approaches is excellent (differences generally $\leq 1°$). At 75% span, the first quarter of the annulus has some short length scale perturbations which are not apparent in the body force results. This is likely a numerical effect rather than a physical one: the

mesh is finer in the outer span to resolve the shroud fillet, and the relative velocities increase with span. This yields higher Courant numbers in the outer span. While a smaller time step would solve this issue, the results are adequate to indicate that even with only 5 blades the body force model is able to capture rotor upstream influence and distortion transfer. This is a comparable level of accuracy for upstream influence and overall better accuracy for distortion transfer than in Hall et al.'s comparison to experimental data for a low-speed aircraft engine fan [15].

Figure 3.19: Circumferential variation of the absolute swirl angles at different span fractions downstream of the blade row for the case of total pressure distortion

Impact of Blade Count on Upstream Influence and Distortion Transfer

We present body force results for both non-uniform inflow cases to investigate how changing blade counts (and thus the ratio of distortion length scale to pitch) alters the fan-distortion interaction. Blade counts of 2, 5 and 9 have been chosen to study the body force model response to inflow distortions. We include a blade count high enough that we would expect good agreement with detailed bladed computations (9

blades), and then examine changes in distortion response for lower blade counts.

Since from the last section it is clear that changing the blade count has a significant impact on the work coefficient predicted by the body force model, comparing inlet distortion response for differing blade counts requires alteration of the rotational speed to yield a consistent total enthalpy rise at the design flow rate in uniform inflow. We consider only blade counts <10 to avoid the hub separations seen at high blade counts as discussed in the previous section. For the 5-bladed fan we maintain the design rotational speed of 2683 rpm. This yields a mass-averaged work coefficient at the design flow rate of 0.0797. To obtain the same total enthalpy rise with 2 and 9 blades requires rotational speeds of 3389 rpm and 2387 rpm, respectively. While this ensures the same overall performance in uniform inflow, local excursions in axial velocity from the mean in the non-uniform inflow case require consideration of the characteristics of the fans with the three blade counts at their respective rotational speeds. These are shown in Figure 3.20. As expected the characteristic slopes are steeper with a larger number of blades, but the differences in total enthalpy rise are not large for small excursions in local flow conditions from the design value.
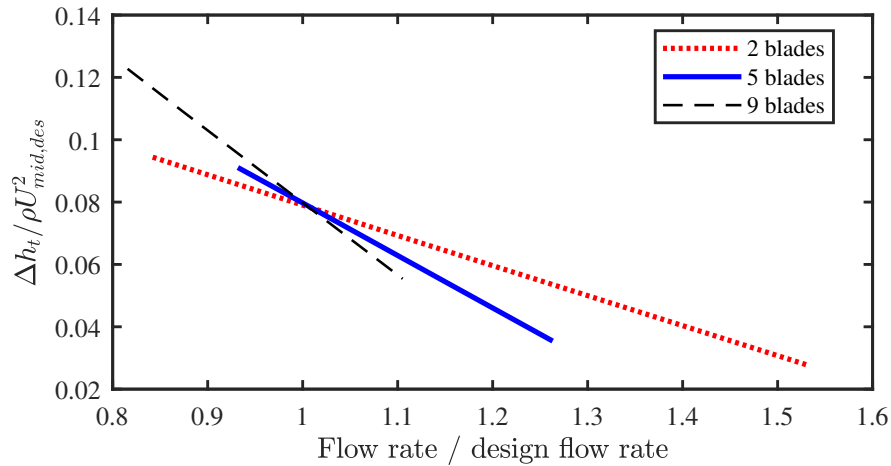
Figure 3.20: Fan work coefficient normalized by design rotational speed versus normalized flow rate. Body force results, rotational speed varying by number of blades.

First we consider the upstream influence of the fan on flow redistribution for case 1, total pressure distortion at the inlet. This yields non-uniform absolute swirl angles around the annulus and across the span. Returning to Figure 3.18, the variations in absolute swirl angle from the circumferential means are shown at 25%, 50%, and 75% span for the three blade counts considered for the body force computations. It is striking that the upstream swirl angle variations are nearly identical for the 5- and 9-bladed fans, while despite the flatter characteristic slope for the 2-bladed fan, the swirl angle variations yield (slightly) more uniform flow. This may represent a limitation of the body force model for extremely low blade counts. However, in the typical blade count range for automotive fans, we see that there is no impact of nearly doubling the pitch to distortion wavelength ratio (going from 9 to 5 blades). In Figure 3.19 the variations in absolute swirl angle downstream of the rotor are shown for case 1 for differing blade counts, and it is clear that the distortion transfer through the rotor is nearly identical for all blade counts considered, and that there is very little attenuation of the inlet distortion across the rotor. This is due to the very low work coefficient values at the operating points of interest.

Finally, we consider case 2, downstream blockage. The flow distribution upstream of the fan is presented in Figures 3.21 and 3.22, which depict the variations in absolute swirl and radial flow angles, respectively, from the circumferential means for different span fractions. The trends shows similar behaviour to that of the total pressure distortion case. The 5- and 9-bladed fans yield nearly identical upstream flow variations in both the absolute swirl and radial flow angles, however the 2-bladed fan exerts a significantly different upstream influence on the flow redistribution. Figures 3.23 and 3.24 show the circumferential variations of the swirl and radial flow angles, respectively, just downstream of the fan for the three blade counts at different span fractions. Again, the 5- and 9-bladed fans respond identically, but the 2-bladed fan shows significant excursions from that behavior, especially in non-blocked out region.
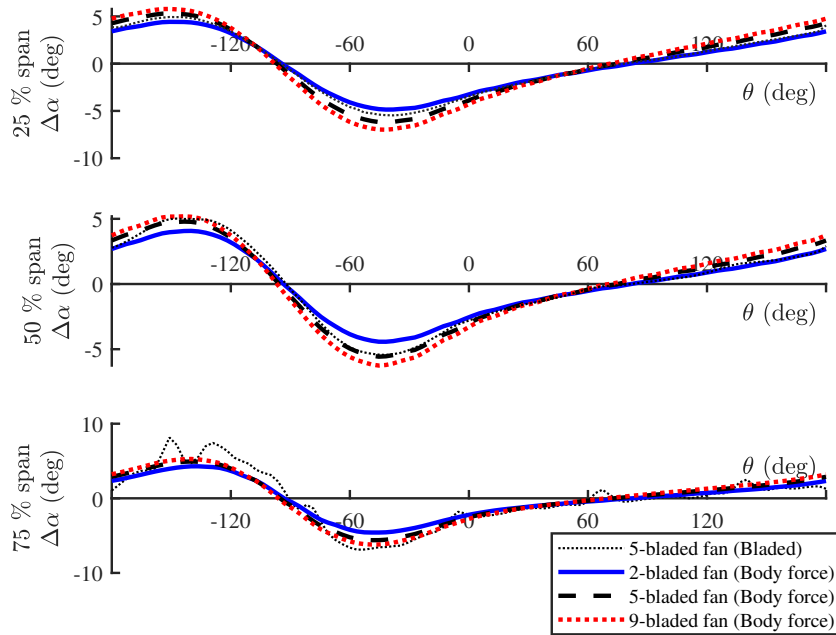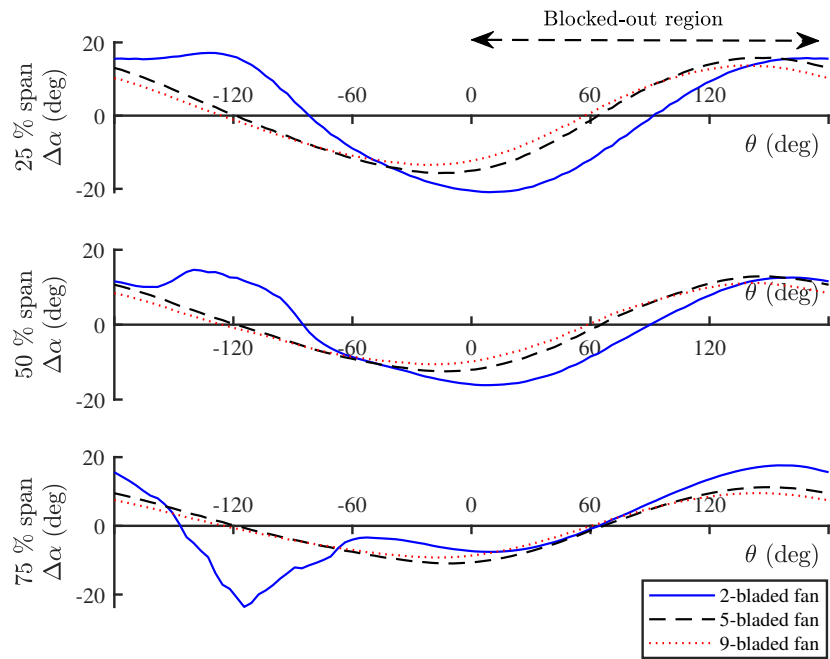
Figure 3.21: Circumferential variation of the absolute swirl angles at different span fractions upstream of the blade row for the case of downstream blockage
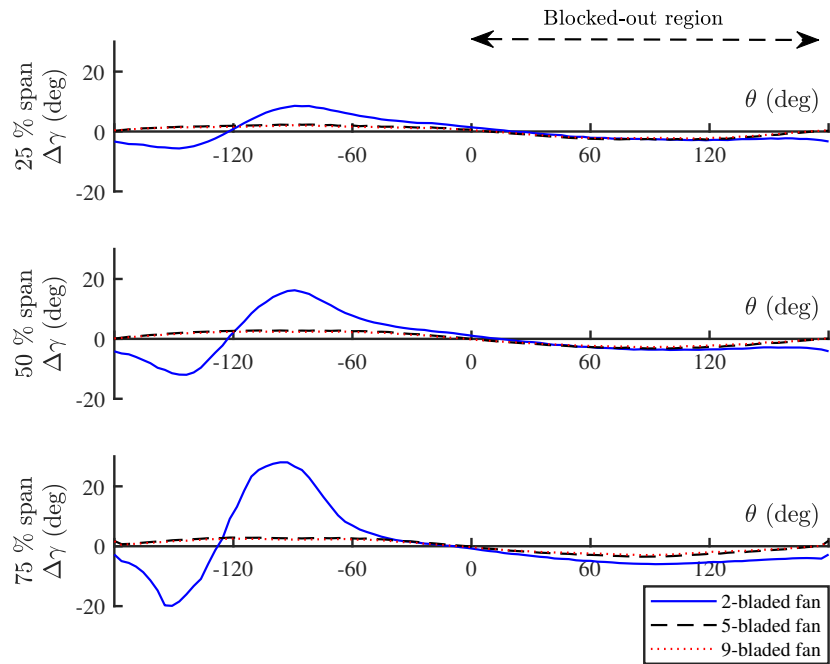
Figure 3.22: Circumferential variation of the absolute radial angles at different span fractions upstream of the blade row for the case of downstream blockage
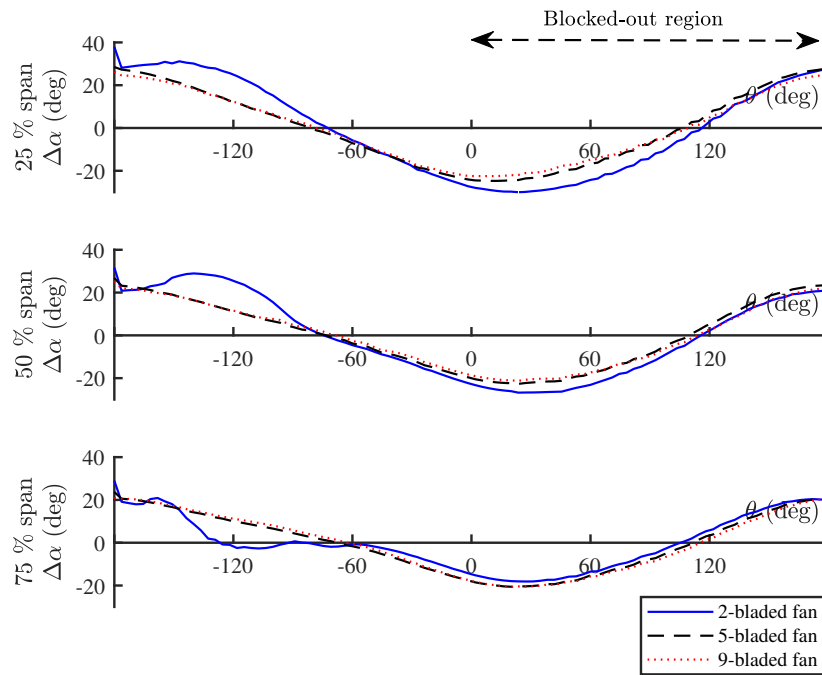
Figure 3.23: Circumferential variation of the absolute swirl angles at different span fractions downstream of the blade row for the case of downstream blockage
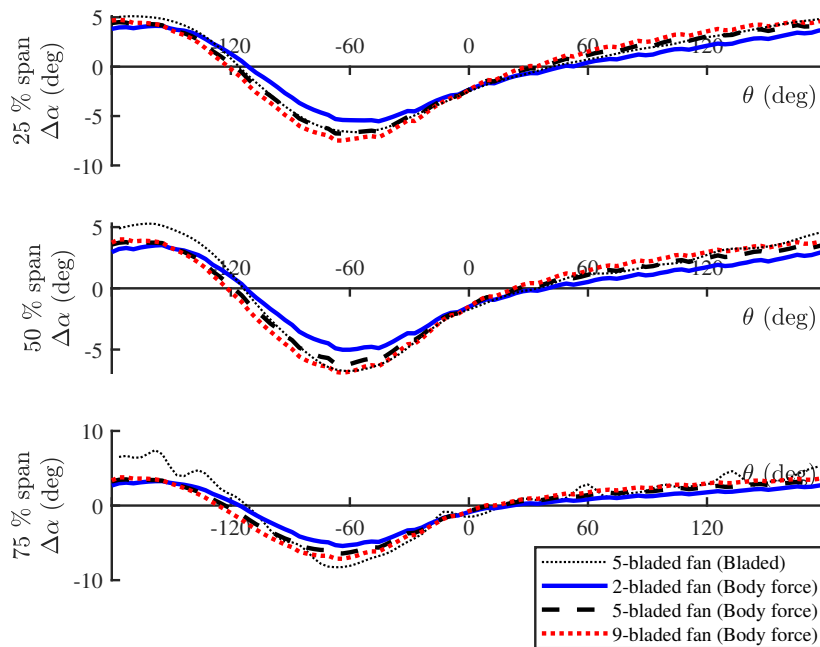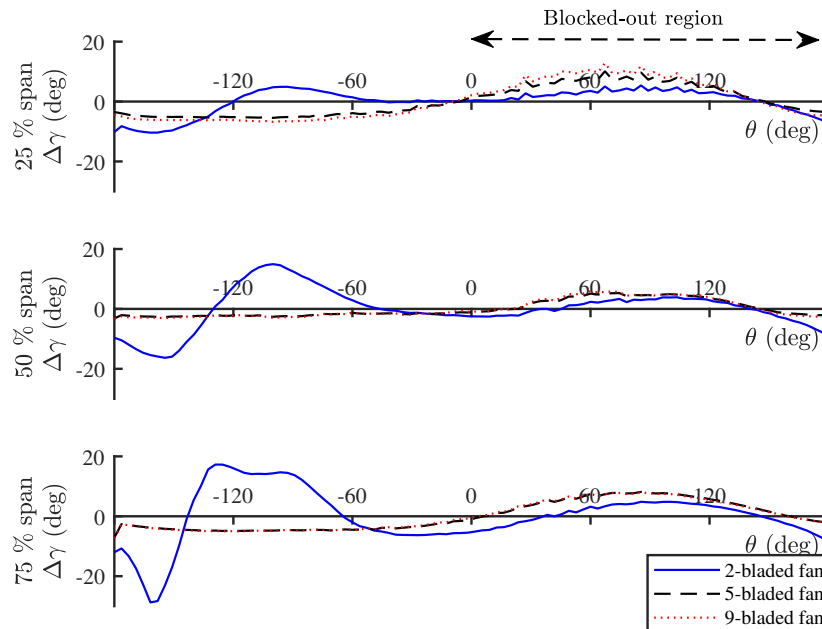

Figure 3.24: Circumferential variation of the absolute radial angles at different span fractions downstream of the blade row for the case of downstream blockage

3.5 Summary and Conclusions

In this paper, the accuracy of Hall's body force approach was assessed for the unexplored design space of low solidity fans with low design flow and work coefficients. The fan considered in this work has highly staggered blades as a result of the design values of ϕ and ψ. An assessment of the model accuracy was made for a range of flow coefficients and blade counts. A detailed investigation was conducted into the fundamental mechanisms that drive the changes in model accuracy for uniform flows. Subsequently, the model was used to capture distortion transfer in fans with low blade counts to assess the effect of the change of the distortion length scale to pitch ratio on the flow redistribution and distortion transfer of the fan.

The key findings of this paper are that (1) for uniform flow, the accuracy of the model improves in the limit of low blade count due to the reduction of the blade metal blockage effects and due to inaccurate spanwise flow distribution which actually improves the mass-averaged work coefficient, and (2) relatively high values of reduced frequency do not have a significant impact on predicted upstream influence or distortion transfer in non-uniform inflow, but very large distortion length scale to pitch ratios do reduce upstream flow non-uniformity and distortion attenuation through the rotor.

For a blade design with a given design work coefficient, the condition of maintaining near zero leading edge incidence at the choice of the design flow coefficient dictates the stagger angle of the blade. As the design flow coefficient decreases at a certain rotational speed and work coefficient, the blades require a successively higher stagger to maintain zero flow incidence at the leading edge. This increase in stagger of the blades causes a subsequent reduction in blade camber as the design flow coefficient decreases, thereby gradually unloading the blade. It is important to keep in mind the fact that this combination of low flow coefficient and low work coefficient creates

operating conditions for the fan which are entirely different from those in which Hall's model has previously been employed. The under-prediction of the work coefficient observed, as opposed to the over-prediction reported in several other studies, could be a consequence of this entirely different operating regime. The results of this paper suggest that Hall's model is an appropriate body force approach for simplified modeling of automotive cooling fans, including in installed under-hood environments which yield non-uniform flow. The under-prediction of work due to low solidity suggests a correction for this factor could be developed to improve the body force model performance.

3.6 Acknowledgments

References

[1] Mahmoud Khaled, Mohamad Ramadan, Hicham El-Hage, Ahmed Elmarakbi, Fabien Harambat, and Hassan Peerhossaini. Review of underhood aerothermal management: Towards vehicle simplified models. *Applied Thermal Engineering*, 73(1):842–858, 2014.

[2] Wei Ding, Jack Williams, Dinakara Karanth, and Sandeep Sovani. CFD application in automotive front-end design. In *Proceedings of the SAE 2006 World Congress & Exhibition*. SAE, 2006. SAE technical paper 2006-01-0337.

[3] M Franchetta, KO Suen, and TG Bancroft. Pseudo-transient computational fluid dynamics analysis of an underbonnet compartment during thermal soak. *Proceedings of the Institution of Mechanical Engineers, Part D: Journal of Automobile Engineering*, 221(10):1209–1220, 2007.

[4] Shankar Natarajan, Aditya Mulemane, and Pradip Dube. Underhood and underbody studies in a full vehicle model using different approaches to model fan and predict recirculation. In *Proceedings of the 2008 SAE World Congress & Exhibition*. SAE, 2008. SAE technical paper 2008-01-1173.

[5] Hak Jun Kim and Charn-Jung Kim. A numerical analysis for the cooling module related to automobile air-conditioning system. *Applied Thermal Engineering*, 28(14-15):1896–1905, 2008.

[6] CJ Meyer and DG Kröger. Numerical simulation of the flow field in the vicinity of an axial flow fan. *International Journal for Numerical Methods in Fluids*, 36(8):947–969, 2001.

[7] Constantine P Tzanos and Tai-Hsin Chien. A simple fan model for underhood thermal management analyses. Technical report, SAE Technical Paper, 2002.

[8] Ali Sahili, Bashar Zogheib, and Ronald M Barron. 3-d modeling of axial fans. *Applied Mathematics*, 4(4):632–651, 2013.

[9] W. G. Joo and T. P. Hynes. The application of actuator disks to calculations of the flow in turbofan installations. *Journal of Turbomachinery*, 119(4):733–741, Jan 1997.

[10] W. R. Hawthorne, N. A. Mitchell, J. E. Mccune, and C. S. Tan. Nonaxisymmetric flow through annular actuator disks: Inlet distortion problem. *Journal of Engineering for Power*, 100(4):604–617, Jan 1978.

[11] SJ Van der Spuy, FN Le Roux, et al. The simulation of an axial flow fan performance curve at low flow rates. In *ASME 2011 Turbo Expo: Turbine Technical*

Conference and Exposition, pages 425–434. American Society of Mechanical Engineers Digital Collection, 2011.

[12] Randi Franzke, Simone Sebben, Tore Bark, Emil Willeson, and Alexander Broniewicz. Evaluation of the multiple reference frame approach for the modelling of an axial cooling fan. *Energies*, 12(15):2934, 2019.

[13] ANSYS Inc. *ANSYS v18.2 User's Guide*. ANSYS Inc., Canonsburg, PA, 2019.

[14] Yuji Kobayashi, Itsuhei Kohri, and Yukio Matsushima. Study of influence of MRF method on the prediction of the engine cooling fan performance. In *Proceedings of the 2011 SAE 2011 World Congress & Exhibition*. SAE, 2011. SAE technical paper 2011-01-0648.

[15] DK Hall, EM Greitzer, and CS Tan. Analysis of fan stage conceptual design attributes for boundary layer ingestion. *J. Turbomach.*, 139(7):071012, 2017.

[16] JJ Defoe, M Etemadi, and DK Hall. Fan performance scaling with inlet distortions. *J. Turbomach.*, 140(7):071009, 2018.

[17] Andreas Peters, Zoltán S Spakovszky, Wesley K Lord, and Becky Rose. Ultrashort nacelles for low fan pressure ratio propulsors. *J. Turbomach.*, 137(2):021001, 2015.

[18] David J Hill and Jeffrey J Defoe. Innovations in body force modeling of transonic compressor blade rows. *International Journal of Rotating Machinery*, 2018, 2018.

[19] DJ Hill and JJ Defoe. Scaling of incidence variations with inlet distortion for a transonic axial compressor. *J. Turbomach.*, 2019. accepted.

[20] Teng Cao, Paul Hield, and Paul G Tucker. Hierarchical immersed boundary method with smeared geometry. *Journal of Propulsion and Power*, 33(5):1151–1163, 2017.

[21] FRANK E Marble. Three-dimensional flow in turbomachines, 1964.

[22] Y Gong, CS Tan, KA Gordon, and EM Greitzer. A computational model for short wavelength stall inception and development in multi-stage compressors. *J. Turbomach.*, 121:726–734, 1999.

[23] Emmanuel Benichou, Guillaume Dufour, Yannick Bousquet, Nicolas Binder, Aurélie Ortolan, and Xavier Carbonneau. Body force modeling of the aerodynamics of a low-speed fan under distorted inflow. *Int. J. Turbomach. Propuls. Power*, 4(3), 2019.

[24] Sho Sato, Nathan Spotts, and Xinfeng Gao. Validation of fan source term model constructed without blade geometry. In *Proceedings of the AIAA Scitech 2019 Forum*, page 1448. AIAA, 2019. AIAA paper 2019-1448.

[25] Quentin Minaker and Jeff Defoe. Prediction of crosswind separation velocity for fan and nacelle systems using body force models: Part 2: Comparison of crosswind separation velocity with and without detailed fan stage geometry. *Int. J. Turbomach. Propuls. Power*, 2019. Under review.

[26] The OpenFOAM Foundation. OpenFOAM v6, 2019.

[27] ANSYS Inc. *Turbogrid v19.2 User's Guide*. ANSYS Inc., Canonsburg, PA, 2019.

[28] FR Menter, R Langtry, and S Völker. Transition modelling for general purpose CFD codes. *Flow, turbulence and combustion*, 77(1-4):277–303, 2006.

[29] Patrick J. Roache. *Fundamentals of computational fluid dynamics*. Hermosa Publishers, 1998.

[30] Pointwise. *Pointwise v18.3R1 User's Manual*. Pointwise, Forth Worth, TX, 2019.

[31] The CGAL Project. *CGAL User and Reference Manual*. CGAL Editorial Board, 5.0.2 edition, 2020.

Chapter 4

Suitability Assessment of an Uncalibrated Body Force Based Fan Modeling Approach to Predict Automotive Under-hood Airflows

4.1 Introduction

As an integral part of vehicle thermal management (VTM), vehicle under-hood airflow simulations are crucial for predicting the engine bay flowfield and identifying the maximum component temperatures for the numerous underhood installations. The radiator fan is a key component of the cooling module as it is a major driver of the airflow in the engine compartment, and is particularly indispensable for high load cases when ram air provides insufficient cooling [1]. The prerequisite for obtaining an accurate prediction of the under-hood flowfield is a robust fan simulation approach which can yield an accurate distribution of the air stream through the various heat exchangers and other underhood installations.

The ever-increasing complexity of vehicle drive-cycles calls for the testing of the fan in a wide spectrum of scenarios with varying driving conditions and engine loads, which may involve tens to hundreds of simulations for a typical vehicle development program. As with all turbomachinery, the flow field generated by the automotive fan is inherently unsteady in nature because the fan blades rotate at thousands of revolutions per minute. This necessitates the use of fully-transient simulations to resolve the small time-scales triggered by the high rotational frequencies of the fan even if the interest only lies in finding steady-state operating points for the full vehicle [2, 3].

However, drive cycles used to test the thermal integrity of automotive components and performance of heat-exchanger packages are on the order of minutes, and this disparity in time scales leads to prohibitively long computation times for the full vehicle. To achieve the required turnaround times with limited computational resources, it has become the norm to use simplified models which can resolve the flow field through the fan using steady Reynolds-averaged Navier Stokes (RANS) solutions.

4.1.1 Inadequacy of State-of-the-art Steady Fan Modeling Techniques

The multiple-reference frame (MRF) model is one of the most commonly used steady-state approaches for under-hood cooling flow simulations. This approach involves the definition of a "rotating" domain which incorporates the fan geometry. In this region, the flow equations are solved in the rotating frame of reference of the fan rotor in a steady sense. Although the MRF approach is much cheaper than a fully-transient simulation, the drawbacks associated with it have been well-documented in the literature. In their studies, Gullberg et al. found the MRF predictions to be very sensitive to user-specific methodology such as the size and axial extent of the rotational domain, and the clocking position of the fan blades relative to the surrounding components [4–6]. Owing to the fact that the MRF approach is a steady-state technique, it cannot be applied to any transient drive-cycles of interest [2]. It has also been found to yield inaccurate results in cases of non-uniform inlet conditions [7]. This makes the MRF technique unsuitable for an automotive fan operating in a compact and convoluted under-hood environment with complex flow paths, even if the overall flow conditions are steady.

Alternatives to the MRF fan modeling approach include the momentum source models such as the actuator disk (AD) and the body force model (BFM). Both of these techniques do not require the construction of fan blade geometry within the simulation and can predict the fan performance at a reduced cost using steady-state

flow approximations. In the actuator disk approximation, the fan is represented by a thin interface which acts as a momentum source. The fan curve models utilized by Natarajan et al. [8] and Kim and Kim [9] are examples of actuator disks which realize the pressure rise through the fan as a function of the volumetric flow rate using experimentally-derived fan performance data. The body force models involve a similar methodology, however the momentum and energy sources are distributed across a fan-representing volume instead of a thin interface. Moreover, body force approaches can calculate source terms based on either experimental data or analytical models, or a combination of both.

Multiple variations of the actuator disk and body force models are available in the literature, however the majority of these models require calibration with some form of experimental or higher fidelity data, or suppress/ignore either (or both) of the radial or tangential components of the velocity field [2, 10–13]. Numerous studies have pointed out that neglecting the swirl and radial flows through the fan subjected to non-uniform inlet conditions has implications for the accuracy of the simplified fan modeling techniques [10, 14–16]. For example, the actuator disk approach employed by Van der Spuy et al. to simulate the effect of axial fans assumed that the flow enters and exits the fan in separate annular rings and it completely ignores the effect of radial flow on the fan blades [16]. However, this assumption is not always true, especially at low flow rates, as pointed out by Meyer and Kröger [10]. The fan static pressure rise curves obtained by Van der Spuy et al. found the actuator disk method to under-predict the static pressure rise values by as much as 37% for the lowest volumetric flow rates used in their studies and therefore the model had to be calibrated with empirical data for correction of performance [15].

In a tightly packed under-hood environment where flow blockage upstream or downstream of the fan can create significant radial and circumferential flow non-uniformities, it becomes imperative to consider experimental or higher-fidelity results

for calibration and/or validation of these momentum source term models, which is a major drawback of these approaches. An ideal fan model for simulating under-hood and underbody flows would have the ability to predict the time-averaged, steady-state response of a fan with accuracy at least as good as calibrated approaches, but without explicitly requiring a priori knowledge of the fan performance. Furthermore, it should be able to do so at a low computational cost while capturing all of the significant flow features which can be suppressed by traditional reduced-order fan modeling techniques. Eliminating the experimental calibration of the simplified fan model would significantly reduce the overall effort, time, and cost involved in simulating underhood and underbody flows.

4.1.2 Uncalibrated Body Force Model Approach

A recent body force based approach developed by Hall, Greitzer, and Tan uses an analytical approach to calculate source terms required to mimic the work input and pressure rise through a fan [17] . This model is particularly interesting because it does not require calibration with experiments nor high-fidelity computations, and it has been found to accurately predict the total enthalpy rise across a low speed fan stage to within an accuracy of 3%. This modelling approach has been widely used in aerospace applications (e.g. Defoe, Etemadi, and Hall [18]), but it's suitability for automotive fans placed in an underhood setting has never been tested before. Most of the previous studies with Hall's body force model have been restricted to aircraft engine fans and compressors with at least 20 blades per row [17, 19–22], while automotive cooling fans often have fewer than half that many. For uniform flows, the model produces a circumferentially-averaged "smeared-out" version of the actual flowfield. For non-uniform inflows, the model works in a "quasi-axisymmetric" sense which is analogous to the working of a low-pass filter. The model suppresses any short-wavelength perturbations which are comparable to the length scale of the

blade pitch (blade-to-blade distance) and instead, produces a time-averaged response of the fan to the local flow conditions as illustrated in Figure 4.1. This behavior is expected to have implications for the accuracy of the model for low blade count automotive fans which have a large length scale of blade-to-blade non-uniformities because of higher blade spacing.
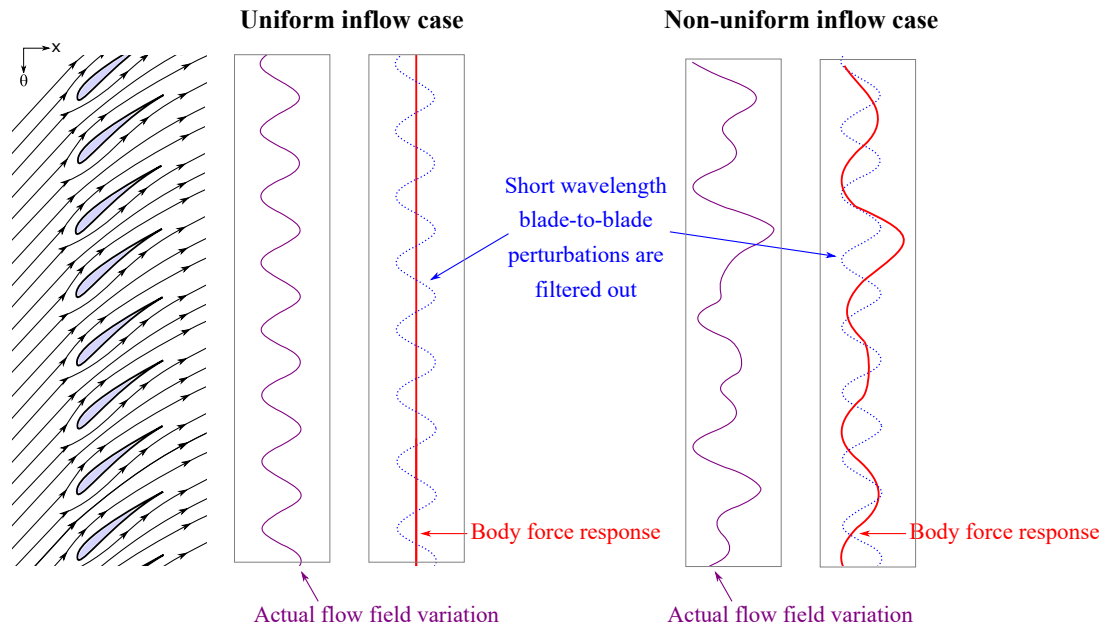
Figure 4.1: Hall's model performs analogous to a low pass filter. Short wavelength blade-to-blade flow perturbations are not captured in the model response.

A recent study conducted by Saini and Defoe [2] assessed the accuracy of Hall's model for low solidity automotive fans in clean flows, and found the accuracy of the model predictions to be highly dependent on the blade count or for a given chord, the solidity (ratio of blade chord to blade pitch), of the fan. The model was found to under-predict the mass-averaged total enthalpy change through the fan for uniform inflow cases but for blade counts as low as 5, it could accurately reproduce the flow angle variation downstream of a fan subjected to non-uniform inlet conditions.

The underhood environment involves highly coupled and complex fluid dynamics phenomena due to the close proximity of the several components placed in a compact

underhood space [23]. Unlike the study conducted by Saini and Defoe [2], the fan is not placed in a simple duct with well-defined inlet/outlet boundary conditions in the vicinity of the fan for a full vehicle computation. In fact, both the pressure rise and the flow rate through the fan are a small part of the solution of the entire vehicle domain. Saini and Defoe's [2] study indicated that Hall's model could be a promising candidate for an uncalibrated automotive fan modeling approach but significant uncertainty remains over the model's response as part of the complex under-hood architecture, and whether the model needs additional corrections to improve it's predictions. This work serves to remove this uncertainty.

Moreover, Hall's model is a "normal force" model only, which means it does not take into account the pressure losses due to the blade profile or skin friction. Normal force models are usually accompanied by "parallel force" models which serve to mimic the pressure losses that occur in a real blade passage [24, 25]. Saini and Defoe's previous study with Hall's model only focused on friction-less fan blades, but real blades cause skin friction and blade profile losses. It is unknown if the model predictions would improve when compared to bladed calculations if blade friction is also considered. Also, their study was performed in the cell-centered open-source CFD solver OPENFOAM v6 [26] and it is unknown if a commercial node-centered solver such as STAR-CCM+ [27] would alter the model response in any way. This question is important to answer since the final full-vehicle simulations are performed in STAR-CCM+. This work serves to answer several questions:

1. How do the original model's predictions compare to bladed simulations without viscous blade surfaces in STAR-CCM+?

2. Does the augmentation of the blade loading force (via the addition of an amplification factor) attenuate the under-prediction of total enthalpy rise as observed by Saini and Defoe [2] in their preliminary study?

3. Does the augmented model require addition of a loss formulation to better capture the actual flow features and/or improve it's predictions?

4. How does the model performance compare to other best-practice calibrated fan approaches used in the industry for full vehicle steady drive-cycle computations?

4.1.3   Key Findings and Chapter Outline

For uniform inflow cases, the model was found to highly under predict the fan total enthalpy rise (or fan work coefficient). The amplification of the model fixed the problem of under prediction, however the agreement of the local velocity field features worsened in general. The addition of a loss model was found to have a negligible impact on the total pressure rise predictions since Hall's original model could reasonably predict the total pressure rise which governs the flow rate.

Hall's original model, without any modifications, was then used to run full vehicle computations for a range of vehicle speeds to capture the mass flux distribution across the heat exchangers. The model predicted the flow rate through the radiator to within 8% of the experimentally-measured value at idle. At high vehicle speed, the accuracy improved to 1%. The uncalibrated model had equal or better accuracy in predicting the flow rate compared to the current best-practice calibrated fan modeling techniques used in the industry.

The rest of this chapter is organized as follows: we first begin with the analysis of the body force model for the case of uniform inflow and compare it to corresponding MRF results. Three versions of the model are tested: i) Hall's original body force model, ii) an amplified-force version of Hall's model, ii) an amplified-version of Hall's model in conjunction with a loss model. Subsequently, the full vehicle computations are carried out with Hall's original body force model and the results are compared to experimental data as well as other fan modeling approaches.

4.2 Body Force Modeling

This section encompasses a brief description of Hall's body force model and the loss model formulation. For more detailed information about Hall's model, the reader is advised to refer to Hall's original work [17] or a previous paper published by the author(s) [2]; Thollet's thesis [24] contains the loss model details. The basic concept of a body force model is shown in Figure 4.2, which illustrates the fan rotor geometry studied in this chapter and its equivalent domain for a body force model. In the latter representation, the bladed region is replaced with an axisymmetric fluid volume defined by the swept volume of the blades. Within the volume, momentum sources (and energy sources for compressible flow) are responsible for generating the flow turning, enthalpy rise, and pressure changes through the blade passage [17].
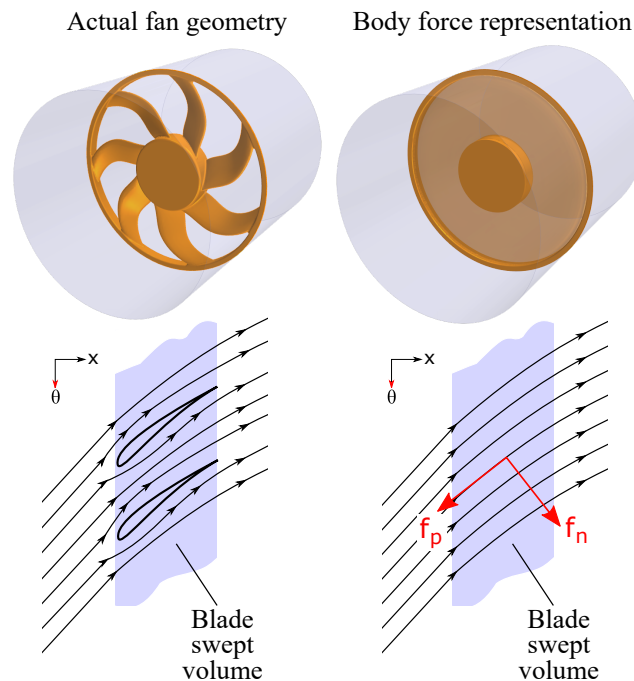
Figure 4.2: Flow through a real blade passage (left) and through a body force region (right). The force can be split into two components, i) the normal force f_n, responsible for pressure rise and flow turning, and ii) the parallel force f_p, responsible for generating blade profiles losses.

Hall's normal force model is only responsible for generating the flow turning or the pressure rise through the blade passage. The source term distribution is defined as a function of the local flow conditions and the blade geometry, which is characterized by the distribution of the camber surface normals, $\hat{n}(x, r)$. In a 2D sense, the camber is a line joining the leading and trailing edges of an aerofoil, equidistant from the upper and lower surfaces as shown in Figure 4.3. These lines stacked up together through the span of a 3D blade form the camber surface.
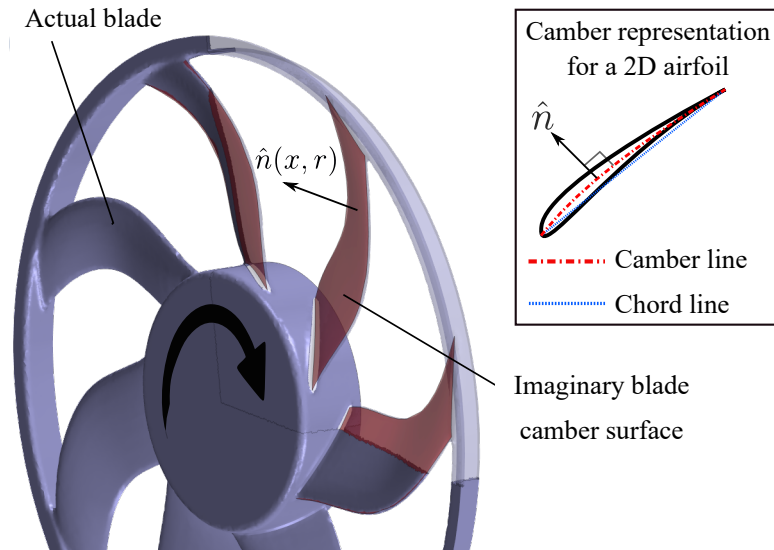
Figure 4.3: Illustration of the fan blade camber surface

The momentum source per unit mass, $\vec{f}_n$, in Hall's model is

$$|\vec{f}_n| = \frac{(2\pi\delta)(\frac{1}{2}\vec{W}^2/|\hat{n}_\theta|)}{2\pi r/B},$$ (4.1)

where $\vec{W}$ is the relative velocity vector, B is number of blades, r is distance from the rotation axis, and δ is the deviation angle of the flow from the blade camber surface. The magnitude of the blade loading force $\vec{f}_n$ scales linearly with the deviation δ in a direction that pushes the flow towards the blade surface as illustrated in Figure 4.4.

Hall's body force model does not capture any viscous losses due to skin friction. The inclusion of total pressure losses can potentially alter the local distributions of the
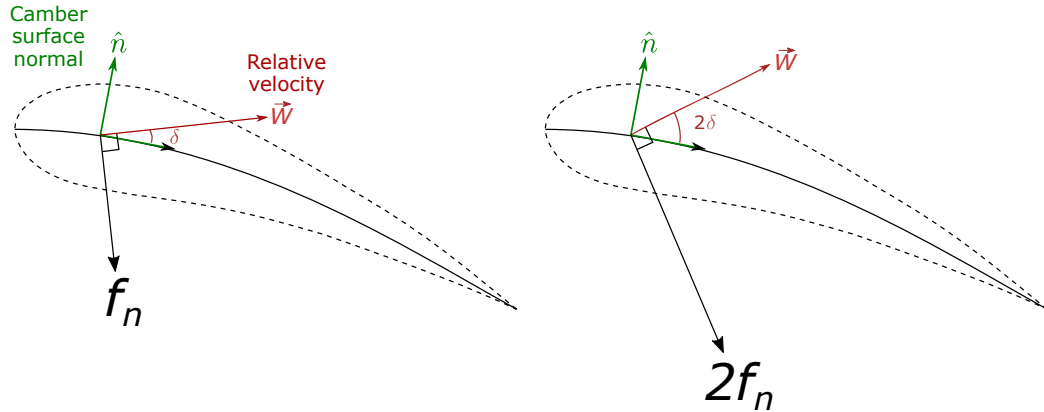
Figure 4.4: Blade loading force doubles if the deviation of the flow δ doubles

velocity and work input, and have a major impact on the overall model performance. To study this, a parallel force model formulation has been adapted from Thollet's work [24]. This model has already shown promising results for boundary-layer ingesting aircraft fans which operate in typically high relative Reynolds number flows. [24, 28]. The parallel body force component $\vec{f_p}$ acts parallel to the relative velocity vector and accounts for the pressure losses through the blade row. The formulation for the loss model is:

$$|f_p| = \frac{(2C_f + 2\pi(\delta - \delta^{\eta_{max}})^2)(\frac{1}{2}\vec{W}^2/|\vec{n_\theta}|)}{2\pi r/B} \tag{4.2}$$

where C_f is the local skin friction coefficient based on an empirical turbulent flat plate correlation, and a local chordwise Reynolds number:

$$Re_x = \frac{\rho W x}{\mu} \tag{4.3}$$

$\delta^{\eta_{max}}$ is a simple calibration parameter which can be easily established by using the deviation field generated by the model without the off-design term at the maximum efficiency design point.

4.3 Analysis of Body Force Model Accuracy for Uniform Inflow Cases

This section details the analysis done on the body force model for uniform inflow cases. The section begins with a brief description of the fan geometry and the computational domain. Subsequently, the performance metrics used for assessing the body force implementation are described. Results are presented for three versions of the model: i) Hall's original body force model, ii) an amplified-force version of Hall's model, ii) an amplified-version of Hall's model in conjunction with a loss model.

4.3.1 Computational Domain for Uniform Inflow Test Cases

The fan geometry and computational domain for studying the axisymmetric through-flow case is the same as the one used by Saini and Defoe [2]. The key design parameters for the fan are listed in Table 4.1 and the fan geometry is shown in Figure 4.2. The geometry is a 7-bladed shrouded automotive fan placed inside a simple annular duct as shown in Figure 4.5. A 2 degree wedge shaped computational domain is created using POINTWISE [29] with constant hub and casing radii.

Table 4.1: Design characteristics for the base fan model

Parameter	Value
number of blades B	7
aspect ratio AR	5.56
hub solidity σ_{hub}	0.46
tip solidity σ_{tip}	0.18
r_{hub}/r_{tip}	0.388
design flow coefficient $\phi_{des} = \bar{u}_x^M/U_{\mathrm{mid}}$	0.215
design rotational speed N	2683 rpm

All simulations in this chapter were carried out using the commercial CFD solver STAR-CCM+ [27]. The flow is modeled as incompressible because of the low Mach numbers encountered in automotive under-hood airflows. For simplicity, all walls
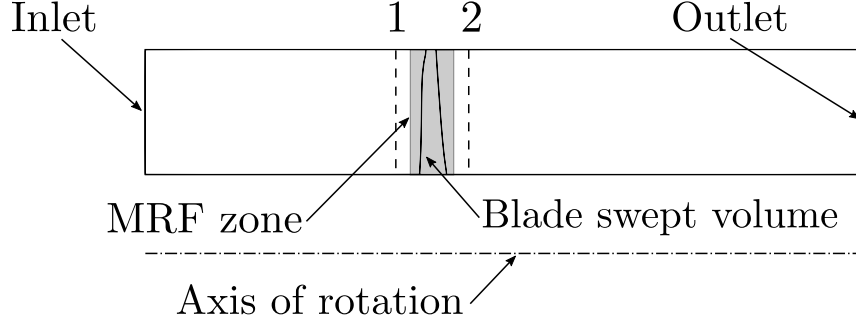
Figure 4.5: Meridional view of the computational geometry

are defined as free-slip or zero shear stress surfaces. The velocity inlet is used to set the incoming mass flow rate and a zero static pressure outlet is employed. The results for uniform inflow cases are assessed against corresponding single-passage MRF simulations.

Grid independence for the computational domain was reached at the same cell count as the one used by Saini and Defoe [2] in the open-source CFD solver OPEN-FOAM v6. The grid selected has $8.72X10^4$ cells. The cell size distribution is such that there are 40 cells in the axial direction and 100 cells in the radial direction inside the blade swept volume. There is a single cell in the circumferential direction.

4.3.2 Performance Metrics of Interest

The metric of interest for comparison of body force model performance between different solvers in this chapter are the the work coefficient of the fan and the total pressure rise coefficient. The work coefficient is defined as:

$$\psi = \frac{\Delta \bar{h}_{\mathrm{t}}^{\mathrm{M}}}{U_M{}^2} \tag{4.4}$$

where $\Delta \bar{h}_{\mathrm{t}}^{\mathrm{M}}$ is the mass-averaged total enthalpy change across the fan, and $U_{\mathrm{M}} = \omega r_{\mathrm{mid}}$ is the midspan blade speed. ω is the angular velocity of the rotor. The total enthalpy is simply defined from the Euler turbine equation as $h_{\mathrm{t}} = \omega r u_\theta$ where the tangential

velocity u_θ is calculated directly from the velocity field. The far-upstream flow is axial so the upstream total enthalpy, $\bar{h}_{t,1}^{M}$, is defined to be zero.

The total pressure coefficient is defined as:

$$\psi_{tt} = \frac{\Delta \bar{p}_t^M}{\rho U_M{}^2} \qquad (4.5)$$

where $\Delta \bar{p}_t^M$ is the mass-averaged total pressure change between the upstream and the downstream measurement plane locations. For Hall's original body force model, $\psi = \psi_{tt}$ because there are no total pressure losses and thus the fan is operating at 100% efficiency (unless there is flow separation).

4.3.3 Results for Hall's Original Body Force Model

Figure 4.6 shows the enthalpy rise characteristics for the clean body force model compared against corresponding MRF simulations for a range of flow coefficients. For a fully inviscid body force case, with no profile losses or flow separation, the work coefficient or total enthalpy rise can be used as a surrogate for the total pressure rise coefficient because the fan operates at 100% efficiency. The results show a similar trend to the one observed by the authors in an identical study performed in the open-source software OPENFOAM V6 [2]. The general trend of the variation of work coefficient is successfully captured by the body force model, however the work coefficient is highly under-predicted compared to the results obtained from the single-passage MRF computations with all free-slip walls. At the design point, the total enthalpy rise is under predicted by 26% which is unacceptable in an industry setting.

Figure 4.7 shows the axial, radial, and tangential velocity components of the two cases at the design point. The axial and radial velocities are well-matched for the two cases for the majority of the span despite the differences in work input. As observed by Saini and Defoe [2], there is a radially outward shift of streamlines in
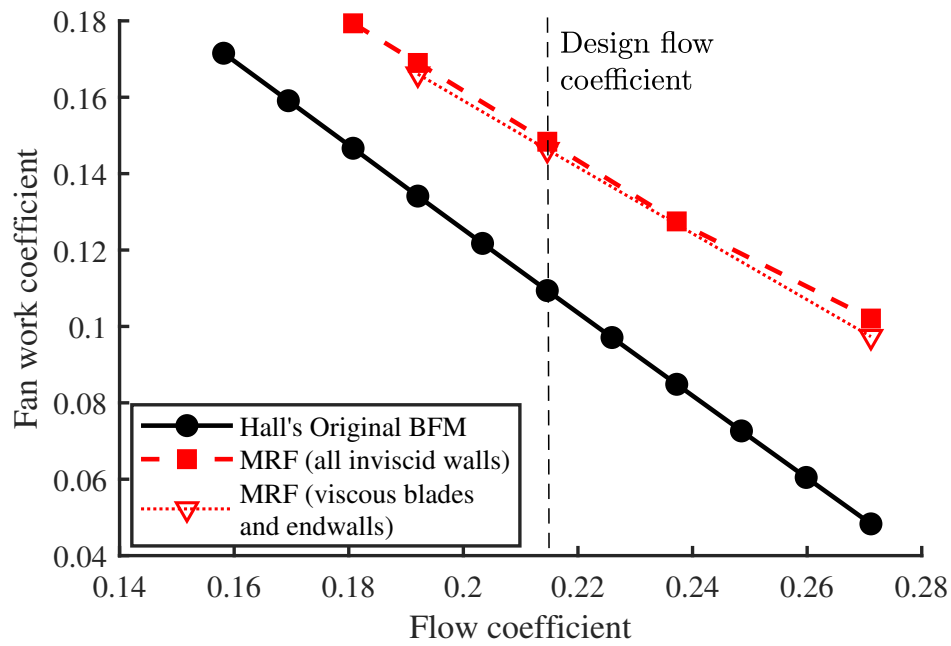
Figure 4.6: The total enthalpy rise characteristics obtained from Hall's original model and the multiple-reference frame (MRF) simulations
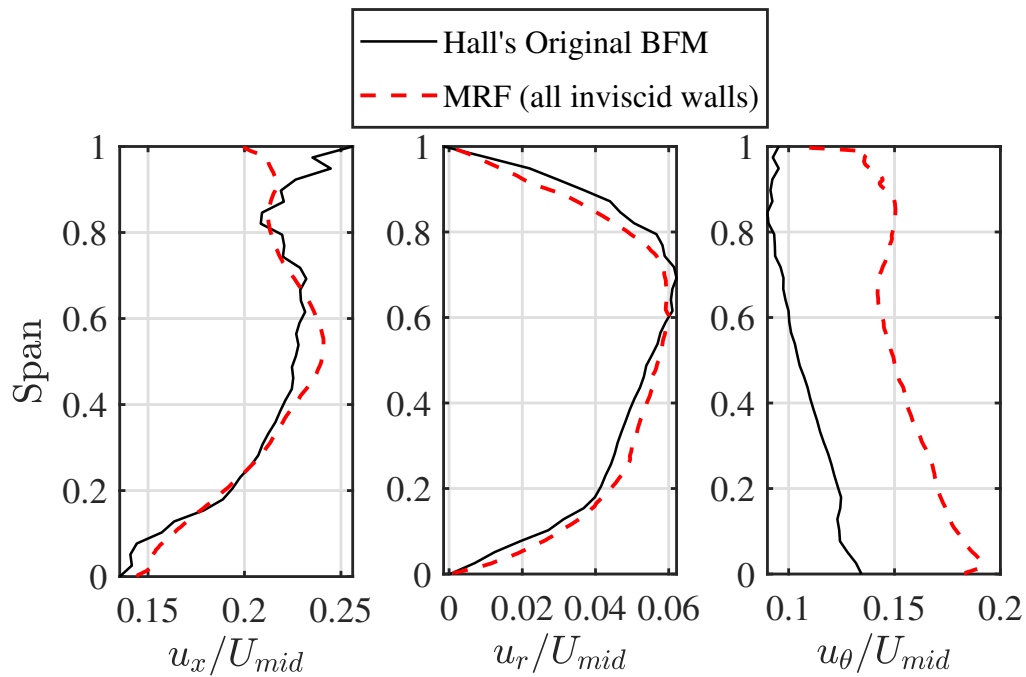
Figure 4.7: Velocity profiles for Hall's original model compared to MRF simulations for the design point

the body force case, indicated by the higher axial velocities for the body force model seen in the outer 20-30% of the span. The differences in radial flow distribution yield changes in the spanwise profiles of tangential velocity, and hence the total enthalpy rise ($h_t = \omega r u_\theta$), at the trailing edge. The increased flow in the outer 30% span for the body force model results in significantly lower flow turning (or total enthalpy rise), driving the under-prediction of the mass-averaged work coefficient.

The agreement of flow deviation from the blade camber surface (see Figure 4.8) obtained from the two models improves as one moves towards the outer span (until 80% span), contrary to what the plots of tangential velocities might suggest.
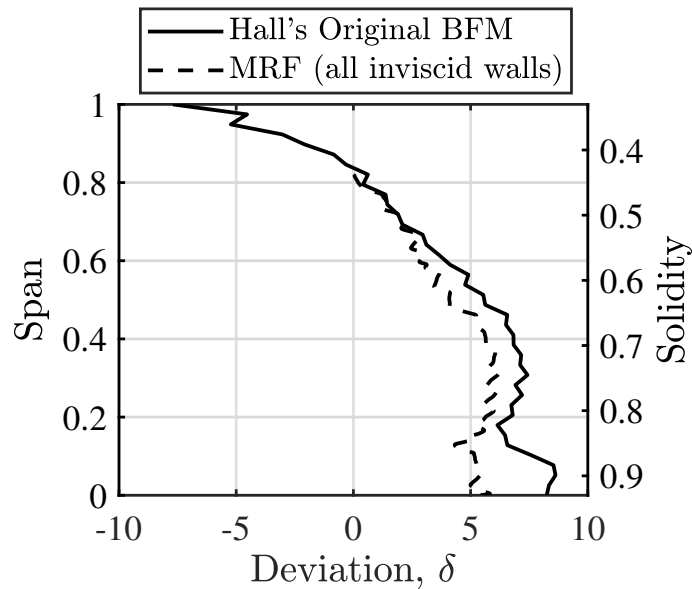
Figure 4.8: Deviation values for Hall's original body force model and the MRF simulations for design point (data in the outer 20% of the span is missing due to numerical errors)

Another interesting observation is that the deviation agreement improves as the solidity values decrease until 80% span (the data in the outer 20% span is missing due to numerical errors). Looking back at Equation 4.1, the blade loading force scales linearly with the solidity ($\frac{1}{2\pi r/B}$ for a unit chord length), and the deviation, δ. Figure 4.8 refutes the idea that a low solidity is the key driving agent for the under-predictions

of the total pressure rise. The observations of surprisingly good agreement of the deviation in the outer span and a poor total pressure rise agreement in the same region are hard to reconcile. However, considering that low blade count fans have significant blade-to-blade variation of flow deviation, it may suggest that in the limit of low blade count (or low solidity) the blade loading force may not be a linear function of the deviation δ anymore.

4.4 Implementation of an Amplified Version of Hall's Body Force Model

Because of no clear correlation between the under-prediction of the deviation and the solidity variation through the blade span, it was challenging to introduce a deviation and/or solidity correction to diminish the extent of the under-prediction exhibited by the model as compared to the single-passage MRF computations. Therefore, the authors attempted to introduce a simple amplification factor for the intensity of the body force model in the following fashion:

$$|f_n| = AF \frac{(2\pi\delta)(\frac{1}{2}W^2/|n_\theta|)}{2\pi r/B}, \tag{4.6}$$

where the amplification factor, AF is set to yield a work coefficient equivalent to the one observed in the single-passage, all free-slip walls MRF computations for the design case. The value of AF was determined iteratively.

Figure 4.9 shows the fan characteristics obtained from the amplified model along with the ones obtained from the original model and the bladed simulations. Only the total pressure coefficients are shown for brevity, and also because in a full vehicle computation, the total pressure differential across the fan sets the mass flow rate through it. Unsurprisingly, the overall total pressure coefficients improve in agreement. It is interesting to note that the amplification of the force causes the slope of the characteristic to become even steeper as compared to the fan characteristic curve

obtained from the MRF simulations. This suggests that the model perceives the blade geometry to be different that it actually is. It would also cause the model to predict higher than actual total pressure rise at low flow coefficients (until it experiences stall indicated by the sharp drop in total pressure rise for MRF case seen in Figure 4.9).
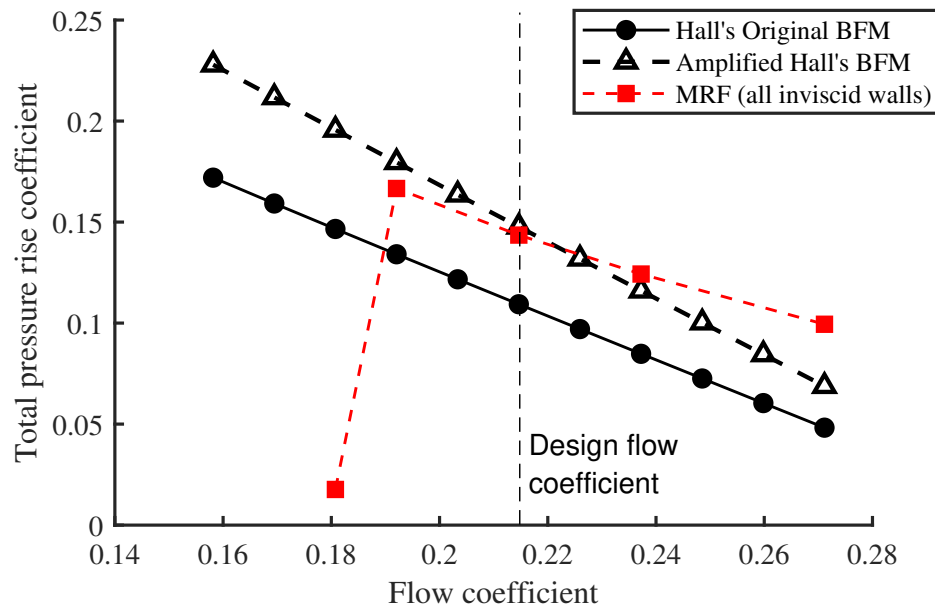
Figure 4.9: Fan characteristics for amplified Hall's model compared to the original model and the bladed simulations

The axial and radial velocity components obtained from the amplified model, as shown in Figure 4.10, worsen in agreement in general. The amplification does not improve the *shapes* of the profiles in any significant way and particularly, it is not able to capture the "kick-out" observed in the outer 50% span of the tangential velocity and the work coefficient profiles (see Figure 4.11). The results suggest that the amplification factor has potential to improve the flow turning, however it has to be traded off with a poor axial and radial velocity agreement. The model could be programmed to only amplify the tangential component of the loading force, $\vec{f_n}$, however it may cause nonphysical behavior as the force will no longer be normal to the relative streamlines.
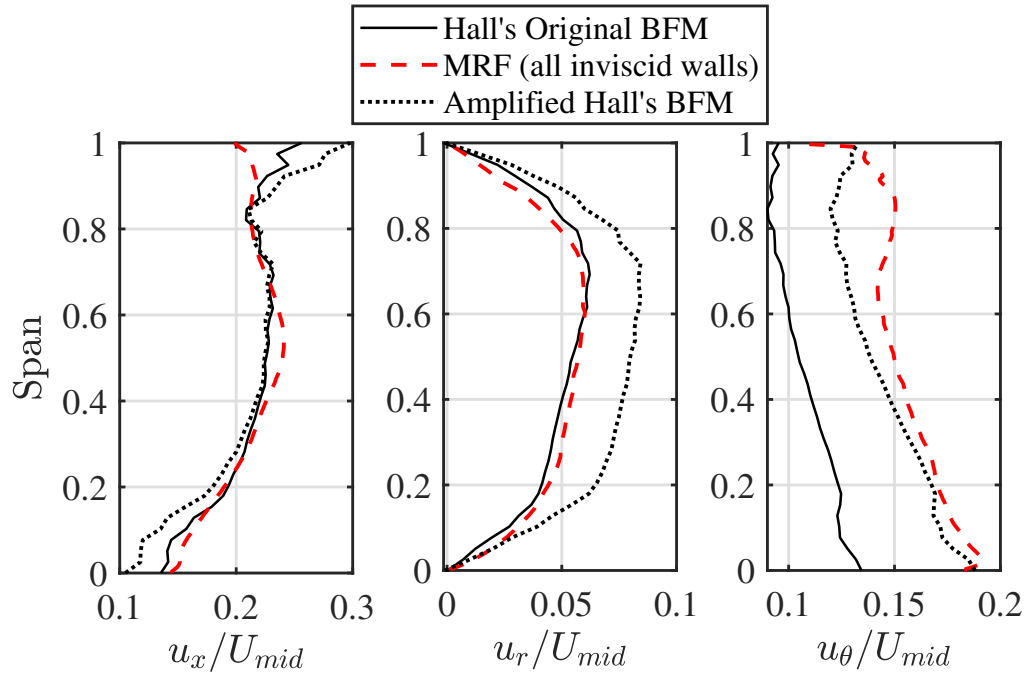
Figure 4.10: Velocity components for Hall's model with and without amplification at design operating point
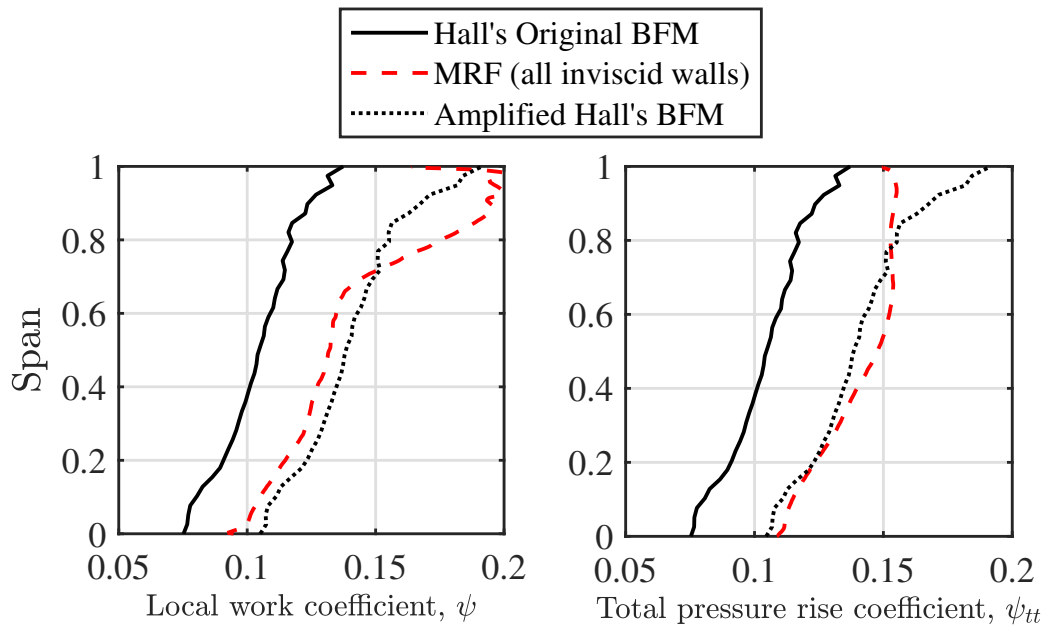
Figure 4.11: Work and pressure coefficient profiles for Hall's model with and without amplification at the design operating point

4.5   Implementation of a Loss Model

Although the addition of an amplification factor attenuated the extent of the under-prediction exhibited by the model to a great extent (as compared to **free-slip** MRF computations), the augmented model requires a loss formulation to capture the total pressure losses that occur in a real blade passage with wall friction. Therefore, the loss model described in Section 4.2 is used in conjunction with the amplified version of Hall's model for further analysis, and the results are compared to multiple-reference frame (MRF) simulations with viscous (no-slip) blade surfaces and endwalls.

Figure 4.12 shows the fan characteristics obtained for the combined version of Hall's model with the loss model. The addition of the loss model has a negligible effect on the predicted total pressure coefficient values. It is important to mention that the flat plate turbulent skin friction correlation used for the loss model described in Section 4.2 is based on the assumption that the fan is operating in a fully turbulent regime. However, the low Reynolds numbers[1] flows seen in automobile underhood environments hardly ensure a fully turbulent operation regime for the fan blades. Clearly, the loss model used for the fan is not producing significant total pressure losses; this might suggest that the friction correlation needs to account for the portions of the blade surfaces operating in laminar/transitional regimes.

Figure 4.13 shows the spanwise velocity component profiles obtained with the combined model formulations. When compared to the viscous MRF case, the velocity components obtained from the original model show relatively better agreement. Moreover, even with the addition of the loss model, the amplified version of Hall's body force formulation over-predicts the fan work input as well as the total pressure rise as evident from Figure 4.14.

---

[1]Local chordwise Reynolds numbers defined in Equation 4.3 range from 6 to 100,000 in the body force volume, at design operating point
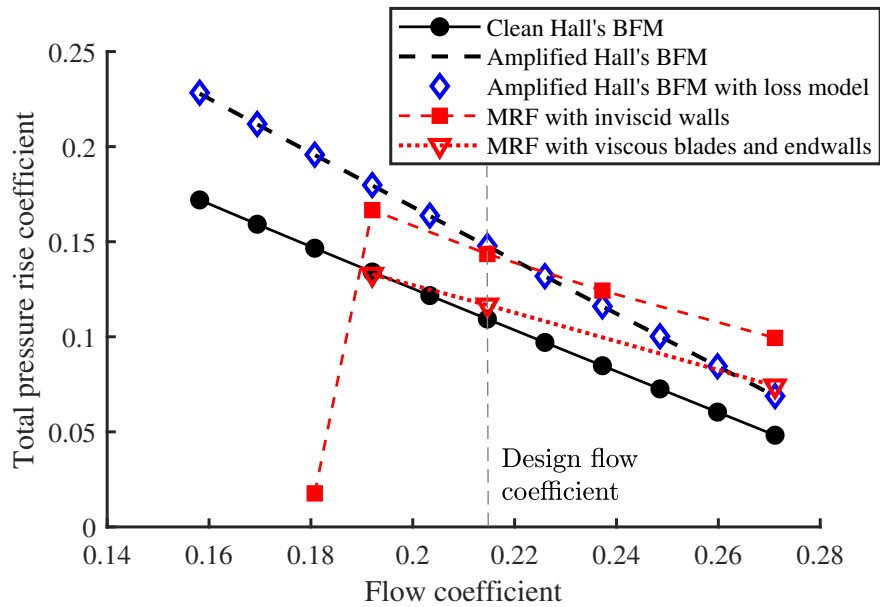
Figure 4.12: Fan characteristics for Hall's original model, amplified version of Hall's model, amplified version of Hall's model combined with the loss model. Data compared to multiple-reference frame simulations with a) all inviscid walls, b) no-slip blades and endwalls.
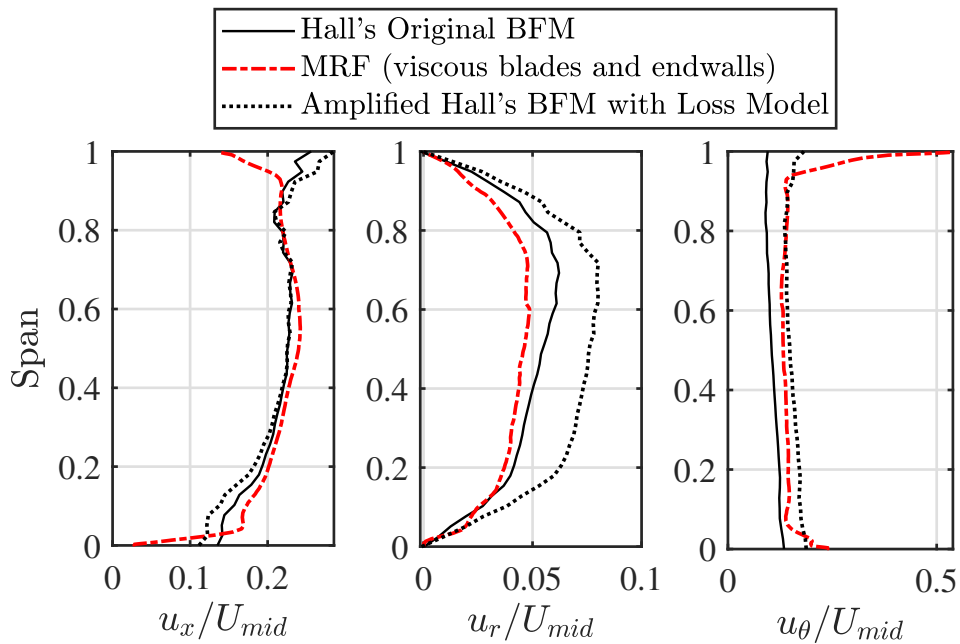
Figure 4.13: Spanwise profiles of velocity components for combined amplified version of Hall's model and loss model, at design operating point. Data compared to multiple-reference frame simulations with no-slip blades and endwalls.
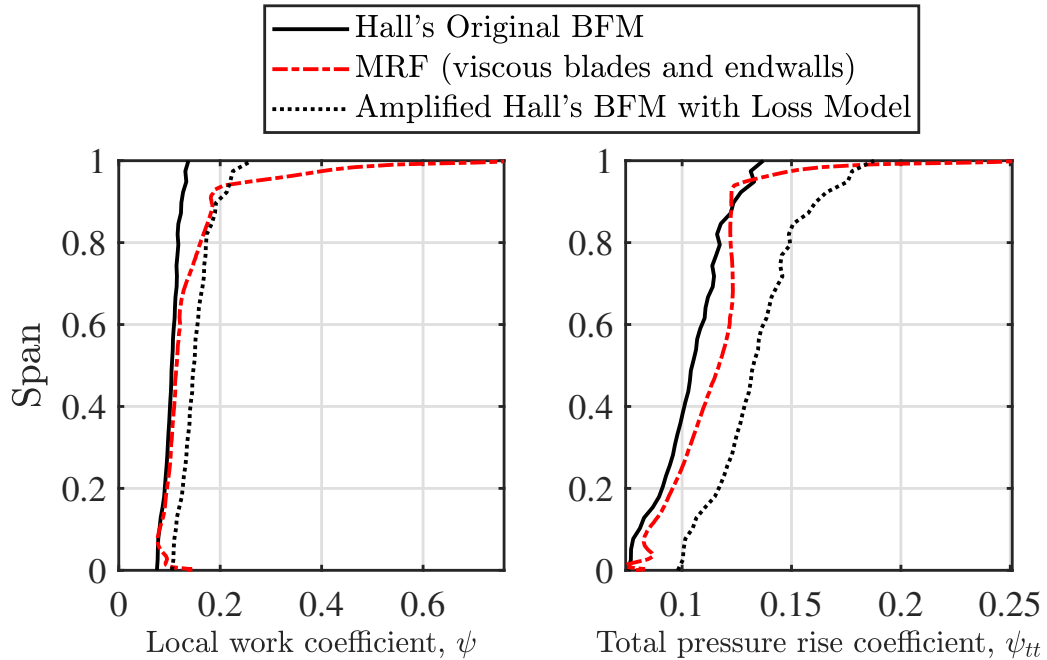
Figure 4.14: Spanwise profiles of work and total pressure coefficients for combined amplified version of Hall's model and loss model, at design operating point. Data compared to multiple-reference frame simulations with no-slip blades and endwalls.

Due to the lack of improvement in the performance of the body force model with the addition of the amplification factor and the losses, only the original model is chosen to be used for further analysis of the model's response in a full vehicle simulation.

4.6   Full Vehicle Setup with the Body Force Model

This section gives a brief overview of the full vehicle setup used for testing the body force model. A complete external and internal flow simulation was performed on a full vehicle placed in a virtual wind tunnel to assess the performance of the fan as a part of the entire cooling system. The results obtained from Hall's original model are compared against a current best-practice calibrated body force type approach used in industry. More details can be found in the following sections.

4.6.1 Geometry and Computational Domain

The automotive geometry used in this work is an SUV/minivan type car model provided by our industry partner. The full vehicle model is placed in a virtual wind tunnel as illustrated in Figure 4.15. The underhood architecture includes detailed geometry of several components which provide major obstruction to the flow such as the engine block, radiator package, transmission and oil cooler, chassis, suspension, wheels, bumper fascia, cabin floor, front grills and openings, etc.. The complex shapes of the heat exchangers are not considered, however they are represented by simple rectangular blocks of porous media.

The commercial CFD solver STAR-CCM+ [27] is used to create a trimmed cell mesh for the entire wind tunnel and vehicle model geometry, and to run the computations. The actual fan geometry is replaced by a body force volume in the computational domain as shown in Figure 4.16. Prism layers were added to wall boundaries to resolve any high gradients close to the walls. The mesh generation process follows best practices established based on an in-depth study for similar vehicle configurations by our industry partner and has been determined to yield grid independent results. The final body force volume contains about 1.27 million cells, while the entire computational domain consists of about 58.0 million cells.

A constant total pressure boundary condition was used at the tunnel entrance and a specified mass flow rate was imposed at the tunnel outlet to set the speed of the vehicle. The *segregated* solver was used to run the simulation for an array of vehicle speeds, ranging from idle to high-speed conditions. The k-ε turbulence model was used with a hybrid all-y^+ treatment which uses blended wall functions that emulate the low-y^+ wall treatment for fine meshes, and the high-y^+ wall treatment for coarse meshes [27].
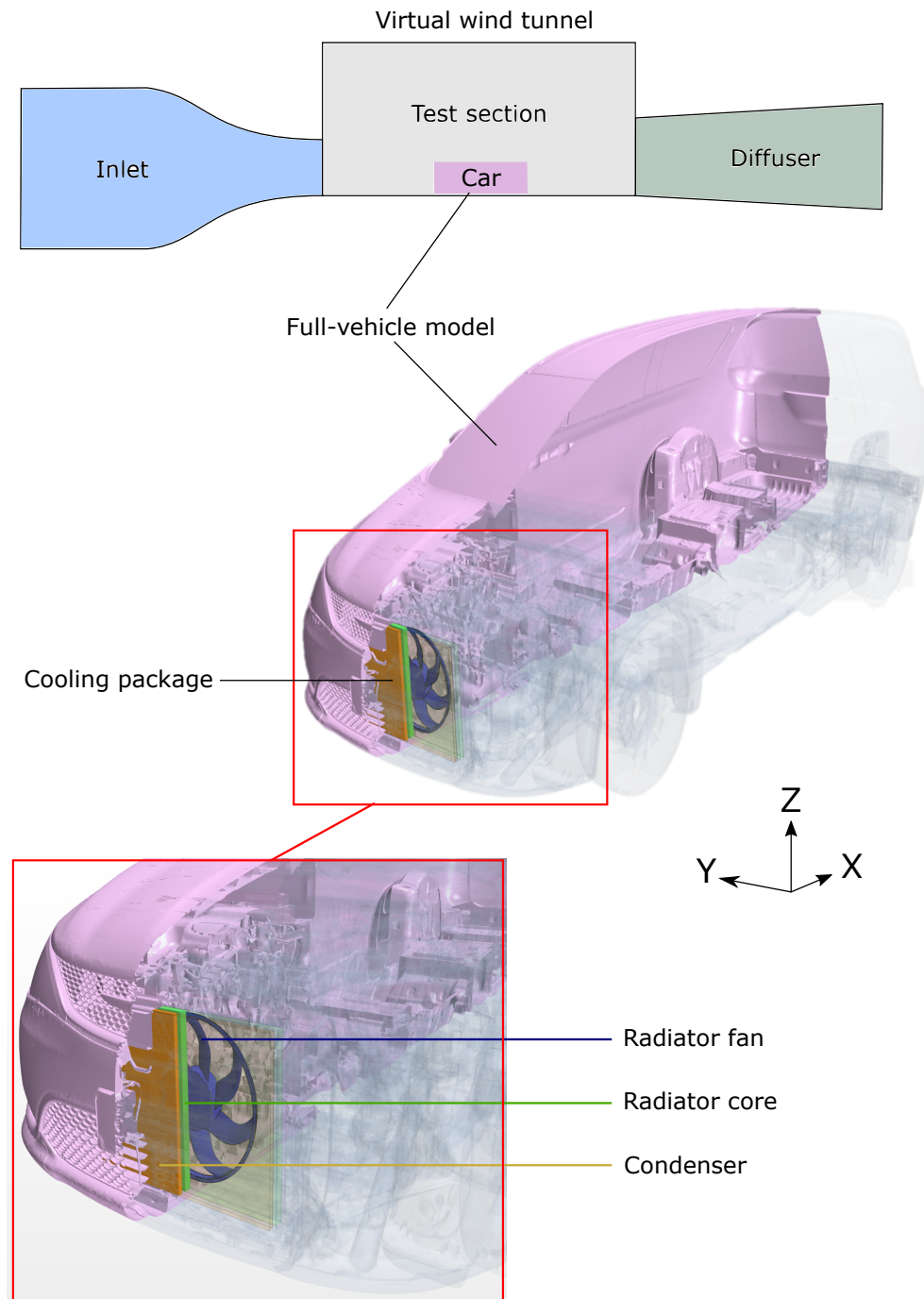
Figure 4.15: An illustration of the full vehicle with the real fan geometry placed in a virtual wind tunnel
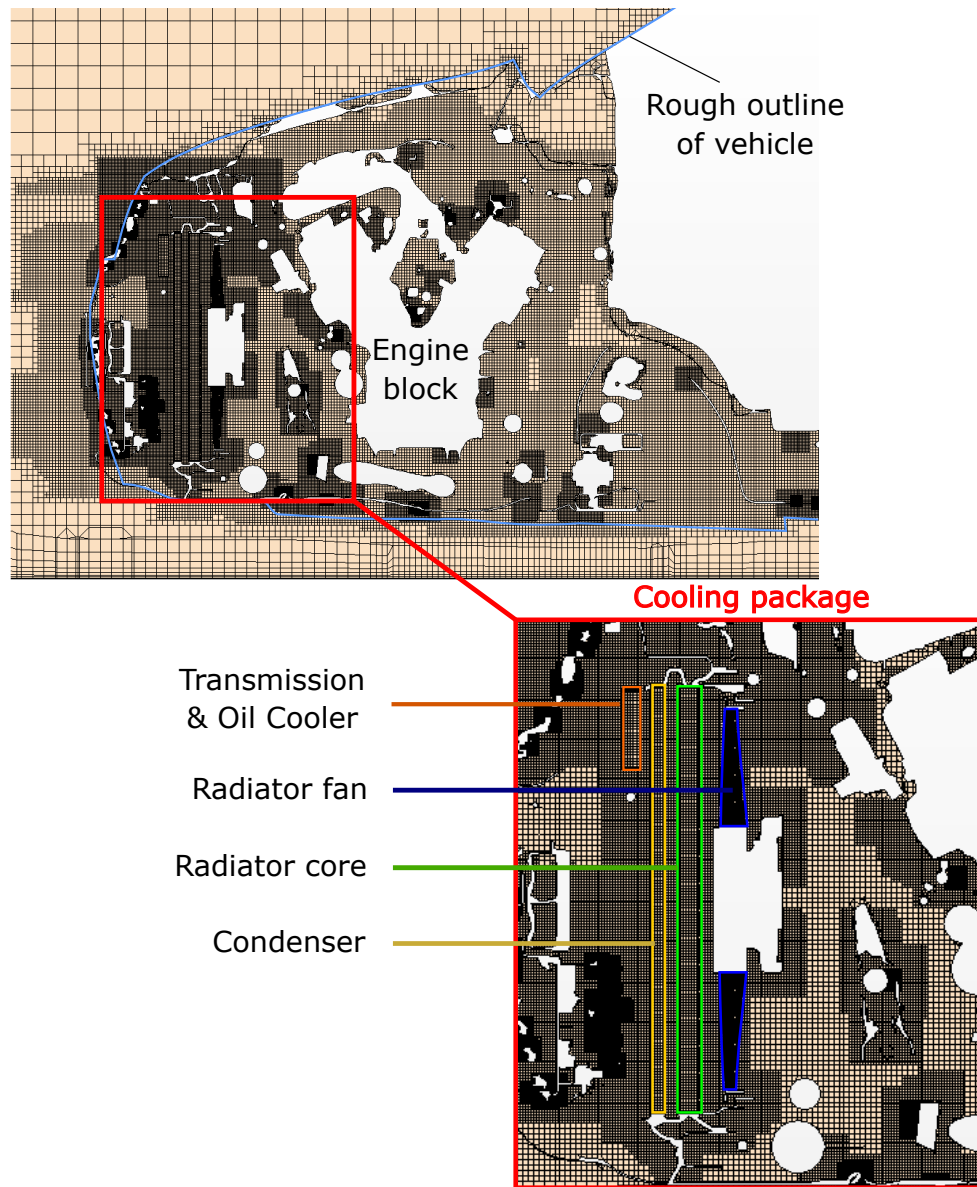
Figure 4.16: An illustration of the full vehicle trimmed mesh created using STAR-CCM+ [27]

4.6.2 Body Force Modeling

Hall's original body force formulation was introduced in the full vehicle setup in a similar fashion as described in Section 4.3 to introduce the source terms in the body force volume. The swept volume of the real blades is replaced by an isolated fluid volume to distinguish the body force region. The upstream and downstream

surfaces of the body force volume are simply defined as internal interfaces. The body force region does not have any concrete upstream/downstream boundary conditions, instead both the total pressure rise and the flow rate through the fan are a part of the solution for the full vehicle. To achieve the correct flow rate through the fan, it is important that the model predicts the correct total pressure rise. The rotational speed of the fan is constant for all simulations.

STAR-CCM+ [27] is only capable of performing a closest point interpolation for 3D scattered data using lookup tables[2]. Therefore, the blade camber normal distributions (needed for BFM calculations) are typically introduced using a table with a resolution at least as fine as the grid spacing present in the body force volume to ensure accuracy. However, the high density of cells created by the trimmed cell mesher makes it impractical to create a table with a finer resolution due to memory usage issues. Dodging this problem required the camber values to be first introduced to a coarser body force grid with a resolution of about 250,000 cells using an identical look-up table resolution[3]. The table contains the camber normal values defined at the exact cell centers of the coarser grid. Once the camber field is initialized on the coarse mesh, the grid can be successively refined to any resolution. After the refinement process, STAR-CCM+ [27] automatically maps the field from the coarse to the fine grid using a robust higher-order interpolation stencil. This ensures that all grid cells have accurately interpolated values of the camber normals without running into insufficient memory issues.

---

[2]The ability to map volume fields from lookup tables using a high-order interpolation routine is missing in Star-CCM+ and is considered to be a major drawback. The constraint of performing a closest-neighbour interpolation for the camber field requires the lookup table to have scattered data in all 3 dimensions (even though the camber normal values are a function of x and r only), and to have a resolution at least as fine as the grid spacing to ensure accuracy. In contrast, the open-source solver OPENFOAM v6 can be programmed to accurately interpolate volume fields from any resolution of a coarse scattered data set provided in the form of lookup tables as a function of two dimensions (x and r) only. See details in Chapter 2, Section 2.4.

[3]In contrast, implementation of this model in OPENFOAM v6 requires a much coarser lookup table resolution. For the automotive fan, a camber table resolution of 60 axial and 13 radial points was used, resulting in a table consisting of 780 data points only.

4.6.3 Calibrated Body Force Model and Comparison Metrics

The results obtained from Hall's original uncalibrated body force model are compared to a calibrated body force model approach currently used in the industry. This calibrated approach requires the specification of the fan performance data which was obtained using full unsteady sliding-mesh simulations of the fan in a virtual wind tunnel test bench for a range of fan mass flow rates. The details of the approach are outside the scope of this chapter. It is sufficient to mention that an identical full vehicle wind tunnel model setup was used to test the calibrated model for a range of vehicle speeds.

The fan model is responsible for yielding the mass flux distribution across the heat exchangers and the rest of the underhood flow paths. The performance of a fan model can be judged by observing how accurately it captures the volumetric flow rate passing through the radiator, hence we use this metric for assessing the accuracy of the calibrated and uncalibrated body force approaches against available experimental data.

4.6.4 Results

The simulations were run for a range of tunnel mass flow rates or vehicle speeds ranging from idle conditions up to a high speed of 100 mph. Figure 4.17 shows the volumetric flow rate exiting the radiator (non-dimensionalized by the fan design flow rate) as a function of a range of vehicle speeds. The fan curves are shown for the experimental tests, the full vehicle computations without the body force model (cooling due to ram air) and the two body force model approaches (cooling due to fan + ram air).

At idle conditions, the experiments yield a non-dimensionalized radiator airflow rate of about 0.7. The calibrated fan interface model under-predicts the volumetric
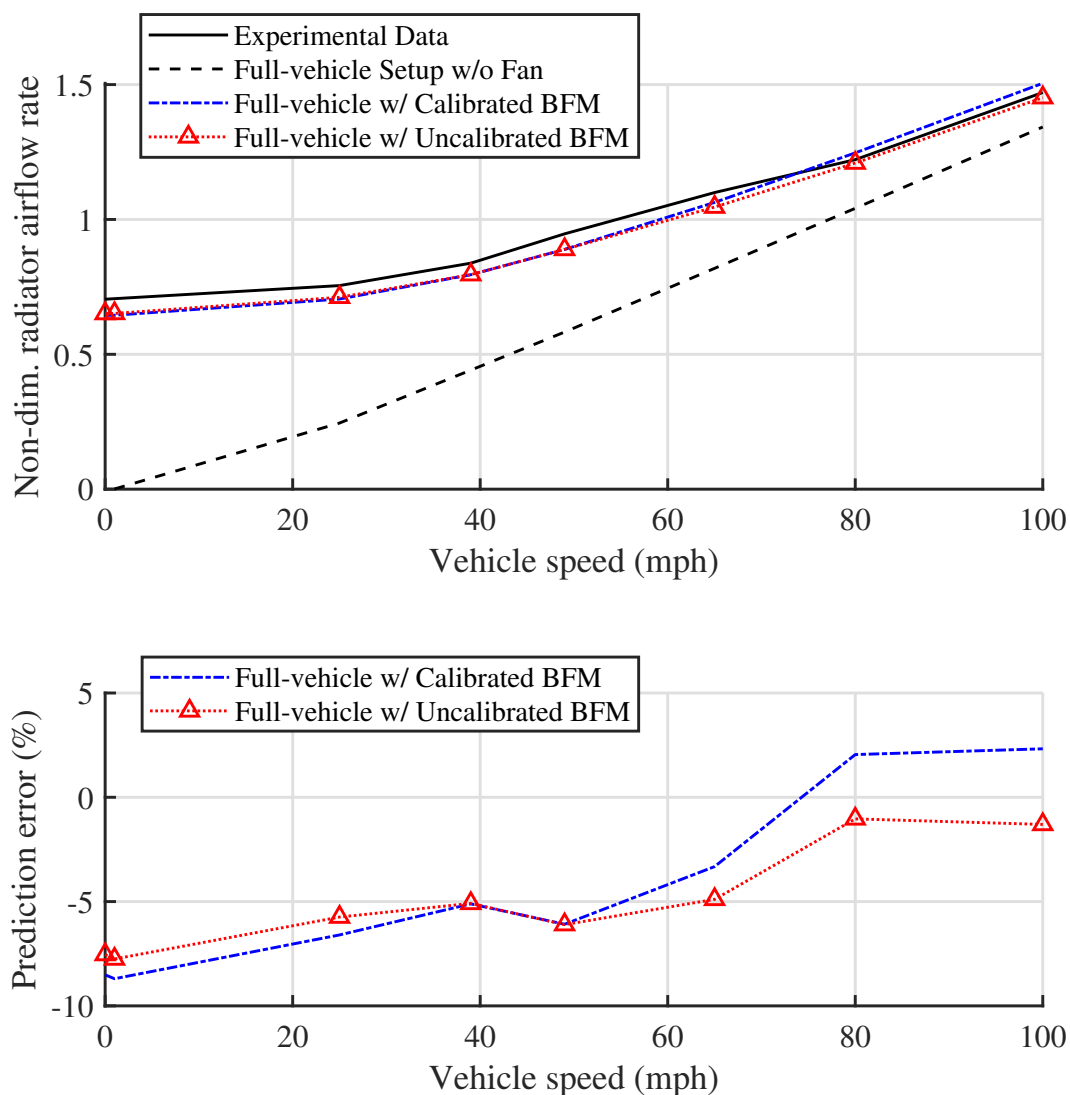
Figure 4.17: Fan performance data obtained from experiments, and full vehicle computational setup without fan, with calibrated body force model, and with uncalibrated body force model (top), and corresponding error for the body force models predictions compared to experimental data (bottom)

flow rate through the radiator by about 9% whereas Hall's model performs slightly better with an under-prediction error of 8%. For vehicle speeds ranging from 25 mph to 65 mph, the two models yield almost identical values of the flow rates. However, at higher vehicle speeds (80mph to 100 mph), the body force model performs significantly

better as it under-predicts the value just by 1%. On the other hand, the calibrated fan interface model overpredicts the volumetric flow rate through the radiator by about 2%. It is important to note that in a full aero-thermal simulation, the under-prediction of flow rate through the radiator would lead to the prediction of higher than actual maximum component temperatures. This is preferable since the under-prediction automatically adds a "safety margin" to the temperature limits for which the underhood installations have to be designed.

Figure 4.17 also shows the flow curve obtained for the case of a full vehicle operating without the fan, which is representative of the passive cooling that occurs due to the ram air effect generated by the motion of the vehicle. It is evident that at lower speeds, the fan is the major driver of airflow through the radiator and ram pressure only plays a minor role. At speeds higher than 40 mph, the fan only supplements the ram air which drives the majority of the airflow through the radiator.

Figure 4.18 shows contours of the velocity components obtained for the uncalibrated and the calibrated body force models on a vertical symmetry plane through the fan. The calibrated model predicts higher axial velocities, especially near the shroud, indicating a higher radial migration of the flow. An interesting feature to note is that the calibrated model exhibits high axial velocity "rings" both at the hub and the shroud whereas the uncalibrated model does not. The uncalibrated model seems to predict more realistic results as the nature of the fan is to cause outward (towards shroud) radial migration of flow (see axial velocity profile for bladed results in Figure 4.7). Moreover, Hall's body force model formulation takes all three velocity components into account, unlike the calibrated body force model. The flow fields just downstream of the fan on the y-cut show minor qualitative differences, however it does not seem to have any effect on the overall predicted air flow rate through the radiator.
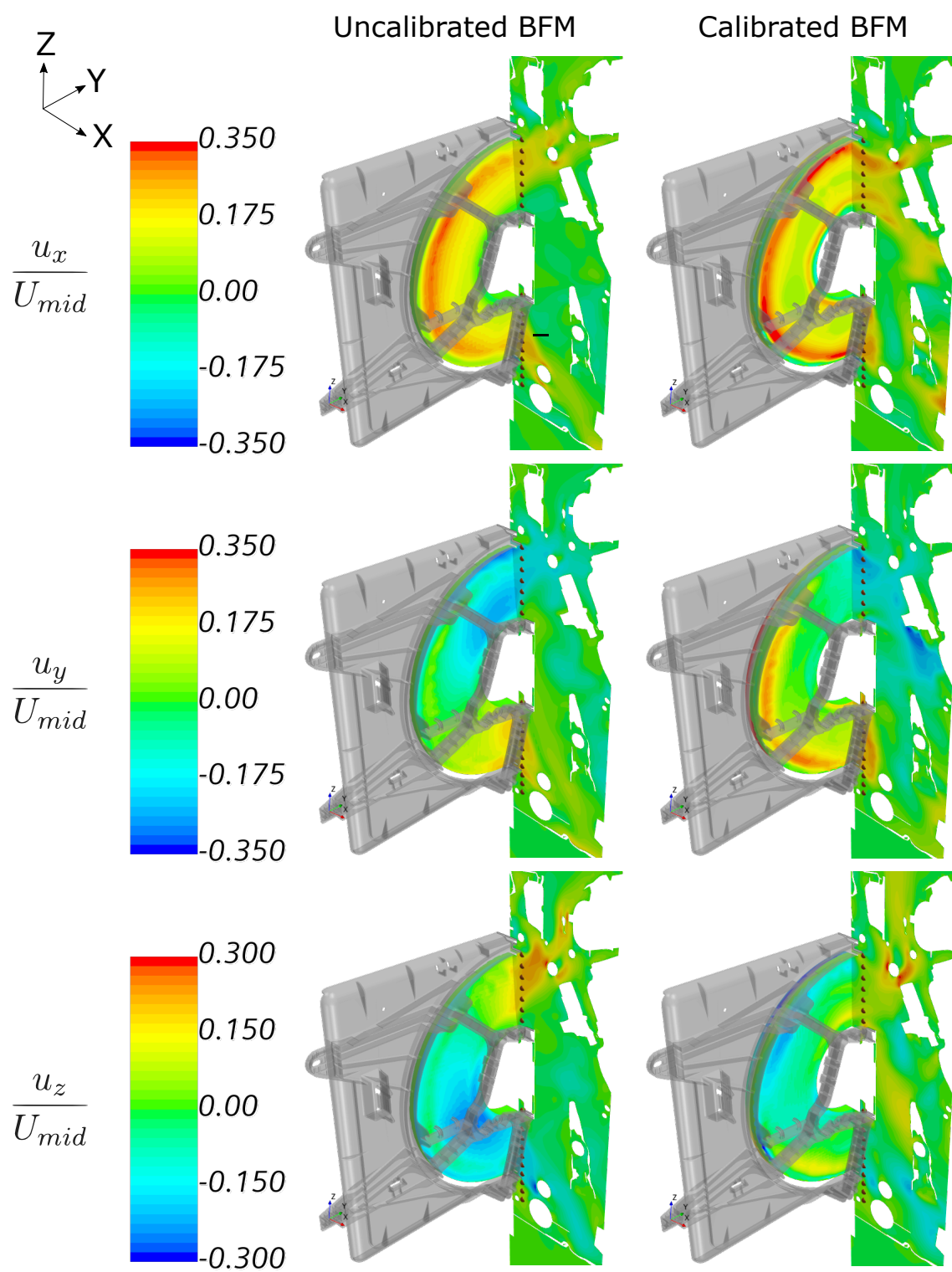
Figure 4.18: Velocity contours on a vertical symmetry plane through the fan along with probe locations for measurement plane 1 in Figure 4.19

To get a more detailed insight into the flow field variations exhibited by the two modeling approaches, the velocity components were extracted at different measurement plane locations just downstream of the fan as illustrated in Figure 4.19. Figures 4.20 - 4.23 show the absolute values of the velocity components extracted just downstream of the fan on the measurement locations indicated in Figure 4.19. The velocity component plots obtained from the two models show mostly similar qualitative trends, however there are many variations between the absolute values of the velocity components.
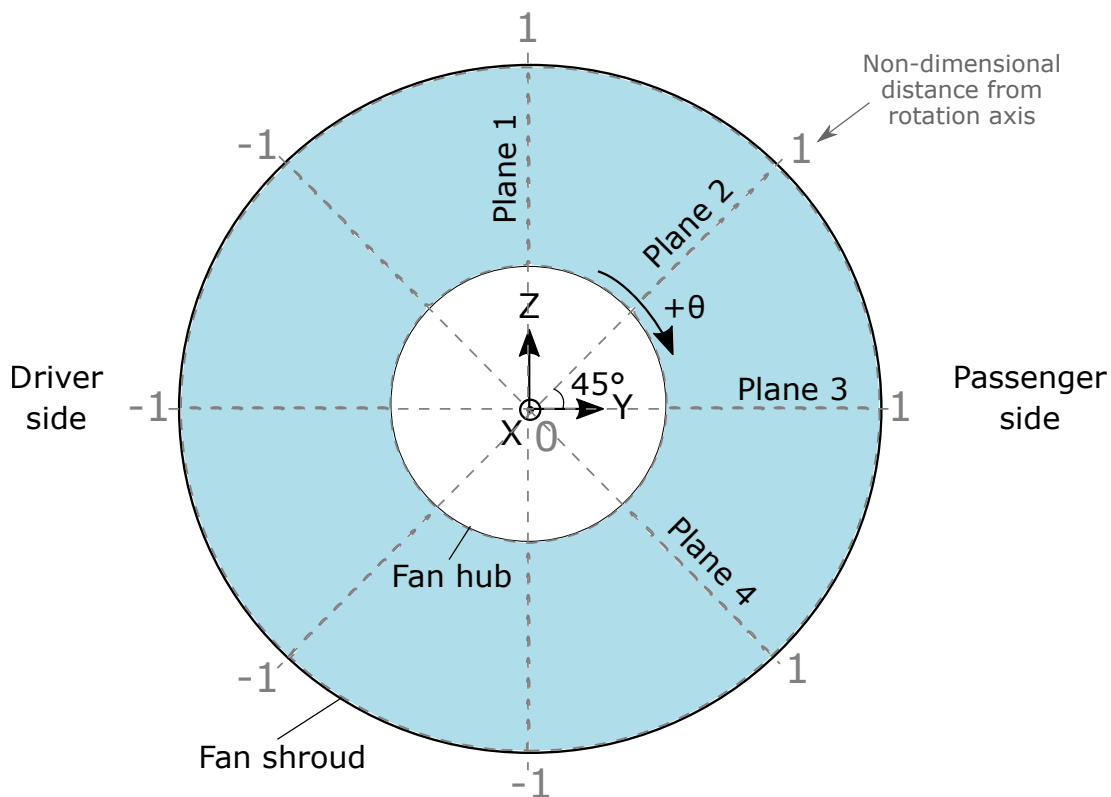
Figure 4.19: Measurements plane locations for data extraction just downstream of the fan (looking towards the front from the back of the car)
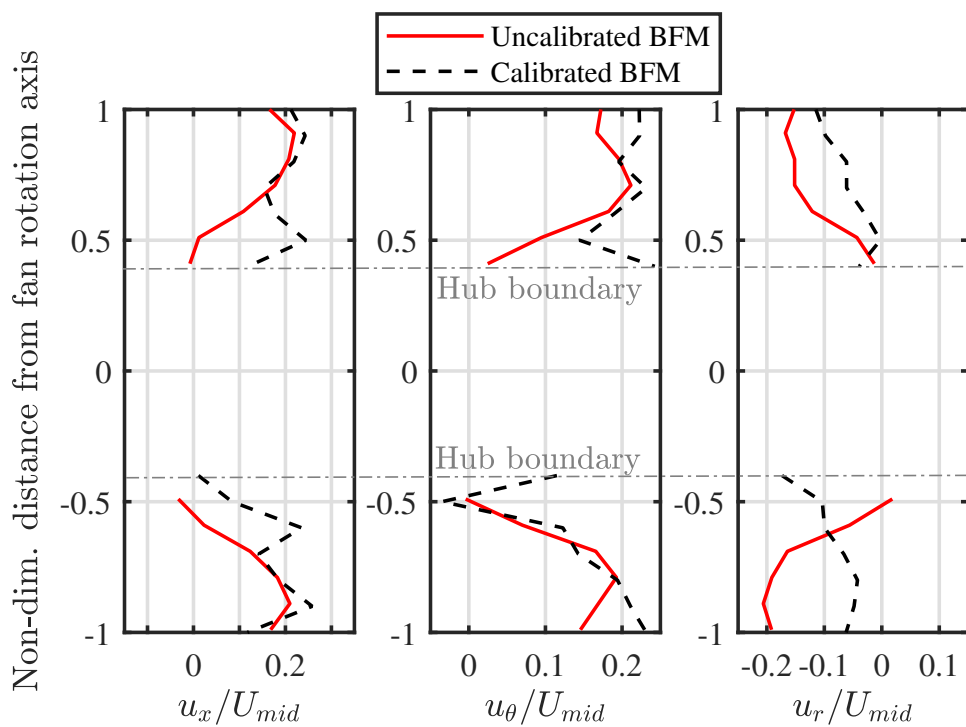
Figure 4.20: Velocity components obtained for measurement plane 1
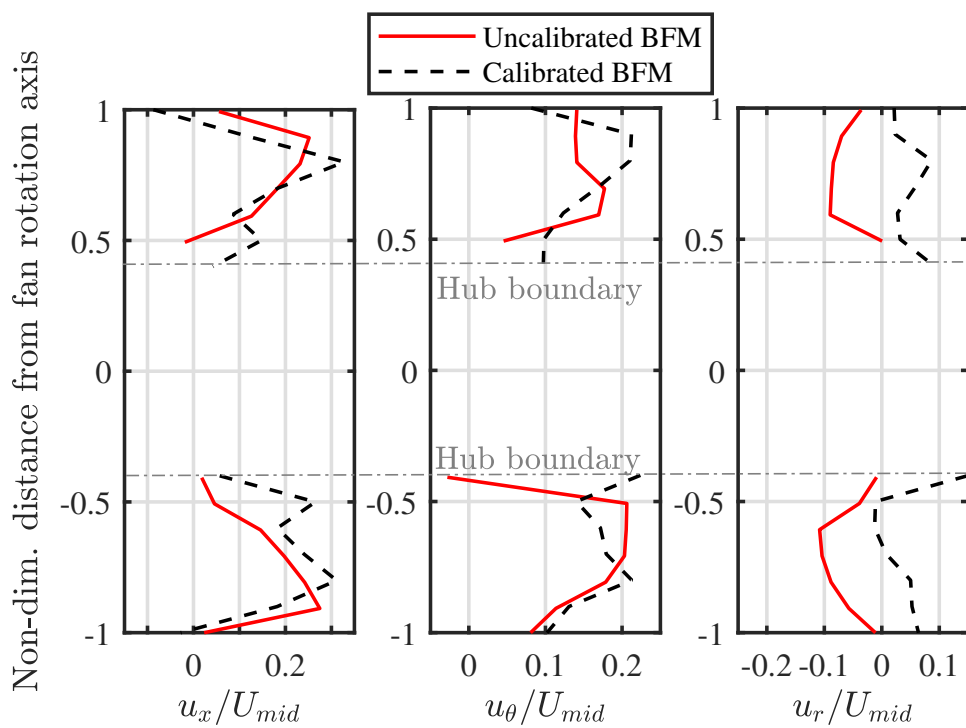
Figure 4.21: Velocity components obtained for measurement plane 2
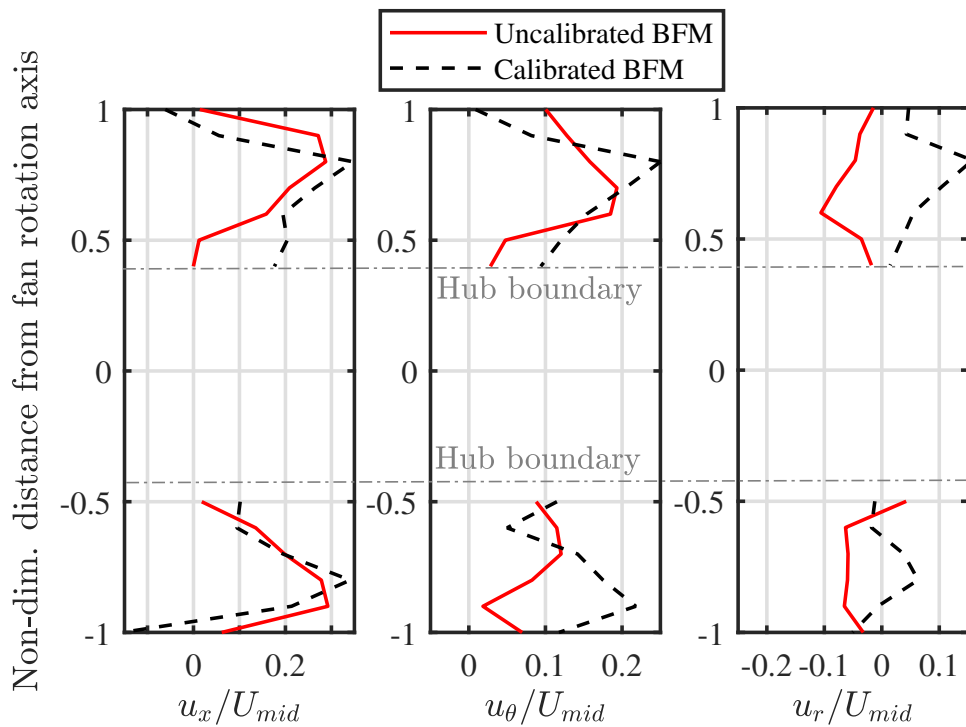
Figure 4.22: Velocity components obtained for measurement plane 3
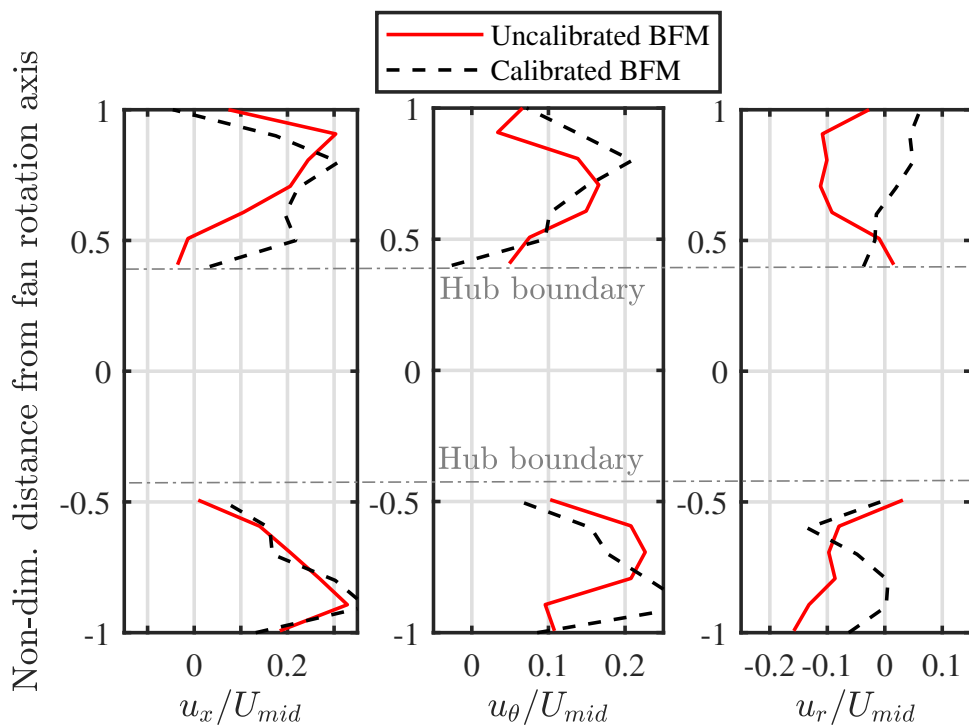
Figure 4.23: Velocity components obtained for measurement plane 4

4.7 Summary and Conclusions

The automotive fan is a critical component of the cooling module, providing the majority of the cooling airflow over the heat exchangers and to underbody components at low speed, idle, and key-off conditions. Accurately predicting the performance of the automotive cooling fan is critical for sizing heat exchangers and ensuring that underhood and underbody components remain below target temperatures. This is normally done with computational fluid dynamics, but in a full vehicle simulation it is impractical to include the details of the rotating fan blades. Thus, simplified body force models which capture the fan behavior are employed. Industrial practice is to calibrate fan models based on experiments or higher-fidelity simulations, but this slows down the design process and is expensive. This work makes use of a purely analytical body force modeling approach which eliminates the calibration step, requiring only fan geometry information and no a-priori performance data.

The fan model was first tested for uniform inflow cases and the performance is assessed against computations including the blades. The model was then applied to simulations of the flow around and through an entire vehicle at a variety of speeds. The model predicts the flow rate through the radiator to within 8% of the experimentally-measured value at idle. At high vehicle speed, the accuracy improves to 1%. The uncalibrated model has equal or better accuracy in predicting the flow rate compared to the current best-practice calibrated fan modeling techniques used in the industry. The impact of the findings is a significant reduction in the overall effort, time, and cost involved in simulating under-hood and underbody flows.

References

[1] Randi Franzke and Simone Sebben. Validation of different fan modelling techniques in computational fluid dynamics. In *Proceedings of the 21st Australasian Fluid Mechanics Conference, Adelaide, Australia*, pages 10–13, 2018.

[2] Palak Saini and Jeff Defoe. The effect of blade count on body force model performance for axial fans. In *Turbo Expo: Power for Land, Sea, and Air*, 2020.

[3] M Kornhaas, K Rädecke1, I Futterer, F Werner, C Ribes, and O Ferney. Aspects of fan modeling for underhood thermal management CFD. In *12th FKFS Conference, Munich, Stuttgart*.

[4] Peter Gullberg, Lennart Löfdahl, Steven Adelman, and Peter Nilsson. An investigation and correction method of stationary fan CFD MRF simulations. Technical report, SAE Technical Paper, 2009.

[5] Peter Gullberg, Lennart Löfdahl, Peter Nilsson, and Steven Adelman. Continued study of the error and consistency of fan CFD MRF models. Technical report, SAE Technical Paper, 2010.

[6] Peter Gullberg, Peter Nilsson, et al. Fan modeling in CFD using MRF model for under hood purposes. In *Proceedings of the ASME-JSME-KSME 2011 Joint Fluids Engineering Conference*, pages 931–942. ASME, 2011. paper number AJK2011-23020.

[7] Yuji Kobayashi, Itsuhei Kohri, and Yukio Matsushima. Study of influence of MRF method on the prediction of the engine cooling fan performance. In *Proceedings of the 2011 SAE 2011 World Congress & Exhibition*. SAE, 2011. SAE technical paper 2011-01-0648.

[8] Shankar Natarajan, Aditya Mulemane, and Pradip Dube. Underhood and underbody studies in a full vehicle model using different approaches to model fan and predict recirculation. In *Proceedings of the 2008 SAE World Congress & Exhibition*. SAE, 2008. SAE technical paper 2008-01-1173.

[9] Hak Jun Kim and Charn-Jung Kim. A numerical analysis for the cooling module related to automobile air-conditioning system. *Applied Thermal Engineering*, 28(14-15):1896–1905, 2008.

[10] CJ Meyer and DG Kröger. Numerical simulation of the flow field in the vicinity of an axial flow fan. *International Journal for Numerical Methods in Fluids*, 36(8):947–969, 2001.

[11] Constantine P Tzanos and Tai-Hsin Chien. A simple fan model for underhood thermal management analyses. Technical report, SAE Technical Paper, 2002.

[12] Ali Sahili, Bashar Zogheib, and Ronald M Barron. 3-d modeling of axial fans. *Applied Mathematics*, 4(4):632–651, 2013.

[13] W. G. Joo and T. P. Hynes. The application of actuator disks to calculations of the flow in turbofan installations. *Journal of Turbomachinery*, 119(4):733–741, Jan 1997.

[14] W. R. Hawthorne, N. A. Mitchell, J. E. Mccune, and C. S. Tan. Nonaxisymmetric flow through annular actuator disks: Inlet distortion problem. *Journal of Engineering for Power*, 100(4):604–617, Jan 1978.

[15] SJ Van der Spuy, FN Le Roux, et al. The simulation of an axial flow fan performance curve at low flow rates. In *ASME 2011 Turbo Expo: Turbine Technical Conference and Exposition*, pages 425–434. American Society of Mechanical Engineers Digital Collection, 2011.

[16] Sybrand J Van der Spuy, TW Von Backström, and Detlev G Kröger. An evaluation of simplified methods to model the performance of axial flow fan arrays. *R & D Journal of the South African Institution of Mechanical Engineering*, 26:12–20, 2010.

[17] DK Hall, EM Greitzer, and CS Tan. Analysis of fan stage conceptual design attributes for boundary layer ingestion. *J. Turbomach.*, 139(7):071012, 2017.

[18] JJ Defoe, M Etemadi, and DK Hall. Fan performance scaling with inlet distortions. *J. Turbomach.*, 140(7):071009, 2018.

[19] FRANK E Marble. Three-dimensional flow in turbomachines, 1964.

[20] Andreas Peters, Zoltán S Spakovszky, Wesley K Lord, and Becky Rose. Ultrashort nacelles for low fan pressure ratio propulsors. *J. Turbomach.*, 137(2):021001, 2015.

[21] Y Gong, CS Tan, KA Gordon, and EM Greitzer. A computational model for short wavelength stall inception and development in multi-stage compressors. *J. Turbomach.*, 121:726–734, 1999.

[22] Emmanuel Benichou, Guillaume Dufour, Yannick Bousquet, Nicolas Binder, Aurélie Ortolan, and Xavier Carbonneau. Body force modeling of the aerodynamics of a low-speed fan under distorted inflow. *Int. J. Turbomach. Propuls. Power*, 4(3), 2019.

[23] Mahmoud Khaled, Mohamad Ramadan, Hicham El-Hage, Ahmed Elmarakbi, Fabien Harambat, and Hassan Peerhossaini. Review of underhood aerothermal management: Towards vehicle simplified models. *Applied Thermal Engineering*, 73(1):842–858, 2014.

[24] William Thollet, Guillaume Dufour, Xavier Carbonneau, and Florian Blanc. Body-force modeling for aerodynamic analysis of air intake–fan interactions. *International Journal of Numerical Methods for Heat & Fluid Flow*, 2016.

[25] Benjamin Godard, Edouard De Jaeghere, and Nicolas Gourdain. Efficient design investigation of a turbofan in distorted inlet conditions. In *Turbo Expo: Power for Land, Sea, and Air*, volume 58554, page V02AT39A011. American Society of Mechanical Engineers, 2019.

[26] The OpenFOAM Foundation. OpenFOAM v6, 2019.

[27] Simcenter STAR-CCM+ user guide v13. 04. *Siemens PLM*, 2018.

[28] David K Hall. *Analysis of civil aircraft propulsors with boundary layer ingestion.* PhD thesis, PhD Thesis, MIT, 2015.

[29] Pointwise. *Pointwise v18.3R1 User's Manual.* Pointwise, Forth Worth, TX, 2019.

Chapter 5

Summary, Contributions and Future Work

In this thesis, an existing uncalibrated simplified fan modeling approach is described which only requires details of the fan geometry to simulate fan behaviour at a low computational cost. The model is used to mimic automotive radiator fans for the study of cooling system behavior in a full vehicle. In this chapter, the three papers which comprise the thesis are outlined with a description of how they relate to one another. Subsequently, the key contributions and technical recommendations for future work are discussed.

5.1 Concluding Remarks

Body force models have long been used in the aerospace as well as the automotive communities as a low cost alternative option for modeling turbomachinery behavior. In the aerospace domain, there are varied analytical approaches available to model turbomachinery but the applications are limited to aero-specific machines such as propellers, helicopter rotors, and powerful high-blade count fans and compressors. On the other hand, the automotive industry has a long history of using body force models for low blade count automotive radiator fans but none of the approaches are purely analytical; all fan models require some kind of expensive and time-consuming calibration process to yield correct results. Clearly, there is a literature gap between the two domains and little work has been done to apply the analytical aero-engine modelling expertise to automotive fan applications. Bridging this gap was the motivation behind the current work. An existing, purely analytical body force based

approach from aerospace literature is used to model automotive radiator fans in this work.

Chapter 2 describes the basis of the framework used to implement the model in an open-source software package (which offers cost savings due to the lack of licensing costs) and the related numerical details. It serves to detail the implementation process of a general volumetric source term based turbomachinery model, a capability which is otherwise largely absent in general-use open-source CFD codes and whose details are mostly undocumented. The chapter describes the model implementation framework in the open-source software OPENFOAM v6 and assesses its performance against experiments, and commercial codes such as STAR-CCM+ and ANSYS CFX. OPENFOAM v6 is found to be a suitable solver for implementing general body force models and yields results as good as commercial CFD solvers while offering the most flexibility.

Chapter 3 addresses the preliminary performance assessment of this simplified model for a range of flow coefficients and blade counts, and dives deep into the model-captured flow field details to gain insights into its behavior. This chapter pushes the model to its breaking limits and to regimes in which it was thought it ought not to work. The model performance was assessed against high-fidelity bladed simulations for the cases of clean uniform inflow, a boundary-layer ingestion (BLI) type inlet distortion, and a canonical underhood flow geometry. Overall, the model was able to capture the general turbomachine behavior even for low blade counts, for which the accuracy of the model actually improved. The model under-predicted the fan work input for uniform inflow cases, however it was able to produce a smooth distortion response even at high reduced frequencies for the non-uniform inflow cases, except when extremely low blade counts (such as 2) were applied.

Chapter 4 attempts to improve the model performance via additional modifications, and then assesses the performance of the original model in simulations of airflow

in and around a full vehicle. The calibration-free model is found to perform with a comparable or even better accuracy than the current calibrated state-of-the-art fan modeling techniques employed by the automotive community. At low speeds, the model is found to predict the radiator airflow to within an accuracy of 8% of the experimental value. At higher vehicle speeds, the accuracy improves to 1%. The chapter clearly demonstrates the suitability of the model for automotive applications and it's comparable robustness to current best-practice fan modeling techniques.

5.2 Contributions

This thesis makes several contributions:

- development of open-source CFD expertise for implementing body force based turbomachinery models,

- a comprehensive insight into the impact of low blade counts on body force model performance in general,

- successful transfer of analytical aero-engine modelling expertise to a completely different application of automotive under hood air flows, and

- implementation of a calibration-free fan model for design of automotive cooling systems; this has the potential to reduce fan design prototypes in the very early stages of the vehicle development program besides offering experimental cost savings, and facilitating a reliable, rapid design and aerothermal analysis process for vehicle cooling systems.

5.3 Technical Recommendations and Future Work

There are a number of technical improvements that the author sees as beneficial for improving the open-source implementation of the model. The comments are mostly

related to the structure of the code itself. Besides this, a number of suggestions for further research are given.

5.3.1 Technical Improvements for Open-source Implementation

- **Lower memory usage:** The code currently creates multiple copies of `camber` field for each iteration as this is the only way that the author found to allow `fvOptions` easy access to the camber field. This can lead to large memory usage, especially for high grid count simulations where the turbomachinery is just a small part of the entire domain. The code implementation should be structured such that the `camber` field is read from a single file which is not copied for every iteration.

- **OpenFOAM v8 compatibility:** OPENFOAM v8 is the latest version of the open-source software. The code needs to be tested for this version to make sure the implementation works correctly.

- **Compressible solver implementation:** The current model implementation is a modified version of the incompressible, steady-state, `simpleFoam` solver which is only coded to include the momentum source terms. The implementation has to be extended to the compressible version of the solver, `rhoSimpleFoam`, which requires addition of both momentum as well as energy source terms.

5.3.2 Future Research Suggestions

1. **Thermal protection simulations for full vehicle:** The ultimate purpose of the body force model is to predict the correct air flux as well as temperature distributions throughout the underhood to ensure that the cooling system will allow optimum engine operation. Complete aerothermal simulations are an important test for the ultimate usability of Hall's model in the design of cooling systems (current incompressible flow analysis only lends aerodynamic insights). Further insights into the model's accuracy can be gained by comparing condenser inflow air temperature, fan blast temperature (radiator out temperature), and temperatures of components in the underhood to experimental data as well as those predicted by current best-practice calibrated models.

2. **Validation of multiple-reference frame (MRF) simulations against full unsteady RANS simulations:** The fan characteristic curves obtained from the multiple-reference frame simulations from the two solvers OPENFOAM v6 and STAR-CCM+ had slight differences. Since the result of MRF computations can be affected by user-specific and solver-specific methodology, the MRF implementations should be validated against full URANS simulations in the two solvers. For cases of uniform flow, both MRF and URANS simulations should yield identical results in both solvers for rotor-alone computations.

3. **Sliding-mesh simulations for full vehicle:** Sliding-mesh URANS simulations for a full-vehicle are rarely performed due to their high computational cost and long simulation times. However, they could lend insights into the behavior of the body force model for low blade counts, and could be a future research direction.

4. **Use of a low Reynolds number correlation for calculation of skin friction coefficient in the loss model:** The loss model described in Section 4.2 has shown promising results for aircraft engine fans which typically operate in the high Reynolds number, turbulent flow regime. Therefore, the friction coefficient, C_f, is based on an empirical flat plate friction coefficient formulation for turbulent flows. However, the low Reynolds numbers seen in automotive underhood environment might cause portions of the blade to operate in the laminar or transitional regime. The friction coefficient formulation needs to be adjusted accordingly to take into account the lower Reynolds number skin friction correlation meant for laminar/transitional flows.

5. **Systematic study to assess the non-linear variations in the blade loading force at low solidities:** Figure 3.11 indicated two different modes of operation for the body force model: a) a high blade count mode, where the accuracy of the model predictions is not a function of the solidity of the fan (hence we see a constant offset between the MRF and the body force predictions above a blade count of 11), b) a low blade count mode, where the accuracy of the model predictions changes with the blade count or the solidity of the fan. This might suggest that at lower blade counts, the low solidity effects need to be accounted for through a non-linear formulation between the blade loading force, $\vec{f_n}$, and the solidity, $2\pi r/B$.

Appendix A

OpenFOAM Source Code

This section details the entire underlying code used to implement Hall's body force model in the open-source CFD package OpenFOAM.

A.1 `fsimpleFoam` solver

A modified version of the simpleFoam solver was compiled under the name `fsimpleFoam`. The files used to compile the modified solver application are listed in a directory structure in Figure A.1.
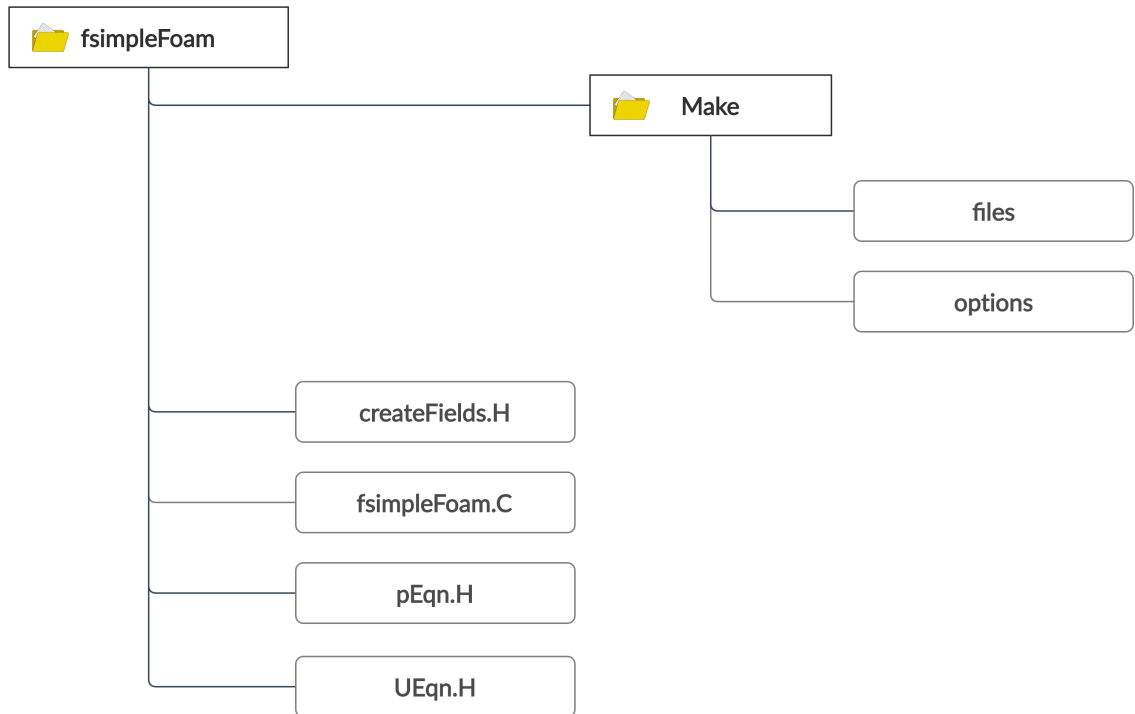
Figure A.1: Directory structure for the `fsimpleFoam` solver application before compilation

For creating the `fsimpleFoam` solver, the `simpleFoam` solver application files were directly copied from the source code. The file `simpleFoam.C` was simply renamed as `fsimpleFoam.C` without any modifications to the file contents. The `createFields.H` was modified for the inclusion of additional fields to hold the blade geometry information `camber` and the body force vector `F`. The `Make/files` was also updated. The contents of the modified files are listed below.

1. `createFields.H`

```
Info << "Reading field p\n" << endl;
volScalarField p
(
IOobject
(
"p",
runTime.timeName(),
mesh,
IOobject::MUST_READ,
IOobject::AUTO_WRITE
),
mesh
);

Info << "Reading field U\n" << endl;
volVectorField U
(
IOobject
(
"U",
runTime.timeName(),
mesh,
IOobject::MUST_READ,
IOobject::AUTO_WRITE
```

```
),

mesh

);


Info<< "Reading field F\n" << endl;

volVectorField F

(

IOobject

(

"F",

runTime.timeName(),

mesh,

IOobject::MUST_READ,

IOobject::AUTO_WRITE

),

mesh

);


Info<< "Reading field camber\n" << endl;

volVectorField camber

(

IOobject

(

"camber",

runTime.timeName(),

mesh,

IOobject::MUST_READ,

IOobject::AUTO_WRITE

),

mesh

);
```

```
#include "createPhi.H"


label pRefCell = 0;
scalar pRefValue = 0.0;
setRefCell(p, simple.dict(), pRefCell, pRefValue);
mesh.setFluxRequired(p.name());


singlePhaseTransportModel laminarTransport(U, phi);


autoPtr<incompressible::turbulenceModel> turbulence
(
incompressible::turbulenceModel::New(U, phi, laminarTransport)
);


#include "createMRF.H"
#include "createFvOptions.H"
```

2. Make/options

```
fsimpleFoam.C


EXE = $(FOAM_USER_APPBIN)/fsimpleFoam
```

A.2 Example of a Body Force Case Setup

Figure A.2 shows the directory structure of an example case setup for a body force model implementation. The contents of the `system/fvOptions`, `0/camber` and `nx_data` files are presented in the subsequent pages.
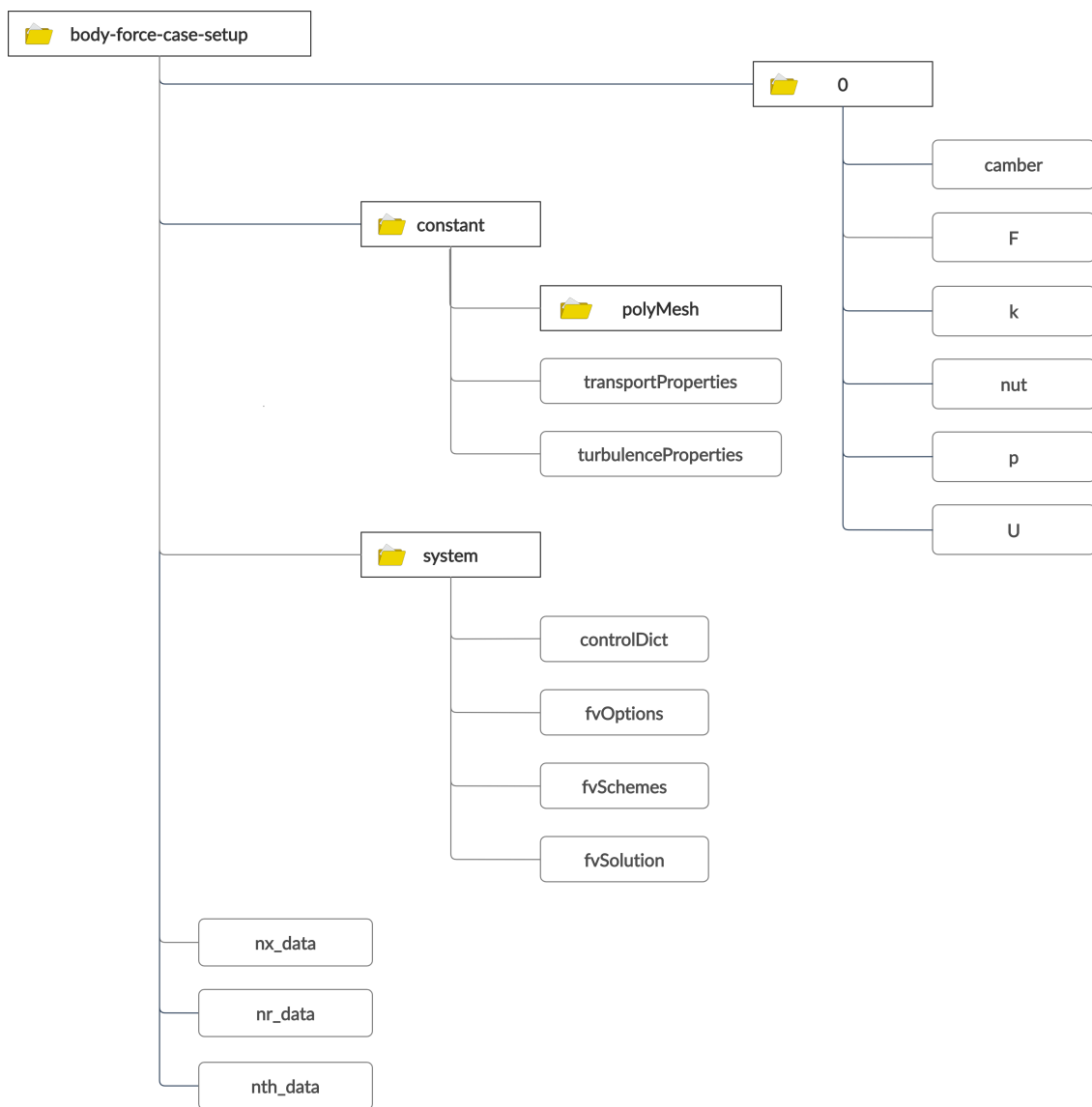
Figure A.2: Directory structure for a body force case setup showing essential files

1. 0/camber

```
/*--------------------------------*- C++

    -*----------------------------------*\

========                    |

\\      /   F ield   | OpenFOAM: The Open Source CFD Toolbox

\\    /    O peration     | Website:  https://openfoam.org

\\  /     A nd            | Version:  6

\\/      M anipulation   |

\*---------------------------------------*/

FoamFile

{

version     2.0;

format      ascii;

class       volVectorField;

location    "0";

object      camber;

}

// * * * * * * * * * * * * * * * * * * * //


dimensions      [0 0 0 0 0 0 0];


internalField   #codeStream


{


codeInclude

#{

#include "fvCFD.H"

#include </usr/include/CGAL/

    Exact_predicates_inexact_constructions_kernel.h>

#include </usr/include/CGAL/Delaunay_triangulation_2.h>

#include </usr/include/CGAL/Interpolation_traits_2.h>
```

```
#include </usr/include/CGAL/natural_neighbor_coordinates_2.h>

#include </usr/include/CGAL/interpolation_functions.h>

#include <IFstream.H>

#include <OFstream.H>

#include <ctime>

#include "clock.H"

#include "string.H"

#include <sstream>

#include <iomanip>

#};


codeOptions
#{
-I$(LIB_SRC)/finiteVolume/lnInclude \

-I$(LIB_SRC)/meshTools/lnInclude

#};


codeLibs
#{
-lmeshTools \

-lfiniteVolume

#};


code
#{



Pout<< " \n Calculating camber normals.... \n" << endl;


const IOdictionary& d = static_cast<const IOdictionary&>(dict);

const fvMesh& mesh = refCast<const fvMesh>(d.db());

vectorField camber(mesh.nCells(), vector(0,0,0));
```

```cpp
scalar x,y,z,RADIUS, NX, NR, NTH;


typedef CGAL::Exact_predicates_inexact_constructions_kernel
    K;
typedef CGAL::Delaunay_triangulation_2<K>
    Delaunay_triangulation;
typedef K::FT
    Coord_type;
typedef K::Point_2
    Point;
typedef std::map<Point, Coord_type, K::Less_xy_2>
    Coord_map;
typedef CGAL::Data_access<Coord_map>
    Value_access;
typedef std::vector<std::pair<Point, Coord_type>>
    C;


Delaunay_triangulation Tnx, Tnth, Tnr;                            //
    Holds the points
Coord_map value_nx, value_nth, value_nr;                          //
    Holds the points and their known values
List<vector> nx_data, nth_data, nr_data;
IFstream nx("nx_data");
nx  >> nx_data;
IFstream nth("nth_data");
nth  >> nth_data;
IFstream nr("nr_data");
nr  >> nr_data;


forAll(nx_data, a)
{
K::Point_2 px(nx_data[a][0], nx_data[a][1]);
```

```
Tnx.insert(px);
value_nx.insert(std::make_pair(px, nx_data[a][2]));
}


forAll(nth_data, b)
{
K::Point_2 pth(nth_data[b][0], nth_data[b][1]);
Tnth.insert(pth);
value_nth.insert(std::make_pair(pth, nth_data[b][2]));
}


forAll(nr_data, c)
{
K::Point_2 pr(nr_data[c][0], nr_data[c][1]);
Tnr.insert(pr);
value_nr.insert(std::make_pair(pr, nr_data[c][2]));
}



forAll(camber, i)
{
x = mesh.C()[i][0];
y = mesh.C()[i][1];
z = mesh.C()[i][2];
RADIUS = sqrt(y*y + z*z);


K::Point_2 p(x, RADIUS);
C coords_nx, coords_nth, coords_nr;


Coord_type norm_nx  = CGAL::natural_neighbor_coordinates_2(Tnx ,
    p, std::back_inserter(coords_nx )).second;
```

```cpp
Coord_type norm_nth = CGAL::natural_neighbor_coordinates_2(Tnth,
     p, std::back_inserter(coords_nth)).second;
Coord_type norm_nr  = CGAL::natural_neighbor_coordinates_2(Tnr ,
     p, std::back_inserter(coords_nr )).second;


Coord_type res_nx   =  CGAL::linear_interpolation(coords_nx.
    begin() , coords_nx.end() , norm_nx , Value_access(value_nx
    ));
Coord_type res_nth  =  CGAL::linear_interpolation(coords_nth.
    begin(), coords_nth.end(), norm_nth, Value_access(value_nth)
    );
Coord_type res_nr   =  CGAL::linear_interpolation(coords_nr.
    begin() , coords_nr.end() , norm_nr , Value_access(value_nr
    ));


NX  = res_nx;
NTH = res_nth;
NR  = res_nr;


camber[i] = vector(NX, NR, NTH);


}


camber.writeEntry("", os);


Pout<< " \n Interpolation  done. \n" << endl;
#};


};


boundaryField
{
```

```
fanwalls
{
type            slip;
}
passagewalls
{
type            slip;
}
inlet
{
type            fixedValue;
value           uniform (0 0 0);
}
outlet
{
type            zeroGradient;
}


#includeEtc "caseDicts/setConstraintTypes"
}


// *************************** //
```

2. `system/fvOptions`

```
/*--------------------------------*- C++

    -*--------------------------------*\
|  =========                 |


                                          |
|  \\      /  F ield    | OpenFOAM: The Open Source CFD Toolbox
              |
|   \\    /   O peration     | Version:  5

                                  |
|    \\  /    A nd          | Web:      www.OpenFOAM.org

                        |
|     \\/     M anipulation  |


                                          |
\*--------------------------------------*/
FoamFile
{
version     2.0;
format      ascii;
class       dictionary;
location    "constant";
object      fvOptions;
}
// * * * * * * * * * * * * * * * * * * * * * * * * * //


rotor
{
type            vectorCodedSource;
active          yes;
name            bodyForceRotor;
vectorCodedSourceCoeffs
{
selectionMode       cellZone; //cellSet;
```

```
// cellSet                              Rotor-cells;
cellZone                               fan-cells;
fields              (U);
codeInclude
#{
// #include </cvmfs/soft.computecanada.ca/easybuild/software
    /2017/avx2/Compiler/intel2016.4/cgal/4.9/include/CGAL/
    Exact_predicates_inexact_constructions_kernel.h>
// #include </cvmfs/soft.computecanada.ca/easybuild/software
    /2017/avx2/Compiler/intel2016.4/cgal/4.9/include/CGAL/
    Delaunay_triangulation_2.h>
// #include </cvmfs/soft.computecanada.ca/easybuild/software
    /2017/avx2/Compiler/intel2016.4/cgal/4.9/include/CGAL/
    Interpolation_traits_2.h>
// #include </cvmfs/soft.computecanada.ca/easybuild/software
    /2017/avx2/Compiler/intel2016.4/cgal/4.9/include/CGAL/
    natural_neighbor_coordinates_2.h>
// #include </cvmfs/soft.computecanada.ca/easybuild/software
    /2017/avx2/Compiler/intel2016.4/cgal/4.9/include/CGAL/
    interpolation_functions.h>
#include </usr/include/CGAL/
    Exact_predicates_inexact_constructions_kernel.h>
#include </usr/include/CGAL/Delaunay_triangulation_2.h>
#include </usr/include/CGAL/Interpolation_traits_2.h>
#include </usr/include/CGAL/natural_neighbor_coordinates_2.h>
#include </usr/include/CGAL/interpolation_functions.h>
#include <IFstream.H>
#include <OFstream.H>
#};
codeCorrect
#{
//Pout<< "**codeCorrect**" << endl;
```

```cpp
#};
codeAddSup
#{
label                    zoneID  = mesh_.cellZones().findZoneID("
    fan-cells");
volVectorField   F       = mesh_.lookupObject<volVectorField>("F"
    );
const labelList&               cells   = mesh_.cellZones()[
    zoneID];
const vectorField&               U                = eqn.psi();
const volVectorField&    camber  = mesh_.lookupObject<
    volVectorField>("camber");
const vectorField&               CC               = mesh_.C(); //
    cell center


const scalar B = 7;
const scalar OMEGA = -281.01;


//Initializing all fields
scalar x,y,z,RADIUS,THETA,OMEGAR,NX, NY,NZ, NTH, NR, WX,WY,WZ,
    WMAG, WDOTN,
WNX,WNY,WNZ,DEVLOC,WTX,WTY,WTZ,WTMAG,TX,TY,TZ,
FNX,FNY,FNZ,FTX,FTY,FTZ,MOMSRCX,MOMSRCY,MOMSRCZ;


forAll(cells, i)
{


x = CC[cells[i]].x();
y = CC[cells[i]].y();
z = CC[cells[i]].z();
```

```
RADIUS = sqrt(y*y + z*z);

THETA = atan2(y,z);


OMEGAR = OMEGA*RADIUS;


NX     = camber[cells[i]].x();

NR  = camber[cells[i]].y();

NTH    = camber[cells[i]].z();


NY = NR*sin(THETA) + NTH*cos(THETA);

NZ = NR*cos(THETA) - NTH*sin(THETA);


WX= U[cells[i]].x();

WY= U[cells[i]].y() - OMEGAR*cos(THETA);

WZ= U[cells[i]].z() + OMEGAR*sin(THETA);

WMAG = sqrt(WX*WX + WY*WY + WZ*WZ);


WDOTN = WX*NX + WY*NY + WZ*NZ;


WNX = WDOTN*NX;

WNY = WDOTN*NY;

WNZ = WDOTN*NZ;

DEVLOC = asin(WDOTN/max(WMAG,1e-9));


WTX = WX - WNX;

WTY = WY - WNY;

WTZ = WZ - WNZ;

WTMAG = max(sqrt(WTX*WTX + WTY*WTY + WTZ*WTZ),1e-9);


TX = WTX/WTMAG;

TY = WTY/WTMAG;

TZ = WTZ/WTMAG;
```

```
FNX = -DEVLOC*cos(DEVLOC)*WMAG*WMAG*B*NX/RADIUS/max(abs(NTH),1e
    -9);
FNY = -DEVLOC*cos(DEVLOC)*WMAG*WMAG*B*NY/RADIUS/max(abs(NTH),1e
    -9);
FNZ = -DEVLOC*cos(DEVLOC)*WMAG*WMAG*B*NZ/RADIUS/max(abs(NTH),1e
    -9);


FTX = DEVLOC*sin(DEVLOC)*WMAG*WMAG*B*TX/RADIUS/max(abs(NTH),1e
    -9);
FTY = DEVLOC*sin(DEVLOC)*WMAG*WMAG*B*TY/RADIUS/max(abs(NTH),1e
    -9);
FTZ = DEVLOC*sin(DEVLOC)*WMAG*WMAG*B*TZ/RADIUS/max(abs(NTH),1e
    -9);


MOMSRCX = 0.5*(FTX + FNX);
MOMSRCY = 0.5*(FTY + FNY);
MOMSRCZ = 0.5*(FTZ + FNZ);


//adding source terms to the momentum equation
F[cells[i]] = vector(MOMSRCX, MOMSRCY, MOMSRCZ);


Pout << " x r MOMSRCX MOMSRCY MOMSRCZ" << endl;
Pout << x << RADIUS << MOMSRCX << MOMSRCY << MOMSRCZ << endl;


}


eqn += F;


#};
codeSetValue
#{
```

```
//Pout<< "**codeSetValue**" << endl;
#};
// Dummy entry. Make dependent on above to trigger recompilation
code
#{
$codeInclude
$codeCorrect
$codeAddSup
$codeSetValue
#};
}
bodyForceRotorCoeffs
{
$vectorCodedSourceCoeffs;
}
}
```

3. nx_data

```
//(x RADIUS nx )
(
(    0.00541909    0.08799994    -0.83941459 )
(    0.00493391    0.08799994    -0.98160586 )
(    0.00579664    0.08799994    -0.95934339 )
(    0.00618960    0.08799994    -0.95058816 )
.              .              .
.              .              .
.              .              .
.              .              .
.              .              .
.              .              .
(    0.00618960    0.08799994    -0.95058816 )
)
```

Appendix B

Implementation of Hall's BFM in Star-CCM+

This section provides a list of STAR-CCM+ parameters, field functions and example tables used to implement Hall's original body force model.

B.1 List of Parameters

Parameters	Expression
Number of blades	7
Rotation speed	281.01
unit x	[1.0, 0.0, 0.0]
unit y	[0.0, 1.0, 0.0]
unit z	[0.0, 0.0, 1.0]

B.2 List of Field Functions

Field functions	Expression
B	${Number of blades}
Deviation	asin(${WDOTN}/max(${WMAG},1e-9))
F	0.5*${Density}*($$({FN}+$$({FT})
FN	${FNX}*$$({unit x}+${FNY}*$$({unit y}+${FNZ}*$$({unit z}
FNX	-${Deviation}*cos(${Deviation})*${WMAG}*${WMAG}*$B*${NX}/$RADIUS/max(abs(${NTH}),1e-9)
FNY	-${Deviation}*cos(${Deviation})*${WMAG}*${WMAG}*$B*${NY}/$RADIUS/max(abs(${NTH}),1e-9)
FNZ	-${Deviation}*cos(${Deviation})*${WMAG}*${WMAG}*$B*${NZ}/$RADIUS/max(abs(${NTH}),1e-9)
FT	(${FTX}*$$({unit x}+${FTY}*$$({unit y}+${FTZ}*$$({unit z})
FTX	${Deviation}*sin(${Deviation})*${WMAG}*${WMAG}*$B*$TX/$RADIUS/max(abs(${NTH}),1e-9)

Field functions	Expression
FTY	`${Deviation}*sin(${Deviation})*${WMAG}*${WMAG}*$B*$TY/$` `RADIUS/max(abs(${NTH}),1e-9)`
FTZ	`${Deviation}*sin(${Deviation})*${WMAG}*${WMAG}*$B*$TZ/$` `RADIUS/max(abs(${NTH}),1e-9)`
NR	`interpolatePositionTable(@Table("camber"),` `@CoordinateSystem("Laboratory.Cylindrical"), "nr")`
NTH	`interpolatePositionTable(@Table("camber"),` `@CoordinateSystem("Laboratory.Cylindrical"), "nth")`
NX	`interpolatePositionTable(@Table("camber"),` `@CoordinateSystem("Laboratory.Cylindrical"), "nz")`
NY	`${NR}*sin(${THETA})+${NTH}*cos(${THETA})`
NZ	`${NR}*cos(${THETA})-${NTH}*sin(${THETA})`
OMEGA	`${Rotation Speed}$`
OMEGAR	`${OMEGA}*${RADIUS}`
RADIUS	`sqrt($${Position}[1]*$${Position}[1]+$${Position}[2]*$` `${Position}[2])`
T	`${TX}*$${unit x}+${TY}*$${unit y}+${TZ}*$${unit z}`
THETA	`atan2($${Position}[1],$${Position}[2])`
TX	`${WTX}/${WTMAG}`
TY	`${WTY}/${WTMAG}`
TZ	`${WTZ}/${WTMAG}`
W	`($${Velocity}[0])*$${unit x}+` `($${Velocity}[1]-${OMEGAR}*cos(${THETA}))*$${unit y}+` `($${Velocity}[2]+${OMEGAR}*sin(${THETA}))*$${unit z}`
WDOTN	`${WX}*${NX}+${WY}*${NY}+${WZ}*${NZ}`
WMAG	`sqrt(${WX}*${WX}+${WY}*${WY}+${WZ}*${WZ})`
WNX	`${WDOTN}*${NX}`
WNY	`${WDOTN}*${NY}`
WNZ	`${WDOTN}*${NZ}`
WTMAG	`max(sqrt(${WTX}*${WTX}+${WTY}*${WTY}+${WTZ}*${WTZ}),1e-6)`
WTX	`${WX}-${WNX}`
WTY	`${WY}-${WNY}`
WTZ	`${WZ}-${WNZ}`
WX	`$${Velocity}[0]`
WY	`$${Velocity}[1]-${OMEGAR}*cos(${THETA})`
WZ	`$${Velocity}[2]+${OMEGAR}*sin(${THETA})`

B.3 Example Lookup Table for Camber Normal Distributions

The coordinate spacing was chosen such that it was finer than the grid spacing in each coordinate direction (r, θ, z).

"r (m)",	"theta (radian)",	"z (m)",	"nr",	"nth",	"nz"
0.088	4.71238898	0.005	-0.14748	0.27018	-0.9576
0.08846488	4.71238898	0.005	-0.12679	0.246428	-0.95834
0.08892977	4.71238898	0.005	-0.12605	0.245144	-0.95864
0.08939465	4.71238898	0.005	-0.1253	0.243857	-0.95894
0.08985953	4.71238898	0.005	-0.12456	0.242568	-0.95924
0.09032441	4.71238898	0.005	-0.1238	0.241277	-0.95954
0.0907893	4.71238898	0.005	-0.12305	0.239984	-0.95984
0.09125418	4.71238898	0.005	-0.12229	0.238689	-0.96014
0.09171906	4.71238898	0.005	-0.12153	0.237392	-0.96044
0.09218395	4.71238898	0.005	-0.12077	0.236092	-0.96074
.					
.					
.					
.					
.					
.					
0.09264883	4.71238898	0.005	-0.12	0.234791	-0.96104
0.09311371	4.71238898	0.005	-0.11923	0.233487	-0.96134

Appendix C

Additional Remarks on Chapter 3 Findings

Chapter 3 presented the results for the effect of blade count on the total enthalpy rise prediction accuracy of Hall's original body force model as compared to the bladed computations with all friction-less walls and blade surfaces. The results are re-displayed below in Figure C.1. This chapter attempts to shed more light on the mechanisms that govern the flow physics for different blade counts.
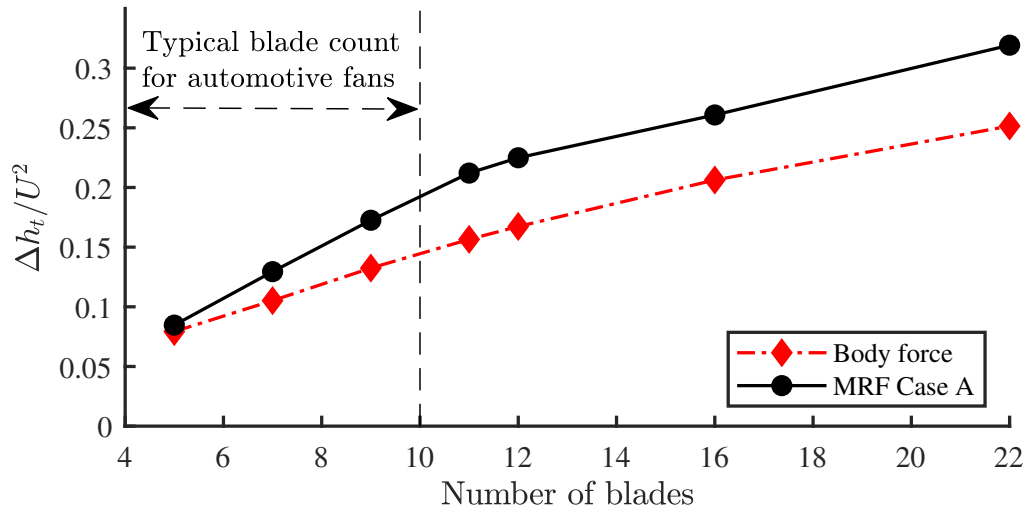

Figure C.1: Fan work coefficient as a function of the number of blades at the design operating point

The accuracy of the body force model predictions improves as we move to lower blade counts which is surprising because one would expect the circumferentially-averaged flow field version created by Hall's model to be a less accurate version of the actual flow field in the limit of low blade count where there are higher blade-to-blade non-uniformities, as depicted in Figure C.2.

Aircraft engine fan

Automotive radiator fan

Actual flow angle variation

Body force represented average
(~Zero deviation version)

More or less
uniform flow
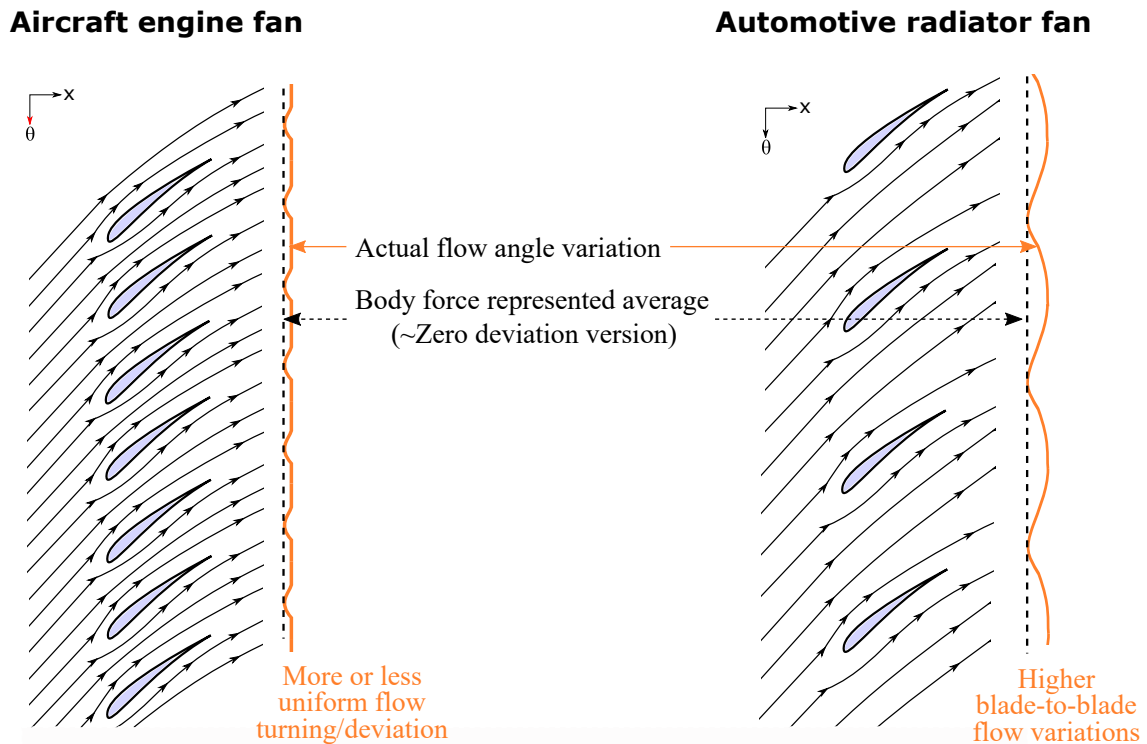turning/deviation

Higher
blade-to-blade
flow variations

Figure C.2: Hall's body force model tries to drive the deviation of the flow from the blade camber surface to zero. This behavior works well for high solidity aircraft engine fans which create more or less uniform flow turning through the entire blade passage. However, for an automotive radiator fan with a low solidity, there is higher blade-to-blade spacing and the net deviation of the flow from the blade camber surface is not actually zero. However, Hall's model ignores these blade-to-blade flow variations and tries to create a zero-deviation circumferentially-uniform version of the flow field even for the automotive fan. Hence, it was expected that Hall's model assumptions would break in the limit of low blade count.

Another very interesting thing to note in Figure C.1 is the change in slope of the MRF curve at a blade count of 11, and an even more interesting feature is that the body force model curve also exhibits this change in slope, though it's much less dramatic compared to the bladed results. For all blade counts above 11, there is almost a constant offset between the two curves. On the other hand, in our typical range of blade count for automotive fans ($B < 10$), the body force model shows a significantly different slope than the bladed MRF results.

This suggests that we have two different flow regimes:

1. a high blade count regime ($B > 10$), where model accuracy is not a strong function of the blade count, hence there is a constant offset between the two curves;

2. a low blade count regime ($B < 10$), where model accuracy is a strong function of the blade count (or solidity, for a given chord) of the fan, hence we see significant difference in the slopes of the two curves.

This may also suggest that in the *low blade count regime*, the normal force formulated by Hall may not be a linear function of the blade solidity any more.

To get a more detailed view of the flow fields, the axial velocity distributions just downstream of the fan are displayed in Figure C.3 for a low blade count of 7 and a high blade count of 12 to highlight the differences between the two.
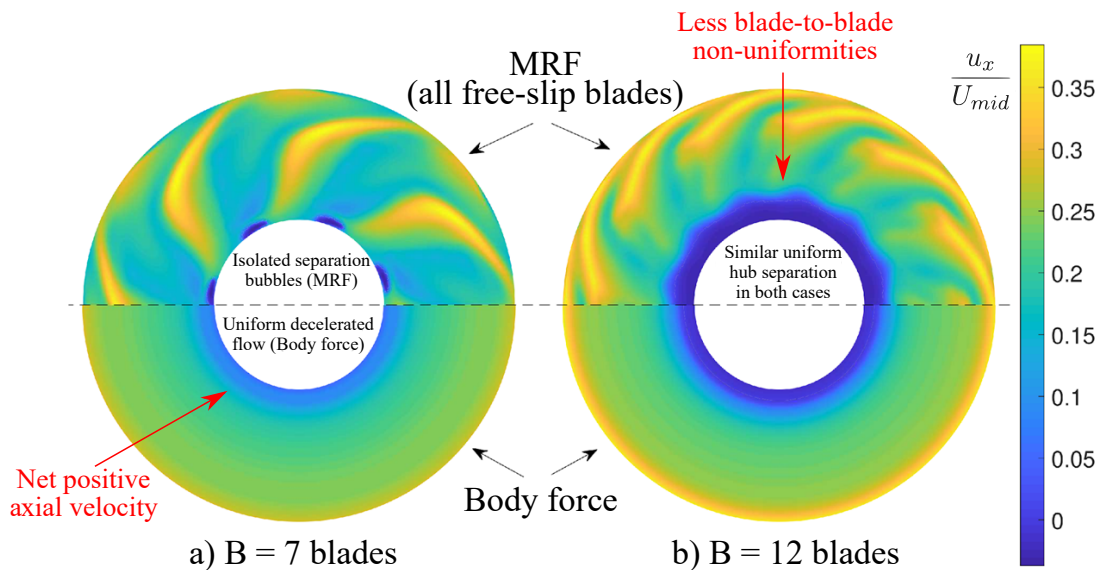

Figure C.3: Contours of axial velocity just downstream of the fan for a) low blade count of 7, and b) high blade count of 12, for the design operating point

At a higher blade count, due to the strong adverse pressure gradient near the hub, there is a massive hub separation that occurs just downstream of the fan despite the absence of boundary layers. This kind of separation, which occurs across the entire hub as depicted in C.3b, is seen for all blade counts above 10 and this is the potential reason for the sudden lowering of slope of the MRF curve seen in the high blade count regime in Figure C.1. The body force results for a blade count of 12 also show a similar separation.

For the low blade counts (Figure C.3a), there are certain isolated separation bubbles in the bladed simulations just downstream of the trailing edge of the fan and there are visible blade to blade non-uniformities. These bubbles increase in size as the blade count increases (until they coalesce for $B > 10$). However, the body force model does not capture these localized regions of flow separation and the corresponding circumferential average of the flow field generated by the body force has a net positive axial velocity everywhere. An artefact of this is that more work input is predicted by the body force model even in regions where there is actually a flow separation in reality. This is believed to be the cause for the difference in slopes between the two models for the low blade count regime.

Appendix D

Additional Full Vehicle Model Results for Chapter 4
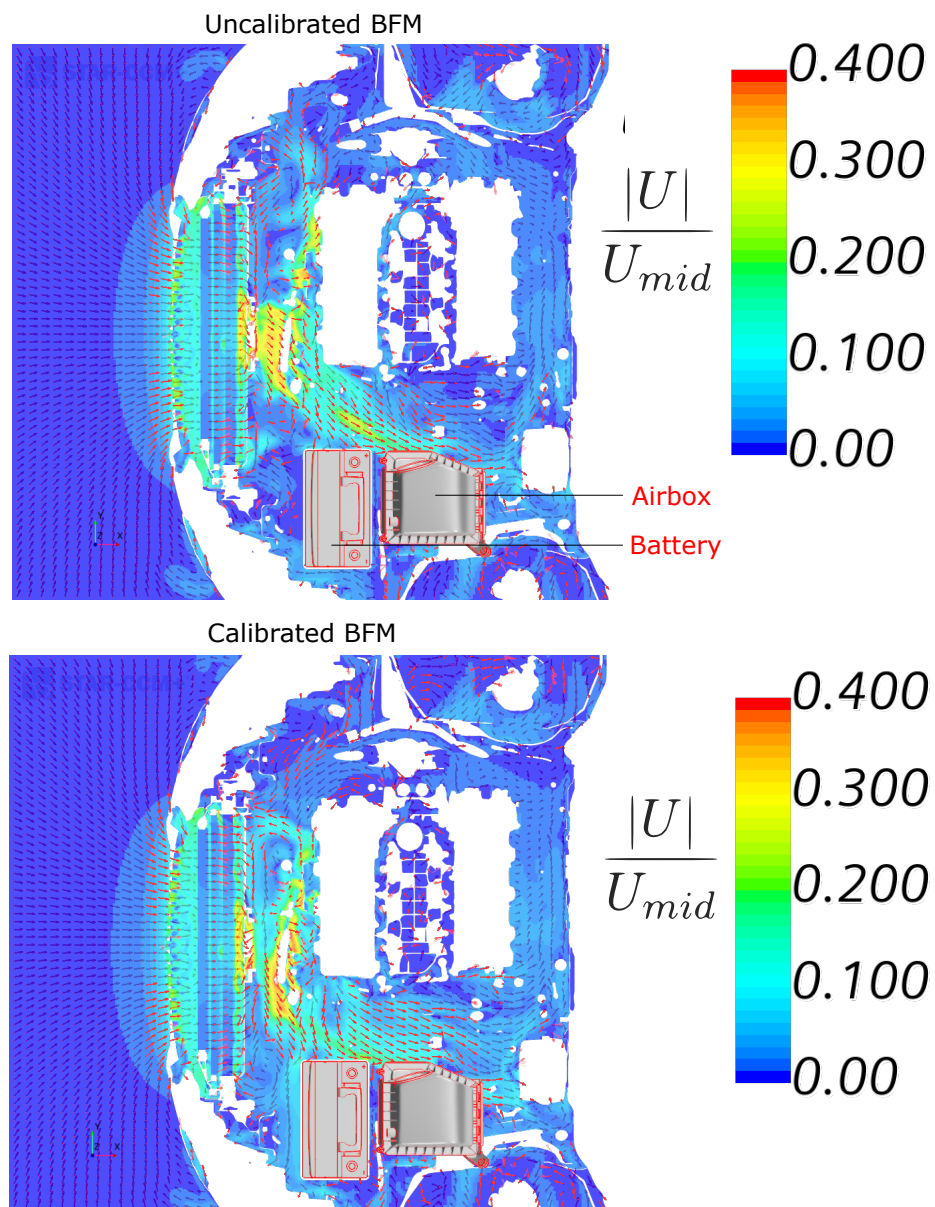
Uncalibrated BFM

Calibrated BFM

Figure D.1: Velocity magnitude contours on a horizontal slice through the full vehicle model, viewed from the top, for idle condition (zero tunnel flow rate)
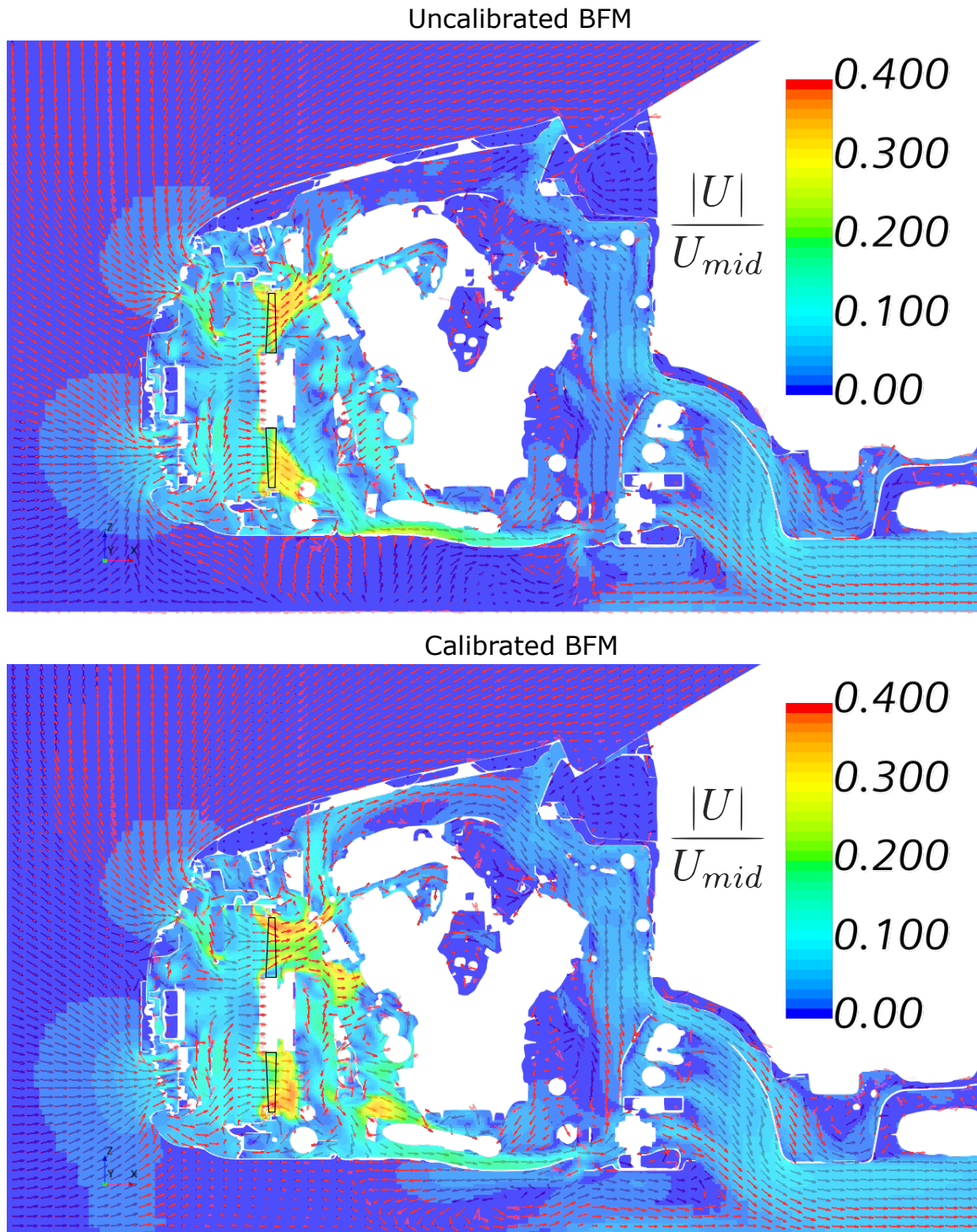
Uncalibrated BFM

Calibrated BFM

Figure D.2: Velocity magnitude contours on a vertical slice through the full vehicle model, viewed from the driver side, for idle condition (zero tunnel flow rate). Fan outline shown in black.

Appendix E

Determination of Design Flow Coefficient of a Fan

There are two ways to estimate the design flow coefficient of a fan:

1. **Incidence Matching:** Fans are usually designed such that at the optimum operating point, the incidence angle of the flow with respect to the leading edge of the blade camber surface is zero (see Figure E.1). This ensures that the flow is aligned as close to the blade surface as possible, hence there is minimum separation from the blade surface as the flow passes through the blade row.
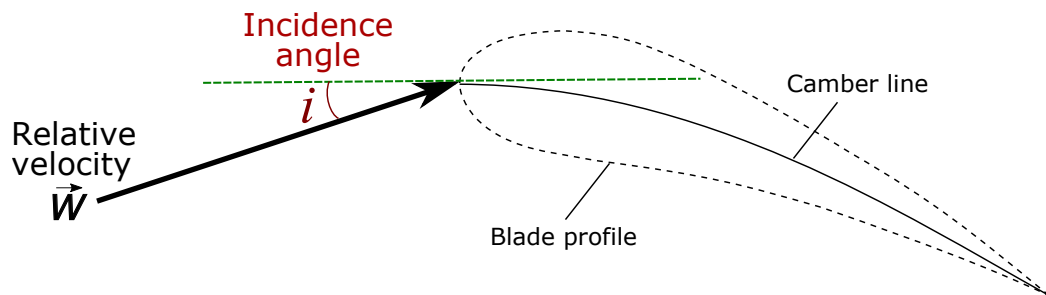

Figure E.1: Illustration of the leading edge incidence angle

The design flow coefficient corresponds to the average value of the axial velocity which yields a zero incidence angle throughout the span of the blade at a given rotational speed. For any non-zero values of flow incidence (any operation points away from the design flow coefficient), the fan efficiency is penalized. For incompressible flows, the change in rotational speed does not change the design flow coefficient (unless a major flow regime change occurs such as fully laminar flow or stall separation).

2. **Maximum Efficiency Point:** At the optimum operating point, the fan is designed to have minimum losses and hence maximum efficiency. The polytropic efficiency of a fan is defined as:

$$\eta_{poly} = \frac{\Delta \bar{p}_{\mathrm{t}}^{\mathrm{M}}/\rho}{\Delta \bar{h}_{\mathrm{t}}^{\mathrm{M}}} \tag{E.1}$$

where $\Delta \bar{p}_{\mathrm{t}}^{\mathrm{M}}$ and $\Delta \bar{h}_{\mathrm{t}}^{\mathrm{M}}$ are the mass-averaged values of the total pressure change and the total enthalpy change (fan work input), respectively, through the fan. Figure E.2 shows the polytropic efficiency values obtained for a range of flow coefficients for the 7-bladed MRF case with no-slip blades and endwalls. The design flow coefficient corresponds to the peak efficiency point of the fan curve.
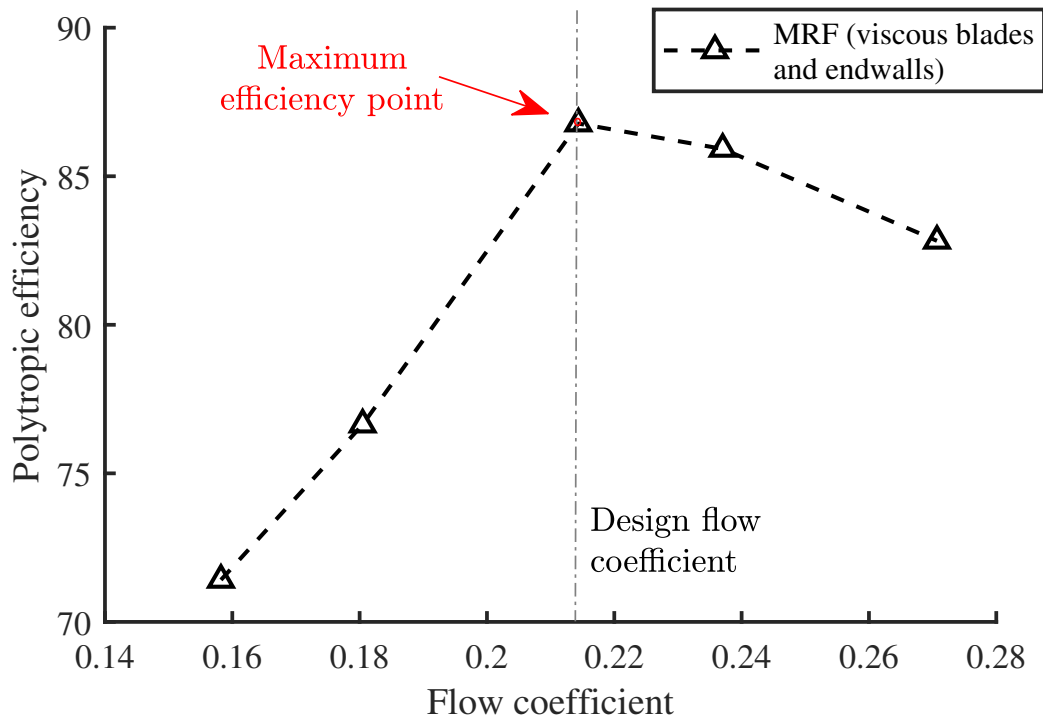

Figure E.2: Polytropic efficiency versus flow coefficient for the 7-bladed automtive fan (OPENFOAM v6 MRF results)

Appendix F

MATLAB code to Create Star-CCM+ Lookup Tables

```matlab
clear
clc

%%%% IMPORT COARSE SCATTERED DATA SET OF BLADE CAMBER NORMALS

rawdata = importdata('input/log.csv',',',1);

%This particular data set relates to a fan centered at the origin.

%Camber normals are function of axial (x_s) and radial positions (
    r_s) only
x_s = rawdata.data(:,1);
r_s = rawdata.data(:,2);


%Import the three components of the camber normals (x,r,theta)
nx_s = rawdata.data(:,5);
nr_s = rawdata.data(:,6);
nth_s = rawdata.data(:,7);

%%%% IMPORT CELL CENTER VOLUMES FOR ANY GRID %%%%
grid = importdata('input/fan_bodyforce_region.csv',',',1);
```

```matlab
%%%% IMPORT CELL COORDINATE INFORMATION FOR THE CELLS %%%%
x_o     = grid.data(:,2);
y_o     = grid.data(:,3);
z_o     = grid.data(:,4);


%%%% SPECIFY OFFSET FROM ORIGIN IF THE FAN GRID IS NOT CENTERED
    AT THE ORIGIN %%%%
xoffset = 0.341246;
yoffset  = 0;
zoffset  = 0.6372383;


%%%% CREATE INTERPOLATION POINTS (IN A FRAME OF REFERENCE WITH
    ORIGIN CENTERED AT THE FAN) %%%%
x_i     = grid.data(:,2) - xoffset;
y_i     = grid.data(:,3) - yoffset;
z_i     = grid.data(:,4) - zoffset;
r_i     = sqrt(y_i.^2 + z_i.^2);



%% PERFORM INTERPOLATION

%Create interpolation functions
F1 = scatteredInterpolant(x_s,r_s,nx_s,'natural');
F2 = scatteredInterpolant(x_s,r_s,nr_s,'natural');
F3 = scatteredInterpolant(x_s,r_s,nth_s,'natural');


%Find interpolated values for the camber surface normals
nx_i  = F1(x_i,r_i);
nr_i  = F2(x_i,r_i);
nth_i = F3(x_i,r_i);


%The net magnitude of the camber normals should be 1
```

```matlab
check = sqrt(nx_i.^2 + nr_i.^2 + nth_i.^2);



%% TABULATE VALUES


    data(:,1) = x_i;

    data(:,2) = y_i;

    data(:,3) = z_i;

    data(:,4) = nr_i;

    data(:,5) = nth_i;

    data(:,6) = nx_i;
%% Save data to a .csv file


file = sprintf('output/xyzgrid_camber.csv'); fileID = fopen(file,'
    w');

fprintf(fileID,'"X (m)","Y (m)","Z (m)", "nr", "nth", "nz" \n');


for k = 1:length(r_i)
fprintf(fileID,'%12.8f  %12.8f  %12.8f %12.8f %12.8f %12.8f \n',
    x_o(k),y_o(k),z_o(k),nr_i(k),nth_i(k),nx_i(k));
end
```

Vita Auctoris

Name: Palak Saini

Place of Birth: Phagwara, Punjab, India

Year of Birth: 1996

Education: M.A.Sc. in Mechanical Engineering
University of Windsor (Canada), 2020

Bachelor of Engineering in Aerospace
Punjab Engineering College (India), 2018